Tobias Lichtenegger, BSc

Drivers of extreme precipitation in Europe and Austria from regional to planetary scales

MASTER'S THESIS

to achieve the university degree of

Master of Science

Master's degree programme: Physics

submitted to

Graz University of Technology

Supervisor

Assoz. Prof. Dr.
Douglas Maraun
Wegener Center for Climate and Global Change

Graz, December 2020

AFFIDAVIT

I declare that I have authored this thesis independently, that I have not used other than the declared sources/resources, and that I have explicitly indicated all material which has been quoted either literally or by content from the sources used. The text document uploaded to TUGRAZonline is identical to the present master's thesis.

Date, Signature

Abstract

Extreme precipitation events are the result of the interplay of the atmospheric conditions at different scales. While the large-scale circulation can provide a favorable environment, events are eventually triggered by local factors like atmospheric stability and moisture content. Therefore, the influence of possible drivers on different scales on extreme precipitation over Europe and Austria is studied. The obtained GEV distributions for the SNAO, SEA, tropical precipitation and the Indian Summer Monsoon as predictors show comparable patterns to findings on mean precipitation. In Austria, extremes in regions south of the Alps are accompanied by moisture inflow from the Mediterranean, which is supported by the jet stream pattern, whereas north of the Alps, extremes are associated with north to northwesterly flow. In terms of weather types, the highest risk for extreme precipitation are found for types associated with low pressure systems over or south of Austria. The seasonal cycles of precipitation conditional on the weather types show maxima mostly in summer and are more pronounced for high percentiles. The atmosphere in the vicinity of extreme precipitation events is found to be warmer and more unstable than in the climatological mean. A positive relationship between CAPE and precipitation intensities is obtained for most regions and seasons, although high CAPE is not a sufficient for extreme precipitation to occur. CIN exhibits both positive and negative relationships with precipitation intensities, with large variations between regions and seasons.

Kurzfassung

Extreme Niederschlagsereignisse sind das Ergebnis des Zusammenspiels der atmosphärischen Bedingungen auf verschieden Skalen. Während die großskalige Zirkulation eine günstige Umgebung bereitstellen kann, werden Ereignisse letztendlich von lokalen Faktoren wie der Stabilität und dem Feuchtegehalt der Atmosphäre ausgelöst. Daher wird der Einfluss möglicher Treiber auf verschiedenen Skalen auf Extremniederschläge in Europa und Österreich untersucht. Die erhaltenen GEV Verteilungen für die SNAO and SEA, für tropischen Niederschlag und den indischen Sommermonsoon als Prädiktoren zeigen vergleichbare Muster mit Erkenntnissen zu gemittelten Niederschlägen. In Österreich werden Extreme in Regionen südlich der Alpen begleitet von Feuchtigkeitszustrom vom Mittelmeer, sichtbar auch im Jet Stream Muster, während nördlich der Alpen Extreme mit nördlicher bis nordwestlicher Strömung assoziiert werden. Bezüglich Wetterlagen geht die größte Gefahr für Extremniederschlag von Lagen aus, die mit Tiefdrucksystemen über oder südlich der Alpen assoziiert sind. Die Jahresgänge des Niederschlags abhängig von der Wetterlage habe ihre Maxima meistens im Sommer und sind ausgeprägter für höhere Perzentile. Die Atmosphäre in der Umgebung von extremen Niederschlagsereignissen ist wärmer und instabiler als im klimatologischen Mittel. Ein positiver Zusammenhang zwischen CAPE und Niederschlagsintensitäten zeigt sich für die meisten Regionen und Jahreszeiten, obwohl hohes CAPE nicht ausreicht dass Extremniederschlag auftritt. CIN weist sowohl positive wie negative Zusammenhänge mit Niederschlagsintensitäten auf, mit großen Unterschieden zwischen den Regionen und Jahreszeiten.

Danksagung

Ich möchte mich bei meinem Betreuer Assoz. Prof. Dr. Douglas Maraun für die Unterstützung im Verfassen dieser Arbeit bedanken, als auch beim gesamten Team der Arbeitsgruppe "Regionales Klima" am Wegener Center für die anregenden Diskussionen. Großer Dank gilt weiters meinen Eltern, die mir stets Vertrauen geschenkt und mich während des Studiums finanziell unterstützt haben. Des Weiteren gilt mein Dank meinen Freunden auf der Universität, die mir bei vielen Fragen weiterhalfen, als auch meiner Freundin und allen Freundinnen und Freunden außerhalb der Universität, die jederzeit für mich da waren und mich motivierten.

Contents

List of Figures

Chapter 1

Introduction

Extreme precipitation is one of the major disasters related to climate. It threatens human lives by causing flooding, land slides, debris flow and hail storms. Climate change is expected to intensify extreme precipitation in general, by the increased moisture holding capacity of the air at higher temperatures according to the thermodynamic Clausius-Clapeyron relationship (Allen and Ingram, 2002). On regional scales however, this can differ from the global-scale increase, with some regions showing no changes or even a decrease (Fischer et al., 2014). This has been attributed to changes in the dynamic contributions (Pfahl et al., 2017).

Two examples in recent history for devastating impacts caused by extreme precipitation are the August 2002 flood in several central European countries, especially along the Elbe and Danube river basins (Grazzini and van der Grijn, 2002; Ulbrich et al., 2003b,a), and the June 2013 flood in Bavaria and Austria (Grams et al., 2014).

The August 2002 flood directly affected over 2 million people, claiming 100 fatalities in total and causing an economic loss estimated at around 30 billion Euro, which makes it the most expensive weather-related catastrophe in Europe in recent decades. An anomalous large-scale circulation in July and August 2002 was found to be the driving force of the event. In July, strong zonal flow over the Atlantic led to several transient waves passing western and central Europe, causing a first wave of anomalous precipitation in the later affected areas. In August, a more blocked circulation with high pressure over northern Europe caused enhanced cyclogenesis over the Mediterranean. The main rainfall event between the 10th and 13th of August was associated with a cyclone moving slowly from the Gulf of Genoa northeastward on a Vb cyclone path, which is known to be responsible for heavy precipitation over central Europe (Messmer et al., 2015; Hofstätter et al., 2018).This advected warm and moist air into central Europe and caused enhanced orographic lifting at the northern slopes of the central European mountain ranges. Several stations experienced record-breaking 24-hour accumulated precipitation values during this time. The gauge level of the Elbe river in Dresden measured in the aftermath of the precipitation was the highest since 1275.

The flood event in early June 2013, affecting the entire northern side and foothills of the Alps as well as the Czech Republic, caused 25 fatalities and an economic damage of more than 12 billion Euro (Grams et al., 2014). The event was preceded by a blocked circulation over Europe over the second half of May, with anticyclonic conditions over the central northern Atlantic and over Scandinavia. Over central Europe, a quasi-stationary upper-level cut-off low established, caused by repeated upper-tropospheric Rossby wave breaking. This already led to anomalous high rainfall rates in the later affected regions prior to the flooding. The main precipitation events during the first days in June were associated with three cyclones, all of which were formed over the Balkans and moved on an unusual track northwestward, establishing a northern flow towards the Alps.

These examples demonstrate, that such extreme precipitation events are influenced by processes on different scales. While ultimately the precipitation is triggered by local factors like instability, increased uplift and enhanced moisture availability, the larger-scale synoptic circulation is crucial in providing a favorable environment for these factors (Barlow et al., 2019). A favorable synoptic situation for extreme precipitation in a specific region, in turn, is more or less likely to appear depending on the conditions on the continental to hemispheric scale.

Thus, in this thesis, drivers at different scales which might be relevant for extreme precipitation over Europe (in case of large-scale drivers) and Austria (when going to synoptic- to regional-scale drivers) will be investigated. On the large-scale, the Summer North Atlantic Oscillation (SNAO) and the Summer East Atlantic (SEA) as well as teleconnections from tropical precipitation and the Indian Summer Monsoon will be considered. Furthermore, typical patterns of the jet stream and moisture transport during extreme events will be revealed. At the synoptic scale, the influence of different weather types on extreme precipitation in Austria are studied. Finally, the atmospheric stability in the vicinity of the events will be investigated.

Of course, the drivers considered here are only a selection. Other important drivers from sea ice extend and sea surface temperatures to cut-off lows,fronts and soil moisture are not explicitly considered in this thesis.

In Chapter 2, general aspects and fundamentals of the later analysed drivers are given. Chapter 3 lists the used data, defines regions in Austria in which extreme precipitation events are investigated and introduces the method used for the extreme value analysis. Chapter 4 shows and discusses the results. Chapter 5 gives a summary and conclusion.

Chapter 2

General aspects

2.1 Large-scale drivers

In this section, several modes of climate variability and climate phenomena and their already investigated impacts on European summer surface temperatures and (mean) precipitation are presented. The corresponding indices are then used to investigate a possible influence on extreme precipitation in summer in Europe with the methods described in Sec. 3.3 and 3.4.

2.1.1 Summer North Atlantic Oscillation

The North Atlantic Oscillation (NAO) is the most prominent regional pattern of sea level pressure variability in the North Atlantic (Hurrell et al., 2003a). The Summer North Atlantic Oscillation (SNAO) can be defined similar to the NAO, as the leading empirical orthogonal function of mean sea level pressure (SLP) in the North Atlantic in the summer season. The North Atlantic region and summer season are defined as the domain [20°N-70°N; 90°W-40°E] and the months June-August (Hurrell et al., 2003b). In some studies, the domain is restricted to the region north of 40°N (Bladé et al., 2012) or the shortened season July-August is used (Folland et al., 2009), motivated by discontinuity problems in Northern Africa and the differing behaviour of the June NAO compared to July and August. However, neither of these differences did alter the results in these studies.

Figure 2.1 shows the spatial patterns of the leading EOFs of mean SLP in the North Atlantic for each season separately as defined in (Hurrell et al., 2003b). The SNAO is characterized in its positive phase by increased pressure in northwestern Europe and stretching out to the North Atlantic, and negative anomalies over Greenland. Compared to the winter NAO, the centers of action are shifted poleward and the pattern has a smaller spatial extent. The variance explained is highest in winter with 36.7% compared to 22.1% in summer. With other definitions the explained

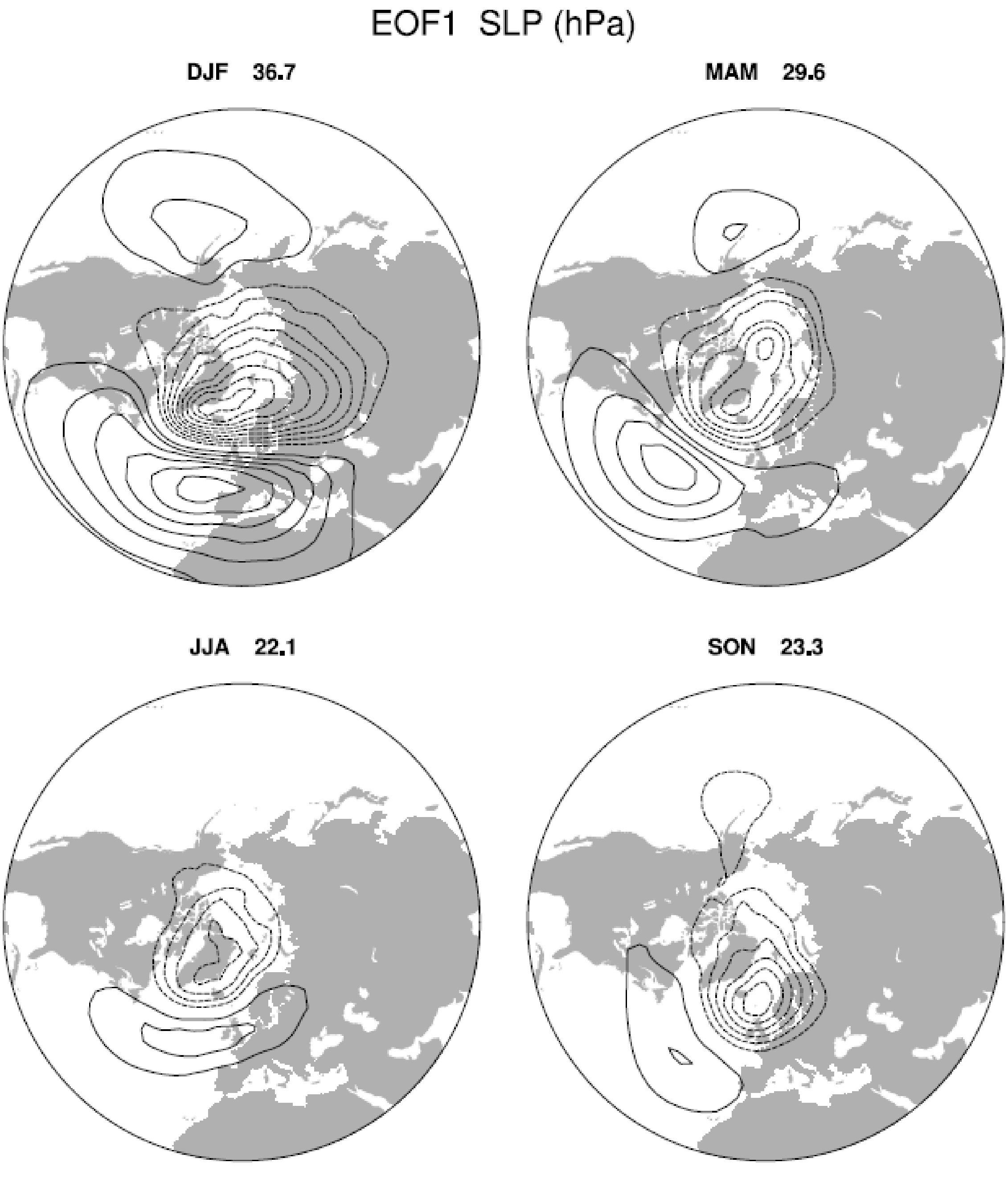

Figure 2.1: Leading EOFs of mean SLP anomalies for the period 1899-2001 in the North Atlantic (20°N-70°N, 90°W-40°E) for each season. The value gives the percentage of total variance explained by the EOF. The contours show the amplitude in hPa, obtained by regressing the hemispheric sea level pressure anomalies upon the leading principal component time series. The contour increment is 0.5 hPa, the zero contour has been excluded. The figure is taken from Hurrell et al. (2003b).

variance in summer can also be higher (Bladé et al., 2012; Folland et al., 2009), but remains always lower than in the winter months.

This pattern results in some obvious surface impacts of the SNAO over Europe. In its positive phase, positive temperature anomalies as well as reduced cloudiness and precipitation are observed over the United Kingdom and Scandinavia associated with the increased pressure in this region (Folland et al., 2009; Chronis et al., 2011). Less obvious are the strong anti-correlations of the SNAO with temperature and precipitation over southern Europe, especially in the eastern Mediterranean and over the Balkans (Bladé et al., 2012; Mariotti and Arkin, 2006; Mariotti and Dell'Aquila, 2012), For precipitation, the resulting pattern is a northwest - southeast dipole over Europe, with highest anti-correlations (up to 0.8) stretching from Ireland to southern Scandinavia and positive correlations of up to 0.6 in Italy, Greece and the Balkans. This is broadly opposite to the precipitation pattern arising from the winter NAO (Vicente-Serrano and López-Moreno, 2008). This pattern also strongly resembles the pattern of the first EOF of European summer precipitation, which has a tripole pattern with enhanced precipitation spanning a region from the British Isles to the Baltic Sea and western Russia and suppressed precipitation in northern Scandinavia and over the Mediterranean (Zveryaev and Allan, 2010). The SNAO can explain up to 45% of this variance in the North and Baltic Sea and 30% in the eastern Mediterranean (Mariotti and Arkin, 2006).

While the change in sign in northern Europe can be explained by the anticyclonic conditions there, an influence of the SNAO on precipitation in the Mediterranean area is not obvious, since the centers of action of the SNAO are too far away to explain modulations of the inflow of maritime air into this region as in winter. Bladé et al. (2012) have found that the positive SNAO phase is accompanied by an upper level trough over the Balkans and a second weaker trough west of Iberia, resulting in an increased potential instability. Together with the warm summer Sea Surface Temperatures (SSTs) and the orographic uplift along the mountains, this suggests a possible explanation of the positive correlations between the SNAO and precipitation in these regions by providing a favourable environment for enhanced summer convection. The upper level troughs were furthermore linked to a hemispheric pattern of anomalies, which could be triggered by a quasi-stationary Rossby wave excited by the SNAO.

The abovementioned studies on the influence of the SNAO on precipitation considered only the mean of the distribution. Tabari and Willems (2018) studied the influence of several large-scale patterns, including the NAO, on decadal anomalies of European summer precipitation extremes in different seasons. They found a profound influence of the NAO on winter extremes, roughly resembling the pattern found for mean precipitation. For summer extremes no significant influence were found. This can be due to the definition of the NAO used in their study. They define the NAO index as the normalized sea level pressure (SLP) difference between the Azores high pressure and the Icelandic low pressure. However, they noted an influence of the concurrent Western Mediterranean Oscillation (WeMO) and the preceding winter NAO and Southern Oscillation Index (SOI) on summer extreme precipitation over Europe.

Rahimpour et al. (2016) have estimated the parameters of the generalized extreme value (GEV) distribution for monthly and annual maxima of daily precipitation at different stations in the Netherlands, by taking the NAO into account. They concluded that the positive NAO phase intensify extreme precipitation, but they did not distinguish between individual months or seasons.

2.1.2 Summer East Atlantic pattern and tropical precipitation

The Summer East Atlantic (SEA) pattern is the second leading EOF of geopotential height anomalies in the North Atlantic after the SNAO, explaining 18% of the JJA mean z_{500} variance in the 1979-2016 period (Wulff et al., 2017). Fig. 2.2 shows the mean z_{500} anomalies in the North Atlantic and over Europe as found by Wulff et al. (2017). The positive phase of the SEA pattern is characterized by significant negative height anomalies over the entire North Atlantic, centered southwest of Iceland and covering Iceland, Greenland and stretching into the North American continent. Positive anomalies of smaller magnitude are seen over central and northern Europe, centered over the Baltic Sea. A second positive area does appear over the Atlantic off the coast of the United States. Wulff et al. (2017) showed that height anomalies are also present outside this region over the entire northern hemisphere in an zonally alternating way and that it coincides with the jet stream position, indicating that the SEA pattern is part of a circumglobal wave train.

The impacts on surface temperature over the Atlantic and Europe were found to be strongest in the same regions were the height anomalies have their maxima, with positive surface temperature anomalies coinciding with positive height anomalies. The regression of precipitation on the SEA index, defined as the corresponding Principal Component time series of the EOF, reveals negative influence around the Baltic Sea and only a small region of significantly enhanced precipitation west of Ireland.

Interestingly, surface temperatures and precipitation in the tropical Pacific and Atlantic do also covary with the SEA index. The positive SEA phase is accompanied by anomalous warm and wet conditions over the tropical Pacific and with rather dry and cold conditions over central America and the tropical Atlantic. For precipitation

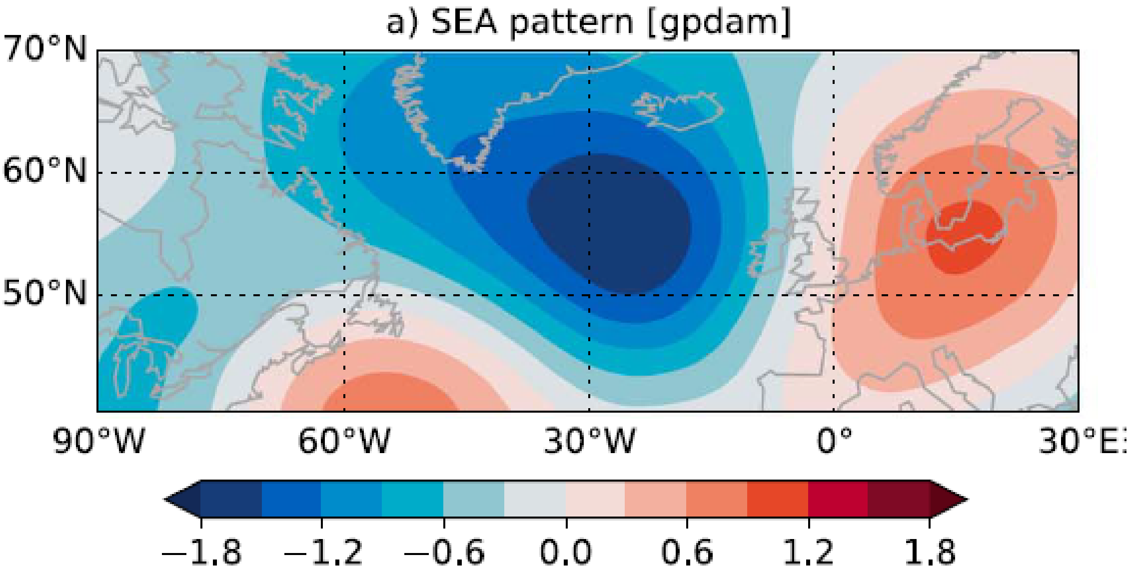

Figure 2.2: Second EOF of JJA mean geopotential height anomalies for the period 1979-2016 in the North Atlantic (40°N-70°N, 90°W-30°E). The figure is taken from Wulff et al. (2017).

also significantly reduced precipitation over Indonesia were found.

Wulff et al. (2017) argued that, instead of the SEA causing these anomalies in the tropics, the tropical Pacific-Atlantic dipole is actually forcing the SEA pattern by showing that the JJA mean z_{500} regressed on an index based on the difference of tropical Pacific and Atlantic precipitation reveals a pattern strongly resembling the SEA pattern. However, they did not investigate whether the surface temperatures and precipitation does also covary with tropical precipitation in the same way as with the SEA. A possible explanation for this forcing might be tropical-extratropical teleconnection induced by a Rossby Wave Source, which can be generated by the diabatic heating associated with the tropical precipitation anomalies (Sardeshmukh and Hoskins, 1988).

2.1.3 Indian Summer Monsoon

The Indian Summer Monsoon is part of the Asian monsoon system and does account for 60-90% of annual rainfall in India between June and September (Shukla and Huang, 2016). It exhibits large spatial and temporal variations influenced by a wide range of drivers, including the El Niño Southern Oscillation, the Indian Ocean Dipole, the Atlantic Multidecadal Oscillation and the Pacific Decadal Oscillation (Ashok et al., 2001; Nair et al., 2018).

The Indian Summer Monsoon in turn has been known to influence the Mediterranean via the so called "monsoon-desert teleconnection" (Rodwell and Hoskins, 1996).Theoretically, remote diabatic heating in the Indian Summer Monsoon region induces a Rossby wave propagating to the west. Over the eastern Sahara and

Mediterranean, the interaction of the Rossby wave with the southern flank of the mid-latitude westerlies causes the air to descent adiabatically, causing dry conditions in these regions during summer. It has been shown that this theoretical teleconnection is indeed present in atmospheric reanalysis data (Tyrlis, 2013).

Ossó et al. (2019) found significant correlations between precipitation anomalies over the Balkans and a precipitation index representative for the Indian Summer Monsoon. Overall, 40% of the interannual summer precipitation variability in this area can be explained by the Indian Summer Monsoon. No other regions of strong tropical precipitation were found to significantly correlate with precipitation in this area, strengthening the assumption of an influence of the Indian Summer Monsoon. They further showed with model experiments that the monsoon-desert teleconnection plays a key role in forcing this precipitation response.

2.2 Jet stream

The jet stream is a narrow wind current in the upper troposphere, with winds often exceeding 30 m/s and peaks up to 150 m/s, which are among the strongest winds found on earth. It is a consequence of the thermal wind balance between the vertical shear of the zonal wind and the meridional temperature gradient (Holton, 2004).

The thermal wind can be derived by taking the geostrophic wind relationship

$$u_g = -\frac{1}{f}\frac{\partial \Phi}{\partial y} \tag{2.1}$$

and substituting the geopotential Φ with the help of the hydrostatic equation and the ideal gas law:

$$\frac{\partial \Phi}{\partial p} = -\alpha = -\frac{RT}{p} \tag{2.2}$$

Integrating the result from pressure level p_0 to p_1 yields a relationship for the thermal wind:

$$u_T = -\frac{R}{f}\left(\frac{\partial \langle T \rangle}{\partial y}\right)_p ln\left(\frac{p_0}{p_1}\right) \tag{2.3}$$

where R denotes the specific gas constant, f the Coriolis parameter and $\langle T \rangle$ the mean temperature in the layer between p_0 and p_1. This shows that the thermal wind is proportional to the meridional temperature gradient $\frac{\partial \langle T \rangle}{\partial y}$ and increases with height. It is actually the difference between the geostrophic wind on two pressure levels, i.e. the vertical wind shear. There is also a component proportional to the longitudinal temperature gradient, which is in general much weaker.

The jet streams therefore arise at latitudes with a high meridional temperature gradient between the warm tropics and the cold poles near the tropopause at roughly 300 hPa. They blow parallel to the isotherms , with the warm air to the right facing downstream in the Northern Hemisphere. A counterclockwise turning geostrophic wind with height is associated with cold-air advection, while clockwise turning yields warm-air advection (Holton, 2004).

In each hemisphere, two jets are usually distinguished: The subtropical jet stream and the polar front or eddy-driven jet stream. The subtropical jet stream is formed at the poleward edge of the Hadley cell at ~30° latitude and is shallow, while the polar front jet stream is created by eddy momentum flux convergence usually between 40° and 60° latitude and reaches deeper into the troposphere (Panetta, 1993; Woollings et al., 2010). Due to the high variability in jet position, especially for the polar front jet stream, the two jets cannot always be separated (Lee and Kim, 2003).

The jet stream has a key role in the formation of mid-latitude cyclones, because it signifies the existance of enhanced baroclinicity and potential energy (Koch et al., 2006). Conceptually, in order to decrease the surface pressure and forming a cyclone, there must be a net divergence of mass in the region above the cyclone. If the jet stream exhibits disturbances from the normal zonal flow and move in a wave like form, the maximum wind speeds will be found in the ridges, while the wind speed is lower in the troughs. This can be explained when representing the wind field associated with the wave by the gradient wind, as this wind is less than the geostrophic wind (subgeostrophic) in cyclones and greather than the geostrophic wind (supergeostrophic) in anticyclones (Lynch and Cassano, 2006). Therefore, there will be an acceleration of the jet stream when the air moves from a trough to a ridge, resulting in upper level divergence and, in further consequence, in lower level convergence and cyclogenesis to the east of an upper level trough. Vice versa, there will be upper level convergence and lower level divergence to the left of an upper level trough (see Fig. 2.3).

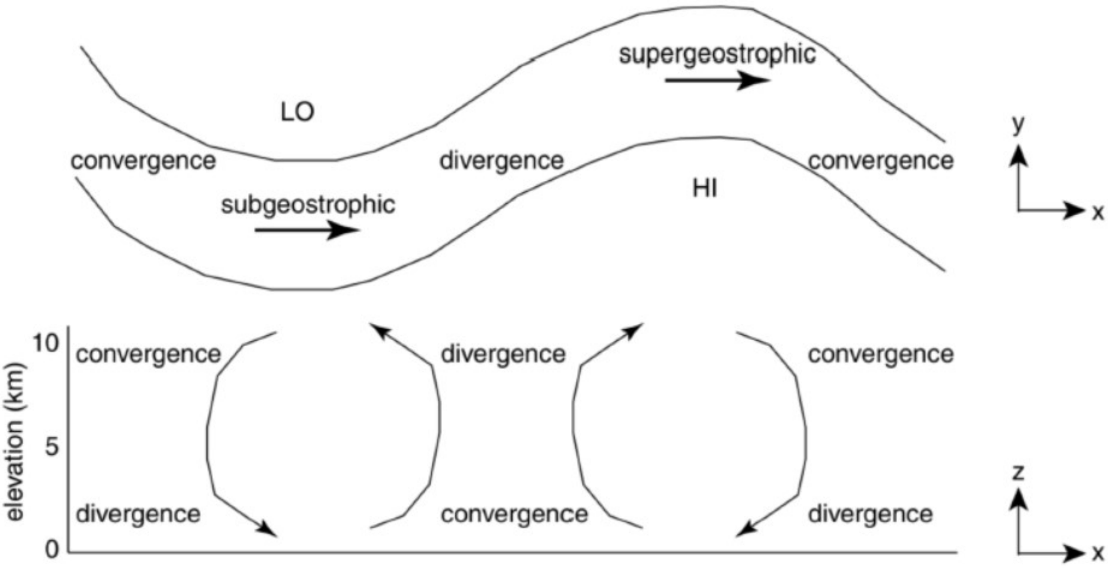

Figure 2.3: (a) The divergence field in the horizontal. The maximum wind speed of the air moving through a wave will be found in the ridge (supergeostrophic wind) and the minima in the trough (subgeostrophic wind). (b) the divergence field in the vertical. Upper level divergence (convergence) regions cause corresponding lower level convergence (divergence) regions. The figure is taken from Lynch and Cassano (2006).

Since the jet stream can be linked to surface weather, there are several studies concerning the features of the jet stream during extreme precipitation events. Toreti et al. (2010) investigated daily extreme precipitation along the Mediterranean coast and found that the position of the subtropical jet stream supports the precipitation region to be in a divergence area with enhanced ascent motions and instability. Barbero et al. (2019) found that the jet stream is a major driver of hourly precipitation extremes along the west coast of the United States. Lavers et al. (2015) looked into the connection of the large-scale atmospheric circulation with river flows and groundwater levels in England, concluding that the jet stream is usually significantly shifted southward in the months prior to the most extreme events. Jet stream maps can be further used to identify quasi-stationary Rossby waves, which are known to cause extreme surface weather conditions by blocking the normal circulation (Petoukhov et al., 2013; Screen and Simmonds, 2014; Coumou et al., 2014). Stadtherr et al. (2016) have shown that the Balkan floods 2014 were caused by an unusual slow moving cyclone due to a quasi-stationary wave train around the Northern Hemisphere at this time.

2.3 Weather types relevant for extreme precipitation in Austria

Going to the synoptic scale, weather types or synoptic patterns are often used to describe the atmospheric conditions in a region during a specific situation, e.g. an extreme precipitation event. The synoptic scale has an order of 1000 kilometers, which corresponds to the scale of typical high- and low-pressure systems as well as extratropical cyclones. The idea of classifying synoptic patterns into a finite number of weather types is to use these emerged weather types for an objective and statistical description of e.g. associated precipitation patterns. Within one weather type, the conditions in terms of advection and circulation should be quite similar (Beck and Philipp, 2010).

There is a long history on the investigation of the relevance of weather types on precipitation over different regions in Europe. Already in the 19th century, van Bebber (1891) classified cyclone tracks relevant for Europe, identifying the Vb-track, which is known to have a high potential for heavy precipitation and floods in central Europe (Messmer et al., 2015; Hofstätter et al., 2018). During the 20th century, several methods for classifying weather types have been developed (Hess and Brezowsky, 1999; Schüepp, 1968; Lauscher, 1972). These methods are often optimized for a certain region and do include subjective components and elements of the observed weather and can rely on relatively small-scale features. This makes it unsuitable for applications outside the regions for which there were designed for. Nonetheless, some of these are still standard methods used by national meteorological services: Hess and Brezowsky (1999) in Germany, Schüepp (1968) in Switzerland and Lauscher (1972) in Austria by the Zentralanstalt für Meteorologie und Geodynamik (ZAMG).

(Hess and Brezowsky, 1999) used mean sea level pressure fields for their classification. They obtain 29 weather types ("Großwetterlagen"), which were further grouped into three categories based on the large-scale circulation: zonal, meridional and mixed. Since they only considered the region between 45°and 65° latitude, this classification does not sufficiently include the Alpine region and the Mediterranean, both necessary for an adequate description of weather types relevant in Austria. Therefore, Lauscher (1972) adapted the method of Hess and Brezowsky (1999) by using a smaller region over the eastern Alps and considering the influence of cyclone activities over the Mediterranean. He ended up with a total of 17 classes (termed "Lauscher Classes" from now on), grouped into five categories.

More recently, Seibert et al. (2007) investigated synoptic patterns with relevance for extreme precipitation in Austria. Using a trajectory clustering method, they identified seven distinct synoptic patterns which can influence extreme precipitation and analysed the corresponding precipitation patterns. Moreover, they also identified seven regions in Autria with similar daily precipitation. The regions used for the analysis (see Sec. 3.2) will be based on these results.

Although the method by Seibert et al. (2007) would be appropriate for an analysis of the influence of different weather types on extreme precipitation in Austria, the implementation of such a method would be beyond the scope of this thesis. Instead, the Lauscher Classes will be used to differ between the weather types, as this method is still used by the ZAMG, which provides confidence in the quality of the classification. Moreover, with 17 classes this system should also provide a higher frequency per class than other comparable systems, which makes it more applicable for statistical analysis. Nonetheless, one should keep in mind that the Lauscher Classes were not designed to separate different synoptic situations leading to extreme precipitation in Austria. They also do neither include the temporal dimension of the synoptic development nor a characterisation of the intensity (Seibert et al., 2007).

Table 2.1 lists all Lauscher Classes which appeared in the series for the time period 1997-2018 provided by ZAMG. There are 18 classes compared to the 17 originally defined by Lauscher, with TSW being the new class. All high pressure classes won't be considered further, as they are not expected to be relevant for extreme precipitation and are not used in the analysis. The remaining classes can be divided into several groups. Classes where Austria is under direct low pressure influence are **TK**, where there is a low pressure system over middle Europe, **TR**, with several low pressure cores ordered meridionally over Europe and **Vb**, which is a special case of low pressure system which moves from the Adriatic Sea towards Poland. Classes where Austria lies a the edge of a low pressure system contains low pressure over the British Isles (**TB**), to the southwest of Austria (**TSW**), over the western Mediterranean (**TwM**, Genoa low) and over the Adriatic Sea (**TS**). The classes **N**, **NW**, **W**, **SW** and **S** indicate a strong and linear large-scale upper air flow from the corresponding direction. All days which cannot be classified in either of these groups fall into the remaining class **G**.

In Sec. 4.3, the parameters of the generalized pareto distribution (GPD, see Sec. 3.3) will be estimated based on the precipitation on days where a specific Lauscher Class occurred. Since there is not enough data to do this for each season separately (see Tab. 4.1), additionally the seasonal cycle of precipitation will be fitted for each Lauscher Class.

Table 2.1: The Lauscher Classes

Group	**Class**	**German long name**
High pressure	H	Hochdrucklage
	Hz	zonale Hochdruckbrücke
	h	Zwischenhoch
High pressure edge	HF	Hoch über Fennoskandien
	HE	Hoch über Osteuropa
Low pressure	TK	Tief über dem Kontinent
	TR	meridionale Tiefdruckrinne
	Vb	Tief Adria-Polen
Low pressure edge	TS	Tief im Süden
	TSW	Tief im Südwesten
	TwM	Tief im westlichen Mittelmeer
	TB	Tief über den britischen Inseln
Linear upper air flow	N	Nordströmung
	NW	Nordweströmung
	W	Weströmung
	SW	Südweströmung
	S	Südströmung
	G	Gradientenschwach

2.4 Atmospheric instability

The large- and synoptic-scale circulation can provide the required environment for extreme precipitation to occur (Barlow et al., 2019). As extreme precipitation is commonly associated with convective rainfall, three basic ingredients are needed: instability, moisture and a lifting mechanism (Doswell et al., 1996).

Since pressure decreases with height, an air parcel, which is moved upward, will expand and thus perform work and consume energy. If the amount of heat in the air parcel stays unchanged, such a process is called adiabatic and the energy needed will be taken by reducing the temperature of the parcel. In the atmosphere, such processes will usually be (approximately) adiabatic (Iribarne and Godson, 1981). This allows the derivation of the rate of the temperature change with height of a rising air parcel, called adiabatic lapse rate. For dry air it is

$$\Gamma_d \equiv -\frac{dT}{dz} = \frac{g}{c_p} = 0.98\ K/100\ m, \tag{2.4}$$

where g is the gravitational acceleration and c_p the specific heat capacity. Since air can hold less moisture at lower temperatures according to the Clausius-Clapeyron relationship, rising and thus cooling moist air will eventually be saturated and start to condensate. This will release latent heat, counteracting the cooling effects of the expansion. The lapse rate of saturated moist air will therefore be lower than the dry adiabatic lapse rate:

$$\Gamma_s \equiv -\frac{dT}{dz} = \Gamma_d \frac{1+\frac{Lw_s}{RT}}{1+\frac{L^2 \epsilon w_s}{Rc_p T^2}} \approx 0.65\ K/100\ m. \tag{2.5}$$

L depicts the latent heat, w_s the saturation mixing ratio, R the individual gas constant and T the temperature of the parcel. Because of the temperature dependency, the moist adiabatic lapse rate is not constant throughout the troposphere. It deviates the strongest from the dry adiabatic lapse rate at high temperature, i.e. the lower troposphere and approaches the dry adiabatic lapse rate with decreasing temperatures, i.e. in the upper troposphere.

The stability of the atmosphere is determined by its temperature gradient, i.e. the lapse rate Γ of the environment compared to the dry and moist adiabatic lapse rates of the air parcel (Barry and Chorley, 1984). Five cases can be distinguished:

$\Gamma < \Gamma_s$ absolutely stable
$\Gamma = \Gamma_s$ saturated neutral
$\Gamma_s < \Gamma < \Gamma_d$ conditionally unstable
$\Gamma = \Gamma_d$ dry neutral
$\Gamma > \Gamma_d$ absolutely unstable

The case of absolute stability is not relevant in this context, as it completely prohibits convection and the development of clouds. Conditions of absolute instability are usually not observed in the atmosphere. As saturated and dry neutral represent only two specific values of Γ, the most relevant case is conditionally instability. This means that a moist air parcel, which is lifted to the height where it becomes saturated and condensation sets in and further to the point where it becomes warmer than its surroundings, would rise freely from this point on until either all the moisture in the parcel is condensated or the atmosphere becomes absolutely stable again. This is the most common case for i.e. the development of thunderstorms. The lifting mechanism is often provided by either local surface heating or by a mountain range, where the air is forced to rise at his slopes. This is especially important in Austria, where the Alps are located. The moister the air, the sooner it will reach the point where condensation sets in.

A commonly used method to quantify the instability of an atmospheric layer is to calculate the convective potential energy (CAPE) in this layer (Holton, 2004), defined as

$$CAPE = \int_{z_{LFC}}^{z_{EL}} g \left(\frac{T_{v,p} - T_{v,e}}{T_{v,e}} \right) dz. \tag{2.6}$$

The integrand is nothing else than the parcel buoyancy, with $T_{v,p}$ and $T_{v,e}$ the virtual temperature of the parcel and the environment and g the gravitational acceleration. It is vertically integrated between the level of free convection (z_{LFC}), where the temperature of the parcel, after condensation set in, exceeds the temperature of the environment, and the equilibrium level (z_{EL}), where the parcel temperature is equal to the environmental temperature again. This calculation assumes no mixing of the rising air with the environment, which would usually reduce the buoyancy and thus CAPE, as the environmental air is not saturated and some of the already liquid water in the parcel has to evaporate to maintain saturation, leading to a cooling effect. Values of CAPE of >2500 J/kg are considered very unstable and only occur in severe midlatitude storms (Holton, 2004; Lynch and Cassano, 2006).

High values of CAPE are not sufficient for deep convection to occur. To release CAPE, the air parcel has first to be lifted to the LFC by a lifting mechanism. The energy required to achieve this is the convective inhibition (CIN). It is calculated analogously to CAPE as

$$CIN = \int_{z_{LCL}}^{z_{LFC}} g \left(\frac{T_{v,p} - T_{v,e}}{T_{v,e}} \right) dz, \tag{2.7}$$

integrated from the lifted condensation level (z_{LCL}) to the LFC. The LCL is the level at which a lifted parcel gets saturated, i.e. where its temperature is equal to its dew point temperature, and condensation sets in. It has a negative value (Westermayer et al., 2017).

Theoretically, CAPE can be directly linked to the expected rainfall rate. As CAPE is a measure of the parcels buoyancy, the theoretical maximum vertical velocity which can be obtained from CAPE is

$$w_{max} = \sqrt{2\ CAPE}. \tag{2.8}$$

Again this does not consider effects of water condensation which reduces the buoyancy (North and Erukhimova, 2009). The rainfall rate is assumed to be proportional to the magnitude of the vertical moisture flux, giving

$$R = Ewq \tag{2.9}$$

for the rainfall rate R, with w denoting the vertical velocity and q the mixing ratio of the rising parcel. E is the precipitation efficiency, taking into account that not all the water vapor has to condensate and precipitate (Doswell et al., 1996). This gives a proportionality between the precipitation intensity and the square root of CAPE:

$$I \sim \sqrt{CAPE} = CAPE^{0.5} \tag{2.10}$$

In reality the exponent will deviate from 0.5 because of entrainment, vertical wind shear and other factors (Lepore et al., 2015).

Several studies have been investigated the relationship between precipitation intensities and CAPE. Lepore et al. (2015) and Lepore et al. (2016) studied rainfall extremes in the United States, finding a slightly weaker relationship as predicted by (2.10), with values between 0.2 and 0.5 for the exponent, depending on the region and the extremeness of the events. Applying the same model to CIN, they found a slightly negative relationship with precipitation intensities. Dong et al. (2019) looked into rainfall extremes over China, finding almost no relationship between precipitation intensities and CAPE. As they mentioned, a reason could be that they used data with only a daily resolution for both precipitation and CAPE which could be insufficient to catch the phase relationship between CAPE and precipitation. Loriaux et al. (2016) studied the relationship between peak precipitation intensities and the atmospheric conditions, including temperature profiles and CAPE, for all precipitation deciles. They found a warmer and more unstable atmosphere for more extreme deciles. For CAPE, a general increase with higher peak intensities was noted, but also a large spread of possible intensities for high percentiles, indicating that the developed CAPE is not always consumed.

In Sec. 4.4, temperature gradients and profiles as well as CAPE and CIN associated with extreme precipitation events will be calculated to investigate possible relationships between those values and the precipitation intensity. A model according to (2.10) will be fitted to the CAPE and CIN values.

Chapter 3

Data and methods

3.1 Data

The following data is used for the analysis: For the jet stream and moisture transport composite analysis (Sec. 4.2) precipitation data is taken from the ZAMG-SPARTACUS dataset (Hiebl and Frei, 2018), which provides daily precipitation over Austria on a 1 km × 1 km grid for the time period 1979-2018. The precipitation data used for the investigation of the influence of large-scale drivers (Sec. 4.1) and weather types (Sec. 4.3) on extreme precipitation over Europe and Austria is the gridded E-OBS precipitation dataset (version 21.0e) (Cornes et al., 2018), with a spatial resolution of 0.25°× 0.25°and spanning the region from 25°N to 71.5°N and 25°W to 45°E. The time period used for analysis is 1950-2018. For the analysis of atmospheric stability during extreme precipitation events in Austria (Sec. 4.4), precipitation data of the ZAMG-INCA dataset is used. It provides the data on a 1 km × 1 km grid every 15 minutes for the time period of 2003-2016. Variables on various pressure levels (temperature, humidity, wind) used in the jet stream, moisture transport and atmospheric stability analyses is provided by the ERA5 global reanalysis (Hersbach et al., 2020). The spatial resolution is 0.25°× 0.25°and the highest temporal resolution 6 hours. The Lauscher series used for weather type classification was provided by ZAMG. The SNAO index is taken from the KNMI Climate Explorer[1] and is based on the NCEP/NCAR R1 reanalysis SLP reconstruction (Kalnay et al., 1996).

3.2 Regions

Fig. 3.1 shows the four Austrian regions, which were chosen for the analysis of the jet stream and moisture transport as well as for the atmospheric stability analysis.

---

[1] https://climexp.knmi.nl/start.cgi (Last access: 07.10.2020)

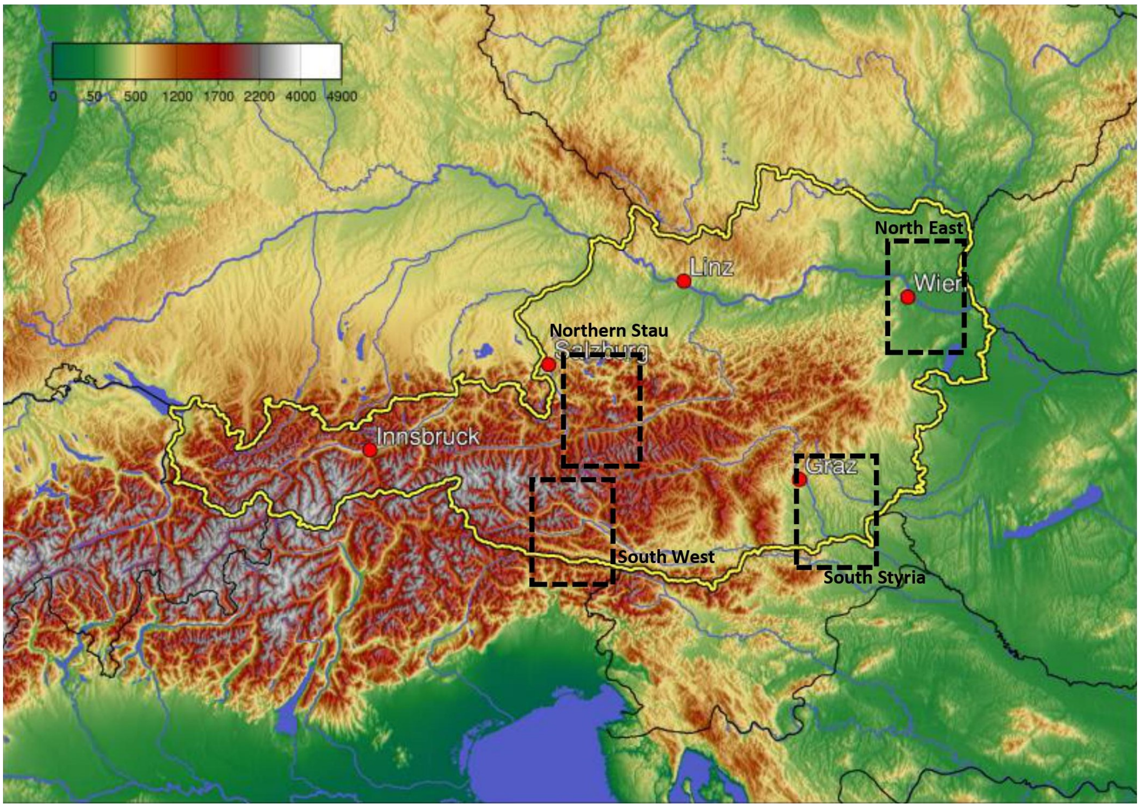

Figure 3.1: The four regions used in the atmospheric stability analysis (Sec. 4.4). The regions used for the jet stream and moisture transport composite analysis (Sec. 4.2) do slightly differ. The grid points at which the seasonal cycle is analysed in Sec. 4.3 lie within those regions. The color map depicts the orography (values in m).

The definition of extreme events within those regions is given in Sec. 4.2 and 4.4, respectively. The analysis of the seasonal cycle of weather type related precipitation (Sec. 4.3) is done for a grid point within the corresponding region.

The regions where chosen based on the results of Seibert et al. (2007), who identified seven regions in Austria with similar time series of daily precipitation sums with a focus on extreme precipitation. The four regions used are subregions of four of the regions found by Seibert et al. (2007). They are named Northern Stau, North East, South Styria and South West.

The regions defined for the jet stream analysis slightly differ from the regions used in the atmospheric stability analysis. In the first case they were designed such that they match the E-OBS grid and in the latter case to match the ZAMG-INCA grid. However, the differences are small and are not expected to have any influence on the results.

3.3 Extreme value theory

Extreme value theory can be used to evaluate data on rare precipitation events. The key result is that maxima of a sample of any distribution can follow only a limited number of limit distributions (Coles, 2001).

Assume there is a sequence of n independent and identically distributed random observations $X_1, ..., X_n$, having a common distribution function F and a maximum M_n, defined as

$$M_n = max\{X_1, ..., X_n\}.$$

In the analysis in Sec. 4.1, the X_i will represent daily precipitation values, i.e. observations on a regular time-scale. n will be the number of observations in one month, thus M_n is the monthly (block) maximum and will be considered as an extreme value.

Theoretically, the distribution of M_n is

$$\begin{aligned} Pr\{M_n < z\} &= Pr\{X_1 <= z, ..., X_n <= z\} \\ &= Pr\{X_1 <= z\} \times ... \times Pr\{X_n <= z\} \\ &= \{F(z)\}^n. \end{aligned}$$

As F is unknown it has to be looked for families of models which approximate F^n for $n \to \infty$ and can be estimated by the extreme data. However, this cannot be done for the distribution of M_n, as $F^n(z) \to 0$ for $n \to \infty$ for any $z < z_+$, where z_+ is the smallest vale such that $F(z) = 1$. Therefore, a linear renormalization of M_n is applied:

$$M_n^* = \frac{M_n - b_n}{a_n},$$

with sequences of constants $\{a_n > 0\}$ and $\{b_n\}$. This stabilizes the location and scale of M_n^* as n increases. The limit distributions of M_n^* are then given by the Fisher-Tippett theorem or extreme value theorem:

If there exist sequences of constants $\{a_n > 0\}$ and $\{b_n\}$, so that

$$Pr\left\{(M_n - b_n)/a_n \leq z\right\} \to G(z) \quad \text{as } n \to \infty,$$

then G can be written as

$$G(z; \mu, \sigma, \xi) = exp\left\{-\left[1 + \xi\left(\frac{z-\mu}{\sigma}\right)\right]^{-1/\xi}\right\}. \tag{3.1}$$

$G(z; \mu, \sigma, \xi)$ is defined on $\left\{z : 1 + \xi\left(\frac{z-\mu}{\sigma}\right)\right\}$, where $-\infty < \mu < \infty$, $\sigma > 0$ and $-\infty < \xi < \infty$ and is known as the generalized extreme value (GEV) family of distributions.

The three parameters are the location parameter μ, describing the position, the scale parameter σ describing the width and the shape parameter ξ describing the tail. From ξ three different distributions can be distinguished: for $\xi < 0$ it is called a Weibull distribution, which has an upper finite value ("bounded") and for $\xi > 0$ it is the Fréchet distribution, where the tail decays polynomially ("heavy-bounded"). For $\xi \to 0$, (3.1) leads to the Gumbel distribution with distribution function

$$G(z;\mu,\sigma) = exp\left\{-exp\left\{\left(\frac{z-\mu}{\sigma}\right)\right\}\right\}. \tag{3.2}$$

It has a exponentially decaying tail ("light-bounded") (see Fig. 3.2).

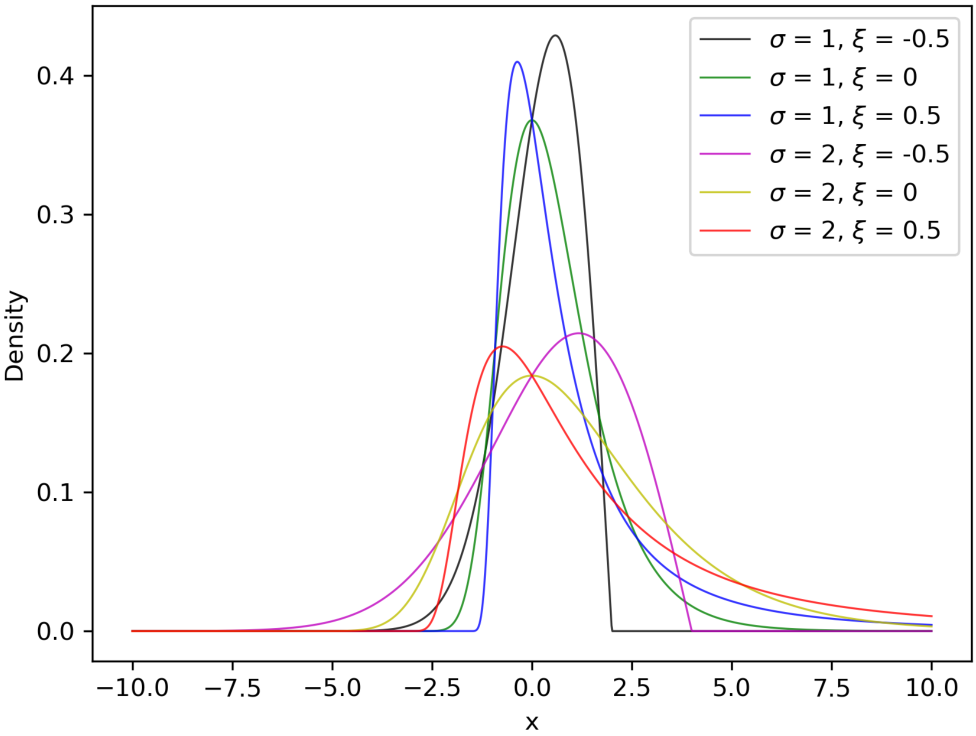

Figure 3.2: GEV distributions for different values of ξ and σ, with $\mu = 0$.

This now can be used to model extreme values, i.e. block maxima of a time series. The time series is divided into blocks of length n and the maximum of each block is determined. According to the Fisher-Tippet theorem, the obtained maxima approximately follow a GEV distribution of the form (3.1), if the chosen block length is large enough. Therefore, the parameters of the distribution can be estimated from the block maxima. In climatology, common block lengths are one month to one year, to get a reasonable trade-off between a large enough block length so that the Fisher-Tippet theorem is applicable and at the same time a large enough sample of maxima to keep the variance of the parameter estimation low (Ben Alaya et al., 2020).

There are several methods to estimate the parameters of the distribution (3.1), including L-moments, Bayesian methods and graphical methods (Šimková and Picek, 2017; Lima et al., 2016). The most common choice however, is to use maximum likelihood estimation, i.e. to find those parameters which maximize the likelihood with respect to the available data. A great advantage of using the maximum likelihood method is that it allows to include non-stationarity and covariate dependence in the model in a straightforward way (Coles, 2001).

The log-likelihood function of the GEV parameters is

$$l(\mu,\sigma,\xi) = -m{*}log(\sigma) - (1+1/\xi)\sum_{i=1}^{m} log\left[1+\xi\left(\frac{z_i-\mu}{\sigma}\right)\right] - \sum_{i=1}^{m}\left[1+\xi\left(\frac{z_i-\mu}{\sigma}\right)\right]^{-1/\xi}, \tag{3.3}$$

where z_i are variables having the GEV distribution.

The case $\xi = 0$ has to be treated separately. This leads to the log-likelihood

$$l(\mu,\sigma) = -m * log(\sigma) - \sum_{i=1}^{m}\left(\frac{z_i-\mu}{\sigma}\right) - \sum_{i=1}^{m} exp\left\{-\left(\frac{z_i-\mu}{\sigma}\right)\right\}. \tag{3.4}$$

The estimated parameters are those that maximize (3.3) and (3.4). Since there are no analytical solutions, numerical optimization methods have to be used.

The block maxima approach has the disadvantage that, since only one (or a certain amount) of values per block can be considered extreme, there are potentially values which are not extreme in their block but would be in another. This means that the n block maxima most likely are the n most extreme values of the entire time series. To avoid not using a large fraction of the data, another possibility to define extreme values would be to define a threshold u, and consider all values above this threshold as extreme. This is called the peaks-over-threshold approach. The downside of this method is that, unlike in the block maxima approach, the extreme values may not represent distinct events, since the underlying data may exhibit serial correlation. This problem is often solved by applying declustering methods or by using e.g. only the single largest of consecutive values above the threshold (Coles, 2001).

From the peaks-over-threshold definition of extreme values follows a different distribution function of these values than with the block maxima definition. Let $X_1, ..., X_n$ be again a sequence of independent and identically distributed variables and u the threshold which has to be exceeded to consider a value to be extreme. Then it can be shown that for large enough u, the exceedances $Y = X - u$, conditional on $X > u$, follow the Generalized Pareto Distribution (GPD), with the distribution function

$$H(y) = 1 - \left(1 + \frac{\xi y}{\sigma + \xi(u-\mu)}\right)^{-1/\xi} \tag{3.5}$$

defined on $\{y : y > 0 \text{ and } (1 + \xi y/(\sigma + \xi(u - y))) > 0\}$. This distribution consists of a scale parameter σ and shape parameter ξ. Similar to the GEV distribution the GPD has an upper bound for $\xi < 0$ and no upper limit for $\xi > 0$ and $\xi \to 0$.

As for the choice of the block length n in the block maxima approach, the choice of the threshold u in the peaks-over-threshold approach has to be a trade-off between a large enough u so that (3.5) can be assumed to be the approximated distribution of the extreme values and a small enough u so that there is still a large sample of extremes. In Sec. 4.3.1 the GPD will be used to investigate the behaviour of extreme values on days where a certain weather type occurred.

Once the parameters of the distribution has been fitted, return levels can be calculated. For extremes following a GEV distribution, the return level z_p is obtained by inverting (3.1):

$$z_p = \begin{cases} \mu - \frac{\sigma}{\xi}\left[1 - \{-log(1-p)\}^{-\xi}\right], & \text{for } \xi \neq 0 \\ \mu - \sigma * log\{-log(1-p)\}, & \text{for } \xi = 0 \end{cases} \tag{3.6}$$

z_p is the value which is expected to be exceeded exactly once per period $1/p$.

For extremes following a GPD, the return level is given by

$$x_m = u + \frac{\sigma}{\xi}\left[(m\zeta_u)^{\xi} - 1\right] \tag{3.7}$$

for m large enough to ensure $x > u$. ζ_u is the probability that $X_i > u$. x_m has a similar meaning as z_p, giving the value which is expected to be exceeded exactly once every m observations. x_m is also called the m-observation return level.

3.4 Modeling of non-stationary processes

The previous considerations all assumed independence of the underlying variables and therefore a constant distribution function through time. However, in practical applications, this is often not the case. In climatology, the values of a time series could depend on time because of seasonal effects or long-term climate changes, which would lead to a trend in the data.

Another possibility would be that the behaviour of the time series is related to that of an external driver. In Sec. 4.1 , a possible influence of large-scale drivers like the Summer North Atlantic Oscillation on extreme precipitation in Europe will be investigated.

To model the influence of an external driver on a dependent variable, often regression models are used. A popular class of regression models are generalized linear models (GLMs). In these models, the expected value of the dependent variables is given by

$$E(\boldsymbol{Y}) = \boldsymbol{\mu} = g^{-1}\left(\boldsymbol{X}\boldsymbol{\beta}\right), \tag{3.8}$$

where $\boldsymbol{Y}$ are the dependent variables, $\boldsymbol{X}$ are the independent variables or covariates, $\boldsymbol{\beta}$ is the parameter vector and $g(.)$ is a link function. However, as the distribution of the dependent variables in GLMs has to be part of the exponential family, these models are not suitable to model the parameters of a GEV distribution or a GPD (Coles, 2001). Therefore, GLMs have been extended to so called vector generalized linear models (VGLMs), which allows for modeling a vector of parameters of a wider class of distributions, including the GEV distribution and the GPD (Yee and Wild, 1996). In the analysis of the large scale drivers, the location and scale parameter will be modelled as linear dependent on an index of the external driver (the covariate COV):

$$\begin{aligned} \mu(t) &= \mu_0 + \mu_1 * COV(t) \\ \sigma(t) &= \sigma_0 + \sigma_1 * COV(t) \\ \xi(t) &= \xi_0 \end{aligned} \tag{3.9}$$

Since the shape parameter is difficult to estimate and would lead to high uncertainties due to the limited number of observations in the tail, it will be kept constant (Maraun et al., 2009; Rust et al., 2009). The estimation of the five parameters μ_0, μ_1, σ_0, σ_1 and ξ_0 using the maximum likelihood method is similar to the stationary case, by just replacing the parameters in (3.3) with the expressions in the model given by (3.9).

Chapter 4

Results and Discussion

4.1 Large-scale drivers

In the following, the influence of the SNAO, SEA, tropical precipitation and the Indian Summer Monsoon on extreme precipitation over Europe will be investigated. Therefore, a statistical model is developed which uses the corresponding index of the driver as predictor for the GEV distribution of monthly precipitation maxima.

Monthly precipitation maxima are computed for the period 1979-2018 for the months June, July and August (JJA) and at each grid point, respectively. To model these block maxima, the GEV distribution is used (see Sec. 3.3). The influence of the driver on extreme precipitation is modeled by using a VGLM. A simple linear dependence of the GEV parameters μ and σ on the index is assumed. The shape parameter ξ is kept constant, as it is difficult to estimate due to the limited number of observations in the tail of the distribution and would lead to high uncertainties (Maraun et al., 2009; Rust et al., 2009).

The statistical model for the GEV parameters therefore is given by (3.9), where *COV* is replaced by the index of the driver, respectively. All indices were detrended prior to analysis. The parameters are obtained via maximum likelihood estimation.

4.1.1 Summer North Atlantic Oscillation

Fig. 4.1 shows the parameter μ_0 of the statistical model, giving the location of the GEV distribution at a SNAO index of zero. The highest values are obtained in the Alps and along the the west coast of Norway.

The scale parameter σ_0 (Fig. 4.2) has its highest values in Slovenia and southern Austria along the southern slope of the Alps. In general, regions with high values are found in the vicinity of mountain ranges, e.g. the northern foothills of the Alps, the Po valley, along the Carpathians and the southern coast of Norway.

The shape parameter ξ_0 (Fig. 4.3) does exhibit mostly positive values, but significant only in some parts of Great Britain, Eastern Europe and along the Mediterranean coast and a broader area centered at the border of Germany and Poland. Individual points of significantly negative values are obtained in Russia and the Balkans. As explained in Sec. 3.3, a more positive shape parameter means a heavier tailed GEV distribution, making very extreme values more likely.

Fig. 4.4 shows the regression coefficient μ_1, giving the actual influence of the SNAO on the location parameter of the extreme value distribution. Negative values correspond to a shift of the location parameter to lower values for high SNAO indices, meaning that the precipitation events become less extreme on average. Vice versa, positive values stand for increasing extreme precipitation values. Regions where the parameter deviates from zero significantly at the 95% level are hatched.

The large-scale pattern follows roughly the results which where already found for the influence of the SNAO on mean summer precipitation (Bladé et al., 2012). Regions of negative influence are spanning from the British Isles over the Benelux countries, Northern Germany and large parts of Scandinavia to the Baltic states. Positive values cover the entire Mediterranean area, with maximum values over Italy and the Western Balkans. The results over southern Spain, northern Africa and the Middle East were not included, as in these regions the station coverage is scarce (Cornes et al., 2018) and precipitation values may be too low to fit a GEV distribution.

Interestingly, Fig. 4.4 shows rather strong and significant negative values also over the alpine region. Previous studies dealing with mean precipitation did not find significant influence in this region as it lies in the transition zone between negative influence over northern Europe and positive influence in the Mediterranean (Chronis et al., 2011; Bladé et al., 2012).

The change of the scale parameter under influence of the SNAO (Fig. 4.5) does not show large significant regions. There are some significantly negative values in Sweden, Poland and Belarus. Negative values can be seen in Italy, Greece and in Russia. This suggests that in regions where there is a negative influence of the SNAO on the location parameter of the distribution, also the shape parameter tends towards lower values and vice versa.

The significant values of μ_1 found over the Alps may be caused by the fact that in the alpine region extreme precipitation values are generally high (see Fig. 4.1). Changes of the same magnitude as in regions where the extreme values are lower do not indicate a similar influence of the SNAO in terms of sensitivity. Therefore, a sensitivity value is computed, defined as

$$Sensitivity = \frac{z_{p_+} - z_{p_-}}{z_{p_0}}. \tag{4.1}$$

z_{p_+}/z_{p_-} stands for the return level evaluated for the estimated GEV parameters at the SNAO-index value of $+var(SNAO)/-var(SNAO)$ and z_{p_0} for the return value where the SNAO-index is zero. The return levels are computed according to (3.6). Since they are dependent on all three GEV distribution parameters this should furthermore give also more complete idea of the impact of the SNAO on extreme precipitation.

Fig. 4.6 shows the sensitivity of the 10-year return level on the SNAO. The strongest values are obtained where the change of both the location and shape parameter with the SNAO are strongest and have the same sign. The highest sensitivities are therefore obtained in southern Italy and in Greece and the lowest in Sweden, Belarus, the Baltic States and in Scotland. As expected, the pattern does resemble the north-south dipole found for the regression coefficient of the location parameter, as the scale parameter change and the shape parameter are low in many regions and therefore do not contribute as much to the return values. However, in some regions the scale and shape parameters do significantly counteract the location parameter in terms of return values. The significant negative values found for the regression coefficient of the location parameter in the alpine region (see Fig. 4.4) are somewhat relativized when looking at the sensitivities, but there is still significant negative sensitivity in the central Alps, indicating that the SNAO might influence extreme precipitation also in regions where there was no significant influence found on mean precipitation.

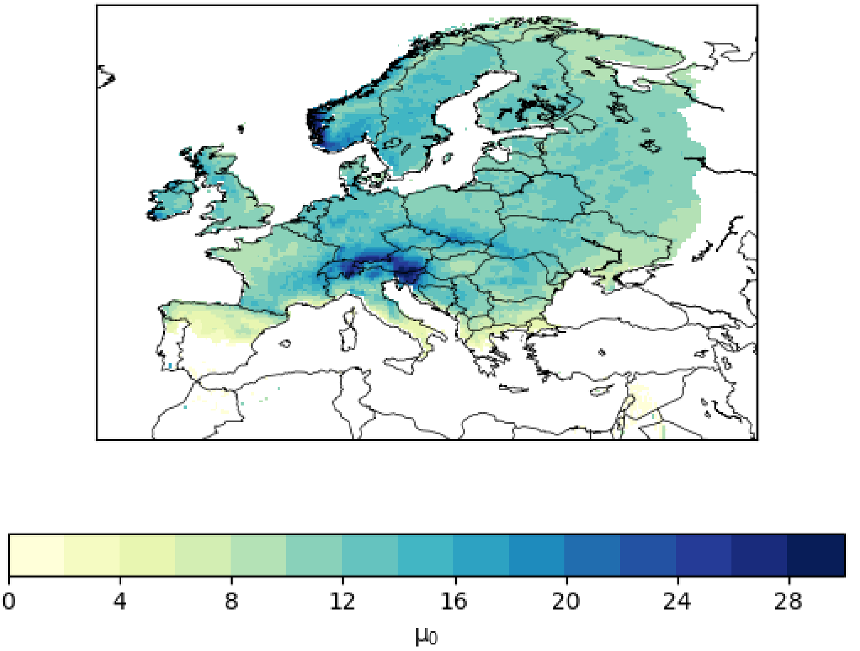

Figure 4.1: Parameter μ_0 of the statistical model

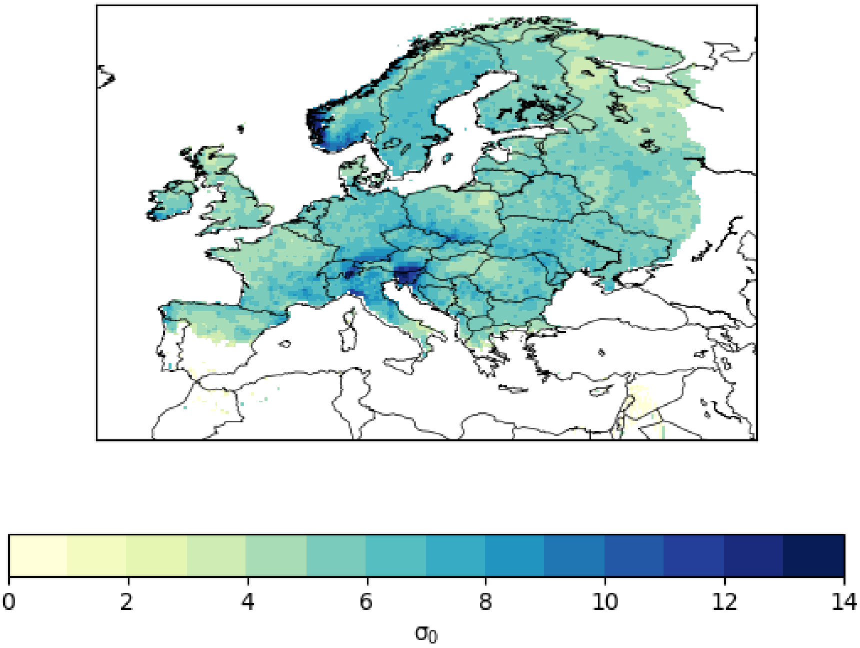

Figure 4.2: Parameter σ_0 of the statistical model

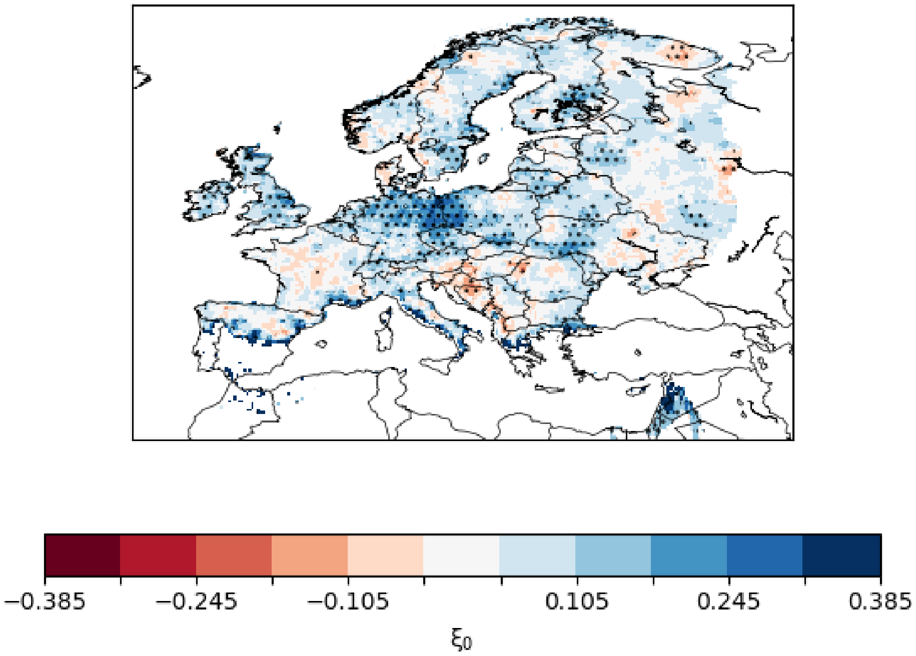

Figure 4.3: Parameter ξ_0 of the statistical model. Values which are significantly different from zero are stippled.

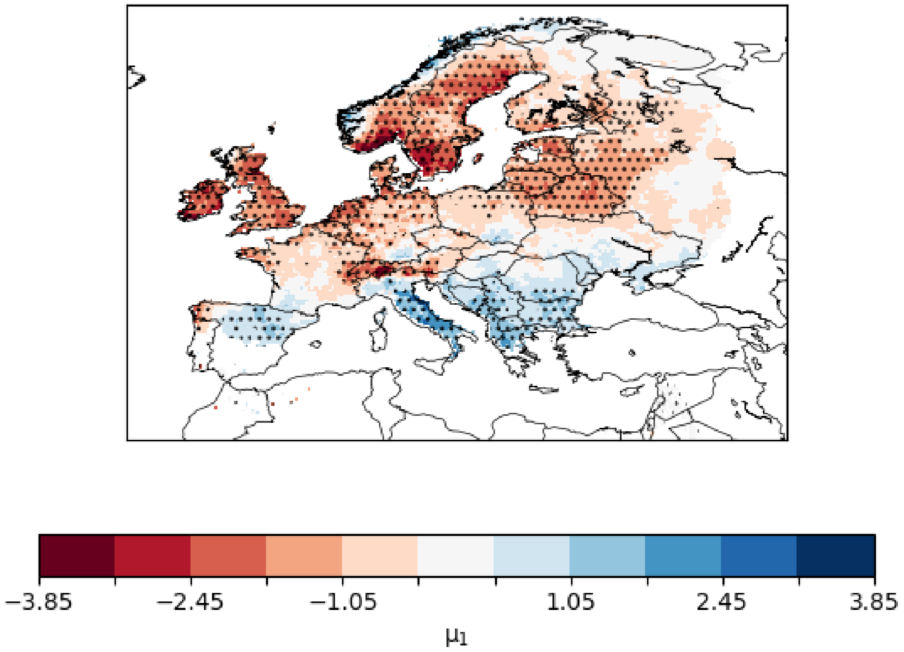

Figure 4.4: Regression coefficient μ_1 of the statistical model with the SNAO as covariate. Values which are significantly different from zero are stippled.

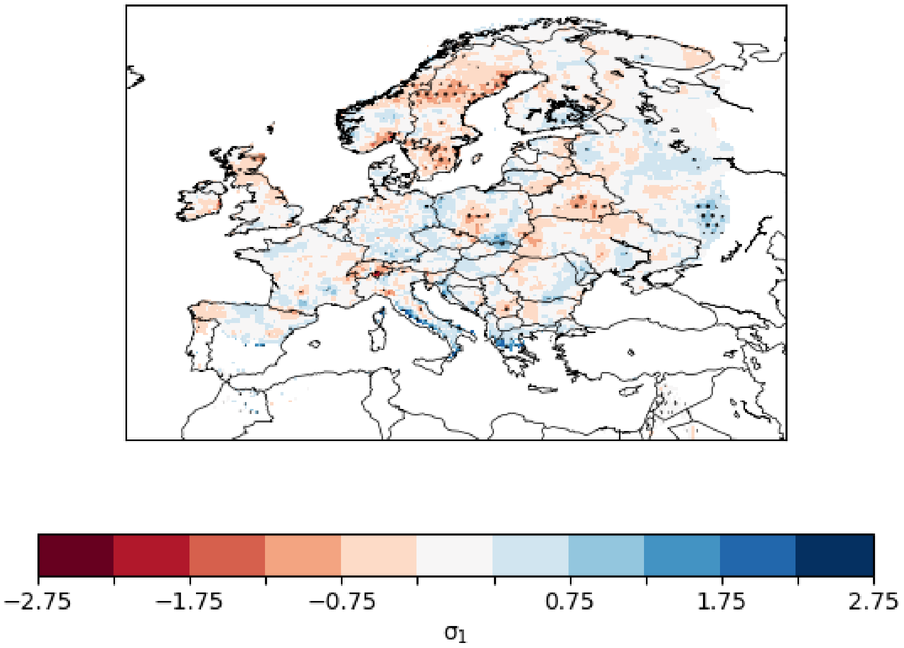

Figure 4.5: Regression coefficient σ_1 of the statistical model with the SNAO as covariate. Values which are significantly different from zero are stippled.

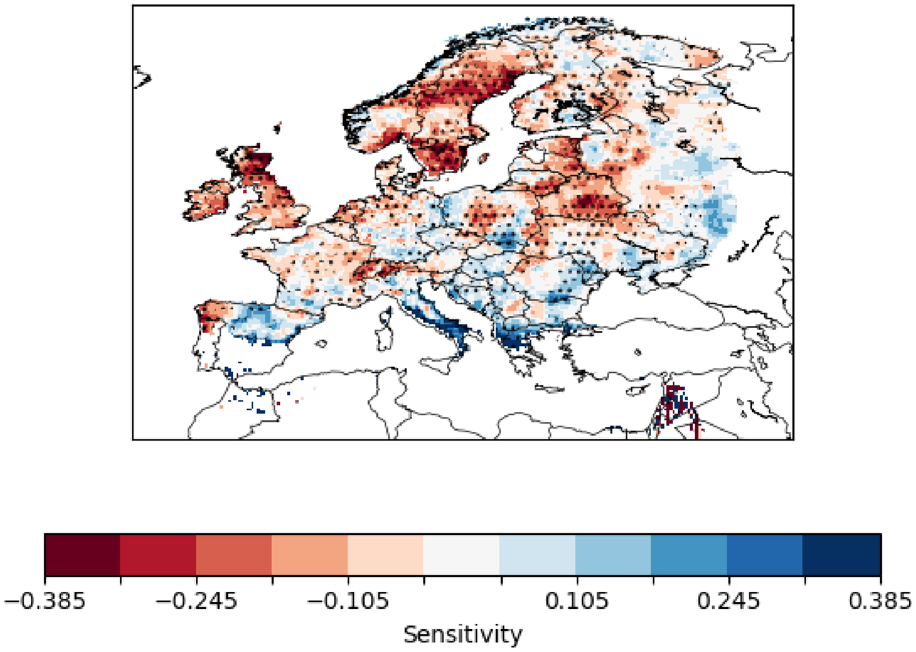

Figure 4.6: Sensitivity of the 10-year return level on the SNAO. Values which are significantly different from zero are stippled.

4.1.2 Summer East Atlantic pattern

The SEA index was obtained by applying an EOF analysis to ERA5 JJA seasonal mean 500 hPa geopotential height anomalies relative to the 1979–2018 JJA climatological mean. The resulting second leading EOF is identical to those found by Wulff et al. (2017) (not shown).

Fig. 4.7 shows the regression coefficient μ_1 of the location parameter. Significant areas of negative influence are obtained from Poland over the Baltic States, Belarus and Ukraine to Russia. Other significant negative areas are seen in Slovenia and Croatia, as well as around the Elsass. In Ireland, the Scottish Highlands and along the west coast of Norway, there are significant positive values. This pattern is comparable to the results found by Wulff et al. (2017) for mean precipitation, where negative regression coefficients where found in a large area around the Baltic Sea. By comparison, the pattern here is slightly shifted towards southeast and the significant negative values cover a smaller area.

The regression coefficient σ_1 (Fig. 4.8) of the scale parameter does not exhibit wider areas of significant values. Individual significant points are found for instance in Romania, Russia, Sweden, in the Pyrenees and in the Alps.

The pattern of the sensitivity of the 10-year return level on the SEA (Fig. 4.9 is therefore very similar to the pattern of the regression coefficient μ_1. The most sensitive regions are in eastern Europe, especially in Poland, Ukraine and western Russia. Strong negative sensitivities can be seen in Scotland, Norway, north Sweden and around the Pyrenees.

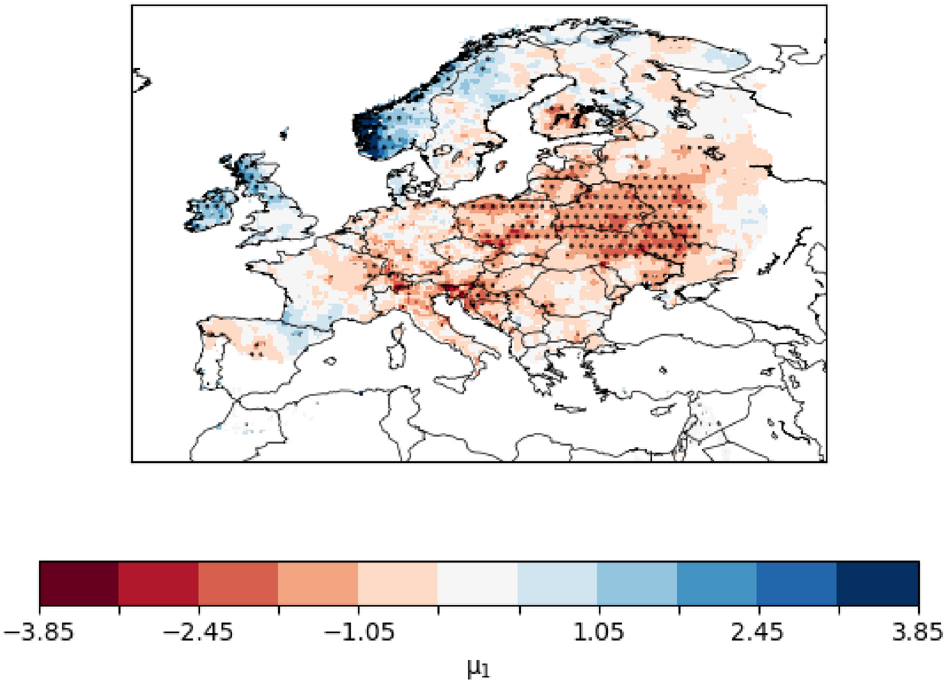

Figure 4.7: As Fig. 4.4 with the SEA index as covariate.

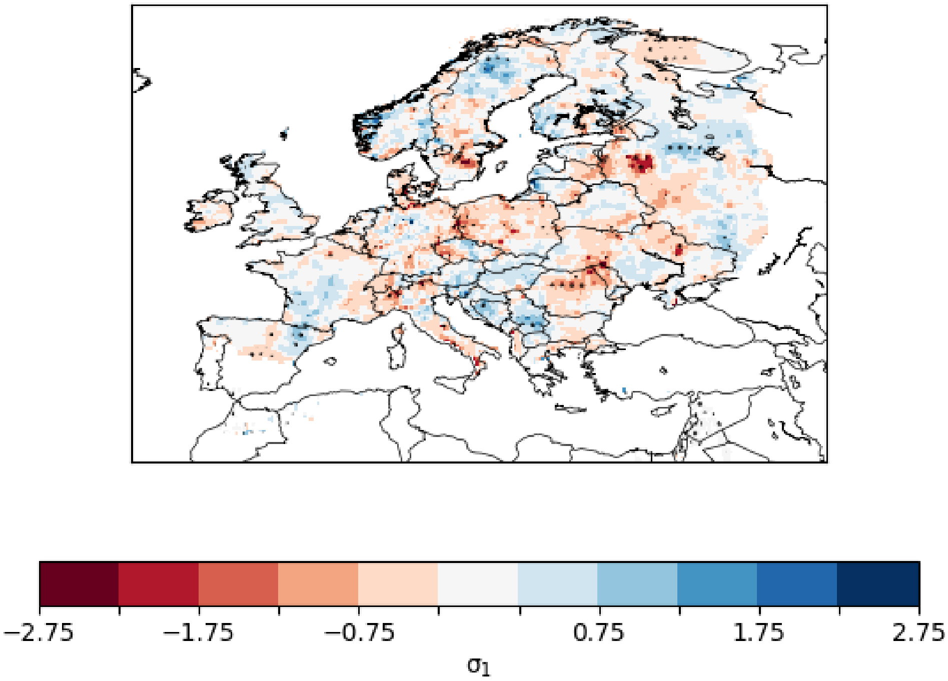

Figure 4.8: As Fig. 4.5 with the SEA index as covariate.

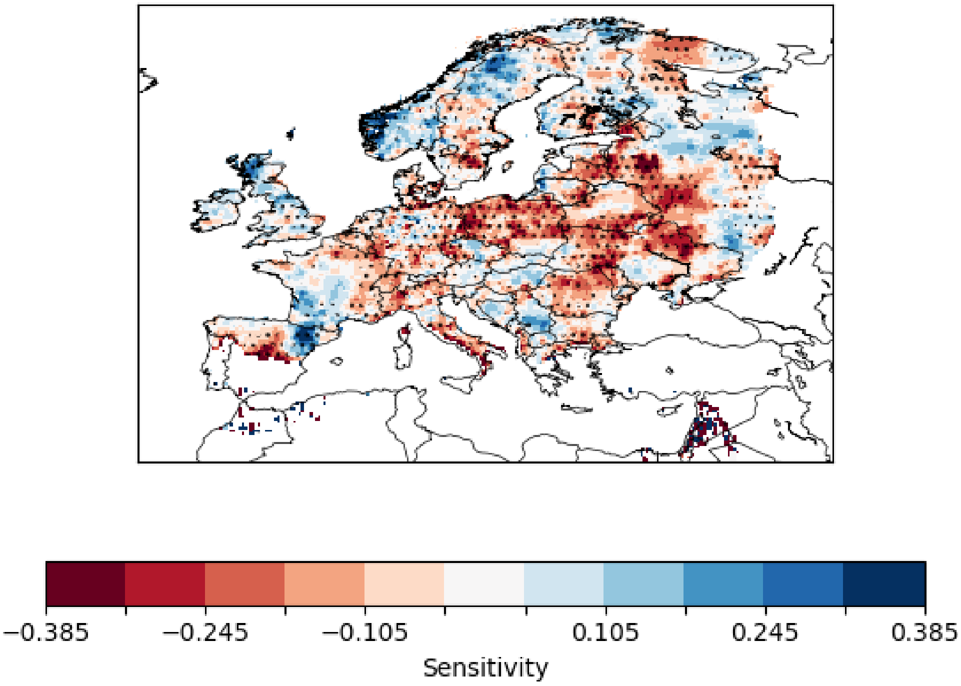

Figure 4.9: As Fig. 4.6 for the SEA index.

4.1.3 Tropical Precipitation

In Fig. 4.10, the influence of tropical precipitation index on the location parameter of the GEV distribution is shown. Regions of significant negative influence are in the Ukraine and along the coast of the Black Sea as well as in northern Spain. Significant positive values are obtained in Norway and the northern parts of Scandinavia as well as south of the White Sea in Russia.

The map of the change of the scale parameter (Fig. 4.11) does show one pronounced region of significant negative values in northern Belarus and stretching through Russia to the White Sea. Some significant negative values are found along the german Baltic Sea coast and in Russia north of the White Sea.

The resulting sensitivity map of the 10-year return level (Fig. 4.12) does show the highest (positive) sensitivities in the same region where there are the also the strongest positive values of the regression coefficient of the scale parameter, covering Belarus and a band through Russia towards the White Sea. Other areas of high positive sensitivity are found in Norway, in East of England and a little bit weaker also around Bulgaria. Positive sensitivity can be seen in northern Spain, the german and polish Baltic Sea coasts, in Russia north of the White Sea and northeast of Moscow and in the Ukraine near the Black Sea. Interestingly, the high values in

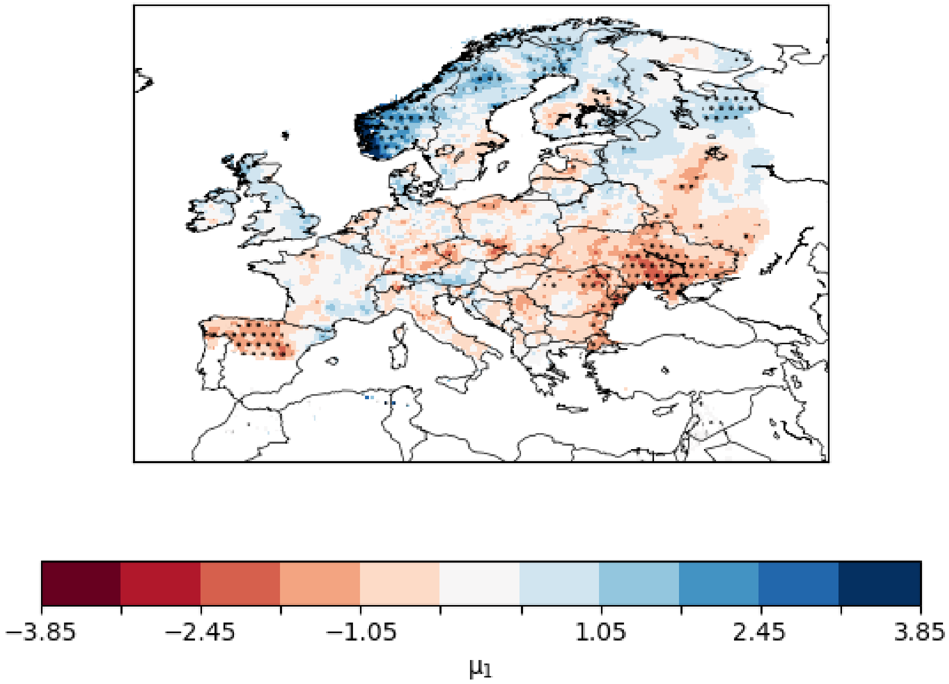

Figure 4.10: As Fig. 4.4 with the tropical precipitation index as covariate.

northern Belarus are not significant, which might be due to abnormal high errors in the parameters in this region.

As Wulff et al. (2017) showed that the tropical precipitation dipole represented by the index used here in the regression model does produce the SEA pattern, one would expect similar results on the influence of tropical precipitation on the GEV distributions as for the SEA index. However, when comparing Fig. 4.10-4.12 to Fig. 4.7-4.9, the results differ substantially. The pattern of the response of the location parameter to tropical precipitation is shifted towards south-east compared to the SEA. The significant regions in Belarus and Russia of the change of the scale parameter due to tropical precipitation are not present in the response to the SEA, resulting in the different patterns for the sensitivity.

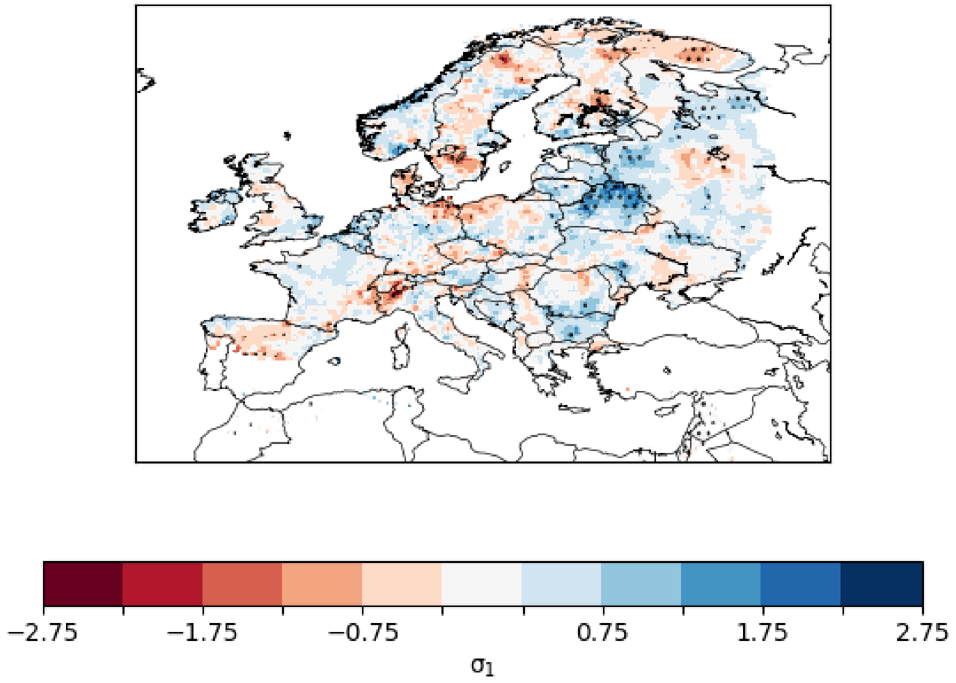

Figure 4.11: As Fig. 4.5 with the tropical precipitation index as covariate.

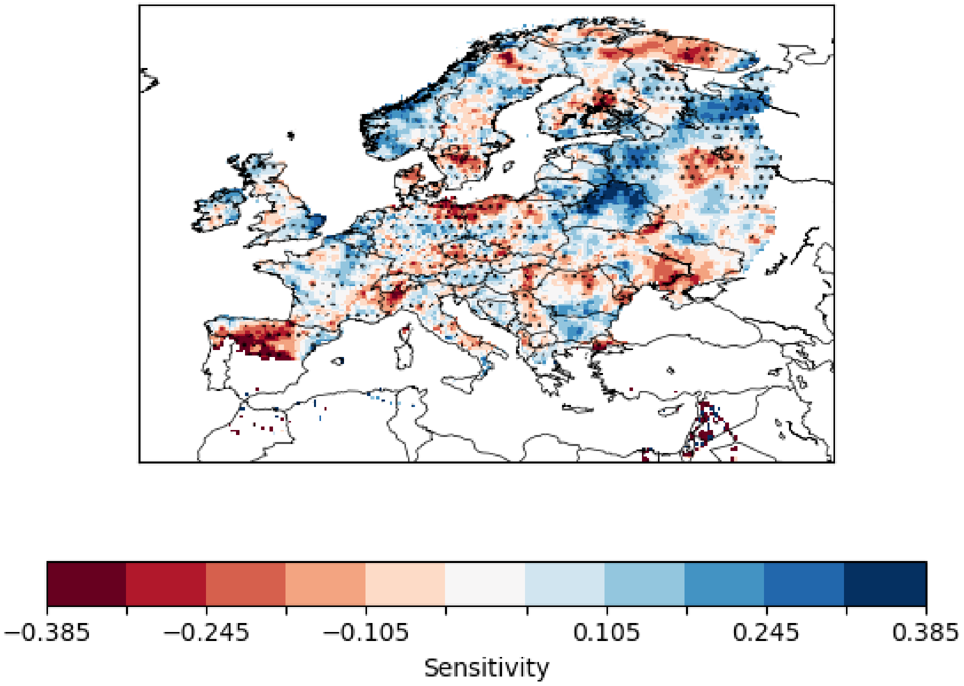

Figure 4.12: As Fig. 4.6 for the tropical precipitation index.

4.1.4 Indian Summer Monsoon

The precipitation index used to represent the Indian Summer Monsoon is calculated as in Ossó et al. (2019). The precipitation data is taken from the Global Precipitation Climatology Project version 2.3 (Adler et al., 2018), providing monthly-mean precipitation data with a resolution of 2.5°× 2.5°. The index is calculated by averaging JJA precipitation over a box spanning 70°E to 105°E, 8°N to 35°N, representing the time and area of the Indian Summer Monsoon.

The results obtained by the statistical model for the GEV parameters are shown in Fig. 4.13-4.15. The regression coefficient μ_1 (Fig. 4.13) shows a rather weak dipole pattern, with significant negative values along the cost of the Mediterranean and mostly positive values elsewhere, which are significant only in some areas over Scandinavia and in a broader region over western and northern Poland and eastern Germany.

When looking at the change of the scale parameter (Fig. 4.14), significant negative values can be seen in the same regions where also the location parameter is decreasing, especially in western Poland/eastern Germany. Another region of significant negative values is found along the west coast of the Black Sea. Regions of positive values are much rarer and significant only in southern Italy.

The map of the sensitivity on the 10-year return level (Fig. 4.15) therefore does show mostly positive values, meaning that the Indian Summer Monsoon does enhance extreme precipitation in large parts of Europe. The highest sensitivities are obtained in a region centered in western Poland, where both the location and the shape parameter of the GEV distribution are increasing with a higher Indian Summer Monsoon index and along the coast of the Black Sea, where, though the location parameter does decrease in some parts, the higher shape parameter leads to an overall increase of the return levels. Regions of strong negative sensitivities are along the Mediterranean coast of Spain, France, Italy, in East England and the western Balkans.

The significant results over the western Mediterranean and especially over western Poland and eastern Germany are surprising, as the Indian Summer Monsoon was only known to influence precipitation over the eastern Mediterranean and the Balkans (Ossó et al., 2019). Indeed, a shift of the GEV distribution towards less extreme values can be seen on the Balkans (Fig. 4.13). However, a significant negative sensitivity of the 10-year return level is only found at the coast of the Adriatic Sea, because of the (slightly) positive values of the scale parameter, especially towards the Black Sea (Fig. 4.14). The reason for the significant increase of both location and scale parameter in western Poland and eastern Germany remains unclear.

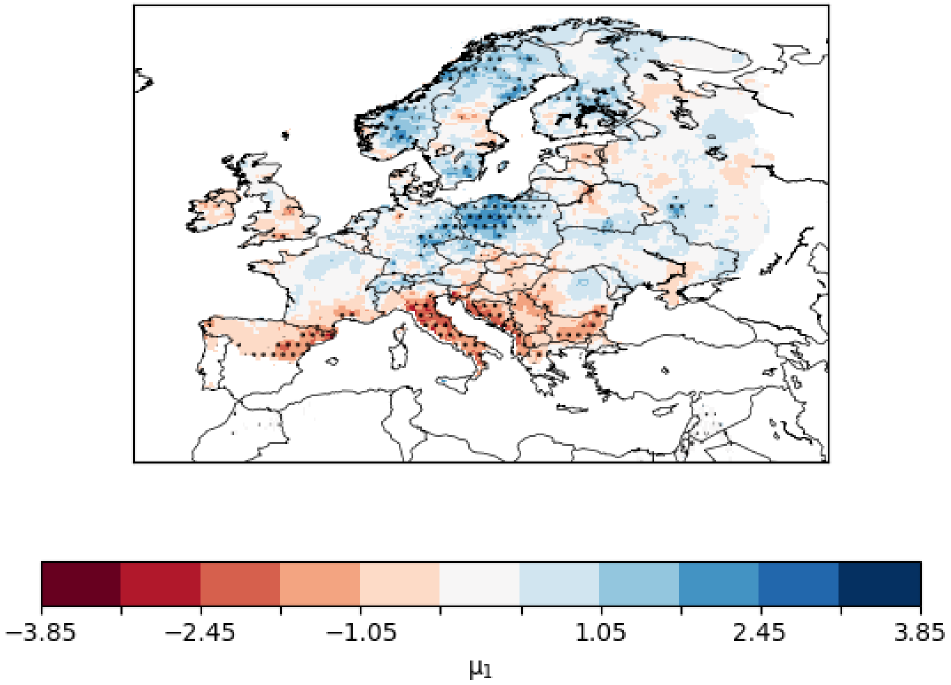

Figure 4.13: As Fig. 4.4 with the Indian Summer Monsoon index as covariate.

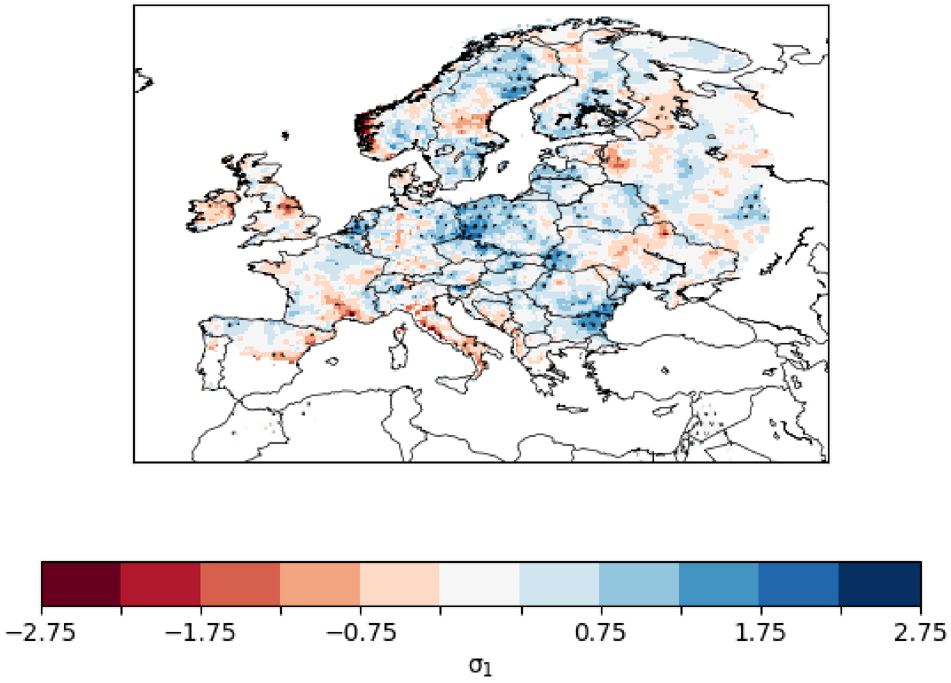

Figure 4.14: As Fig. 4.5 with the Indian Summer Monsoon index as covariate.

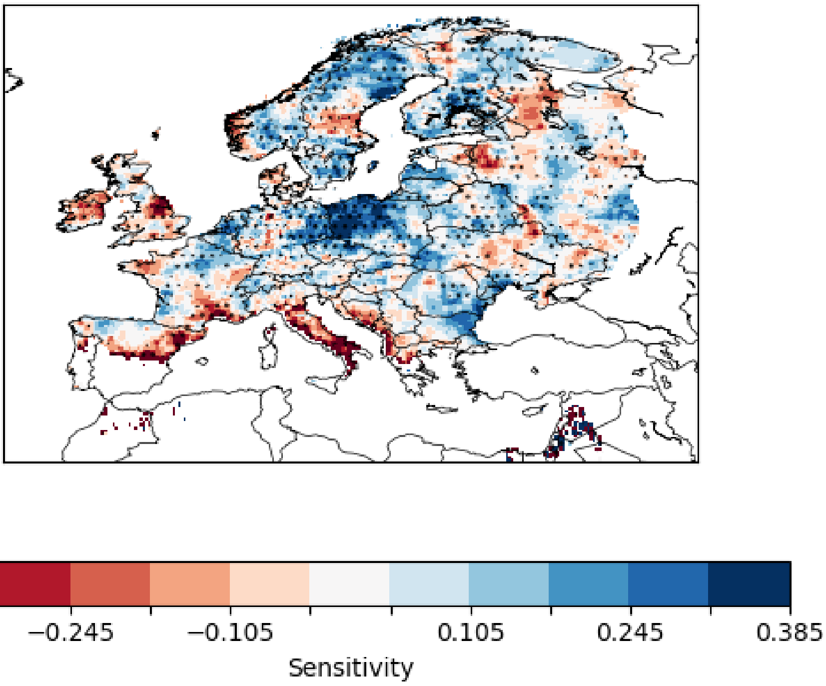

Figure 4.15: As Fig. 4.6 for the Indian Summer Monsoon index.

4.2 Jet stream and moisture transport

To analyse the behaviour of the jet stream during extreme precipitation events in Austria, a composite analysis is conducted. The daily values of the precipitation data are averaged over 4 different regions in Austria (see Fig. 3.1), which were chosen to represent the different synoptic conditions responsible for extreme precipitation in these regions. Consecutive days with precipitation exceeding 1 mm in the resulting time series are assumed to originate from the same synoptic condition and are considered as one event. This means that between two events there must be at least one day with precipitation less than 1 mm. Extreme precipitation events are then defined as the 18 strongest events of daily precipitation for each region and each season.

Composite maps of wind speed at 300 hPa, representing the jet stream, are calculated for the days of the events for each region and each season separately.

The results are shown in Fig. 4.16 to 4.19. Regions were the wind speed is not significantly different at the 95% level from the climatology are hatched. The arrows indicate the wind direction. At the top right corner of the plots the most frequent Lauscher Class of the event days is given, indicating the synoptic condition. The number of total occurrences and availability of the Lauscher Class at the event days is also indicated.

Between the individual regions the obtained composite plots show large differences. Within one region, the differences between the seasons are usually much less pronounced. For the South Styrian region, the most pronounced results are found for autumn. The jet stream lies in a narrow band exhibiting a wave-like motion, with north-westerly flow (equatorward) coming from the Atlantic into Europe and turning into north-easterly direction (poleward) over the Alps, which builds a shallow trough over western Europe. In winter, this trough is more pronounced and shifted southward, while the band width gets wider. In summer the equatorward part is quite similar to autumn, while the poleward is much weaker than in autumn or summer. In spring, there is still a weak poleward flow from the Mediterranean over Austria into Poland visible, while the equatorward part is completely missing.

For extreme events over the North East region, significant results are absent for winter and also very limited for the other seasons. In spring and winter, a westerly flow of the jet stream over the Mediterranean can be identified. In autumn, there is north-westerly flow from the British Isles over France into the Mediterranean.

Extreme events in the Northern Stau region in winter are clearly accompanied by a arc-shaped jet stream flow from the North Atlantic over the North Sea in central Europe into the Mediterranean. The same pattern is seen in spring with weaker wind speeds. In autumn, this pattern is slightly shifted to the south-west, with even weaker wind speeds. In summer, the jet stream builds almost a half circle around the Alps, but the results are less pronounced.

The results for the South West region are almost similar in shape and strength over the different seasons. The jet stream flow builds a trough over western Europe, with north-westerly winds over the East Atlantic and Iberia and turning into a south-west to north-east flow spanning from the western Mediterranean over the Alps up to the Baltic Sea. In summer, this pattern is slightly shifted northward and the wind speeds are weaker.

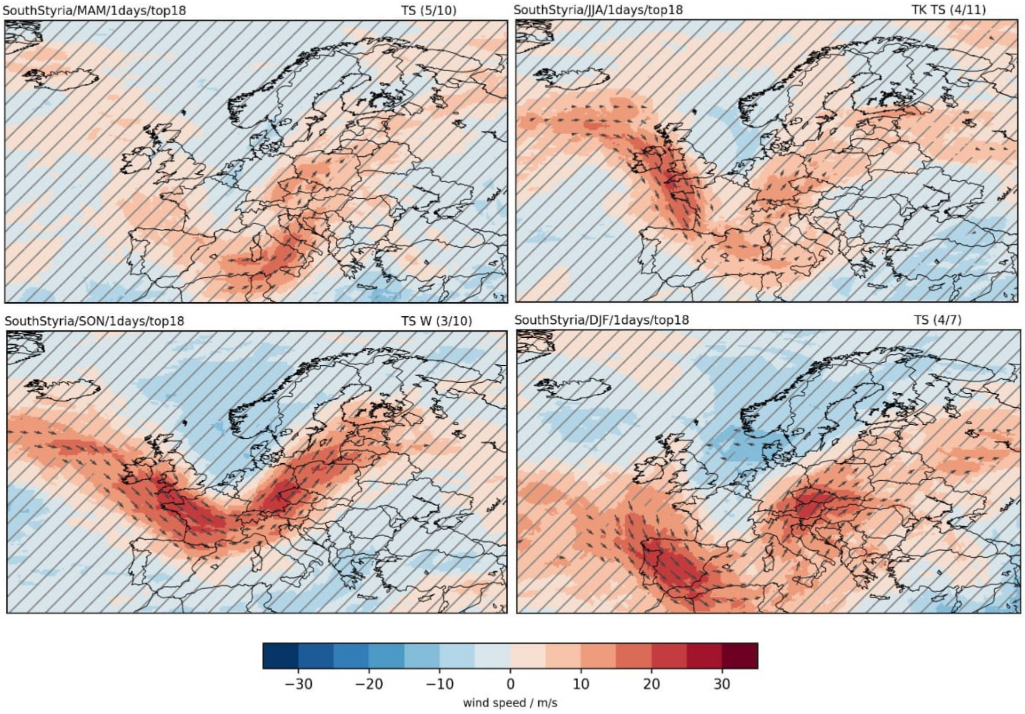

Figure 4.16: Anomaly of the 300 hPa wind field composites of the 18 strongest daily extreme precipitation events in the South Styrian region for each season separately. Insignificant anomalies are hatched. The letters in the upper right corner denote the most frequent Lauscher Class(es) on the days of the events, together with the fraction of absolute occurrences over the number of events where the Lauscher Class(es) were available.

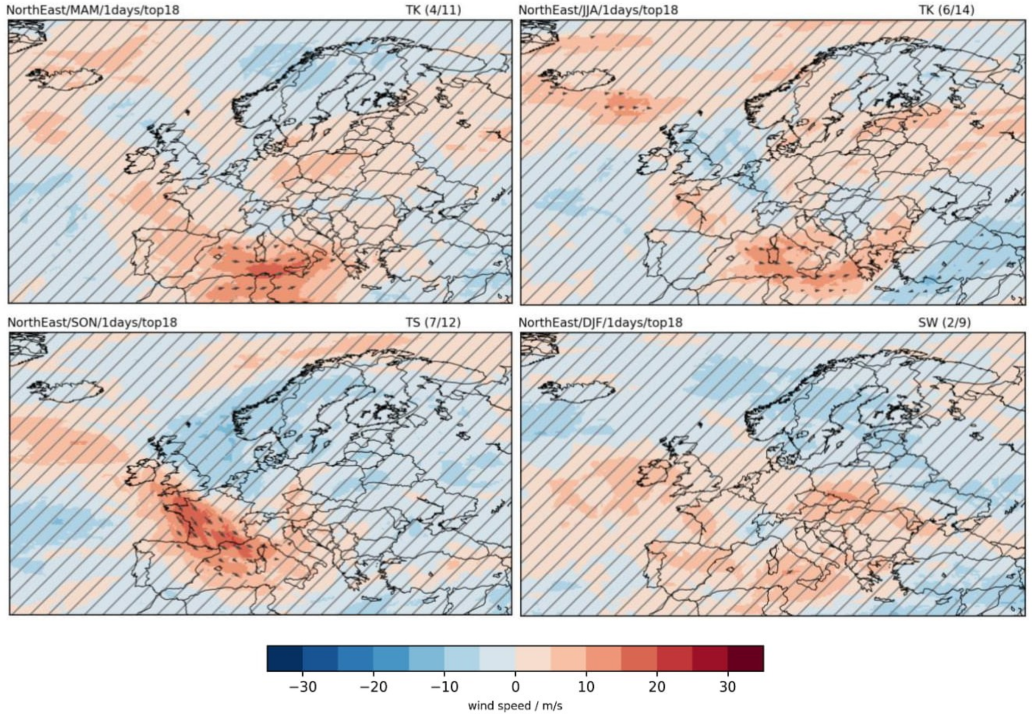

Figure 4.17: Same as in Fig. 4.16 for the North East region

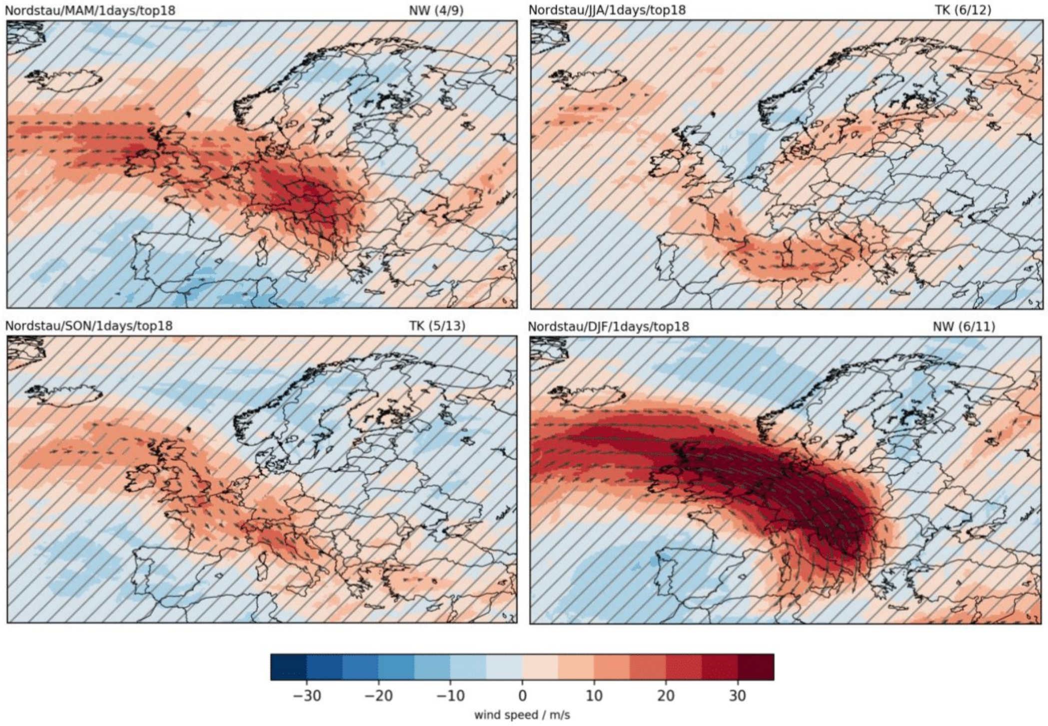

Figure 4.18: Same as in Fig. 4.16 for the Northern Stau region

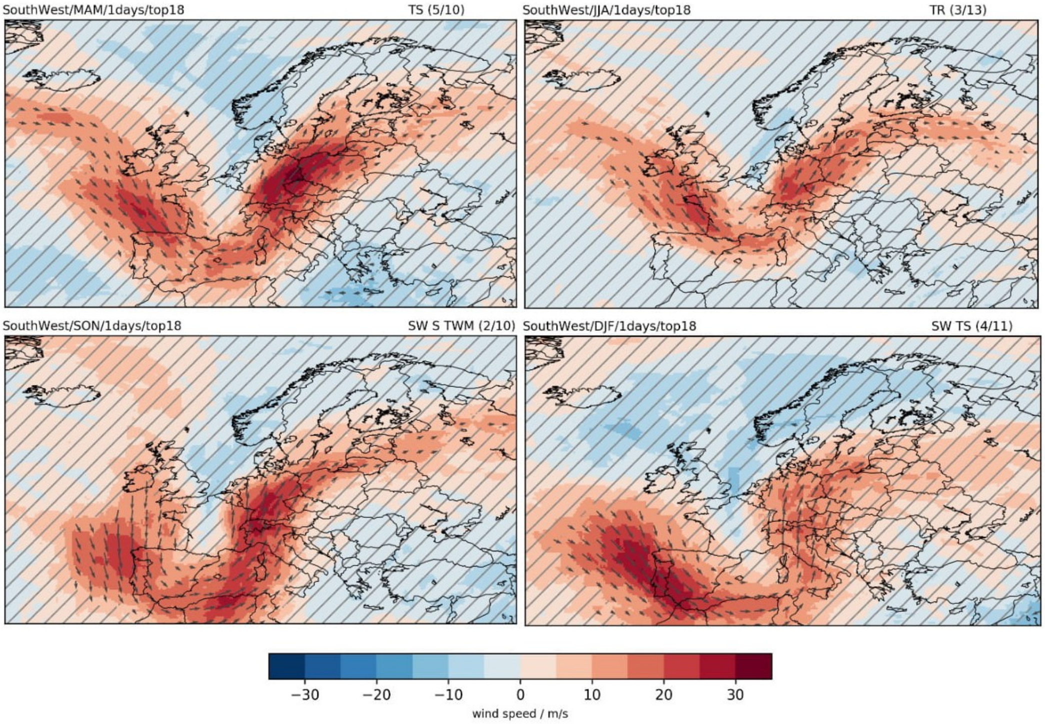

Figure 4.19: Same as in Fig. 4.16 for the South West region

In addition, the moisture transport and the wind speed at the 850 hPa level is plotted in Fig. 4.20 to 4.23 to analyse the large-scale atmospheric conditions in the lower troposphere during these extreme events.

For extremes in the South Styria region (Fig. 4.20) there are positive moisture anomalies visible in the vicinity of the extreme event region, with highest anomalies usually centered around the Adriatic Sea. Strong anomalies are seen in autumn, where significant values are found from the Mediterranean over all Eastern Europe up to the Baltic States and Russia. In spring and winter the pattern is similar with slightly weaker anomalies. In summer, the significant anomalies are restricted to a smaller area, covering southern Austria, Slovenia, northern Croatia, Hungary and stretching north into Poland. The moisture transport anomalies clearly suggest that the Mediterranean and especially the Adriatic Sea is the main moisture source for extreme events in the South Styria region in every season. There is also a counter movement visible over Western Europe, where moisture is transported south towards the Mediterranean. The overall pattern therefore resembles the pattern of jet stream anomalies(Fig. 4.16), suggesting a coupling of the upper and lower tropospheric conditions. These results are also supported by the most frequent Lauscher Class on the days of the extreme events, which appears to be TS in all seasons.

In the North East region (Fig. 4.21), there are more differences between the individual seasons. Strongest moisture anomalies are found for autumn over Eastern and around the Adriatic Sea. This is very similar to the result for autumn for the South Styria region. The moisture though is transported from the Adriatic Sea in a wider arc over Eastern Europe into the North East region. Similar conditions are seen in spring, but with less significance for both the humidity and the moisture transport. In winter the moisture anomalies are also weak, but still significant over a large area covering a band stretching from the Benelux over Germany and Eastern Europe towards the Black Sea and Turkey. Over the Adriatic Sea, there are no significant values. The moisture transport anomalies are very weak, but hinting at the North Sea on the one hand and the Mediterranean and the Black Sea on the other hand as possible sources for the extreme events. An explanation for the weak anomalies in this season could be that the extremes happened on days with different synoptic situations. This is suggested by the most frequent Lauscher Class, which only appeared on 2 out of nine event days, meaning that on all other 7 event days for which the Lauscher Classes are available, a different class has to be occured. In the resulting composite plot, this could result in a mutual obliteration of the anomalies. In autumn, where the highest humidity anomalies are found, 7 out of 12 days had the same Lauscher Classes. In summer, significant moisture anomalies are only found in the direct vicinity of the North East region. Interestingly, there is even a wider region of negative anomalies visible over northern Spain and the Bay of Biscay. The moisture transport on the other hand are the strongest of all seasons, forming almost a full, anticlockwise rotating circle. The Black Sea could be a main moisture source for extreme events in the summer season.

Looking at the Northern Stau region (Fig. 4.22), the conditions in summer seem to be very similar to the North East region, but with a larger area with significantly enhanced humidity, stretching from the Black Sea in a curve over the Ukraine, Belarus and Poland towards Austria. This does even more point to the Black Sea as the main moisture source for extremes in the Northern Stau region in summer. In the other seasons, the conditions are completely different. In winter and with weaker anomalies also in spring and autumn, there is moisture transported in a northwest-southeast direction from the Atlantic and the North Sea directly towards the Northern Stau region. This is accompanied with enhanced humidity centered over northern France, the Benelux and western Germany. In autumn, there are also positive anomalies over the Aegean Sea and the Black Sea. The discrepancy between the summer and the spring and winter season is also indicated by the different most frequent Lauscher Class, which appears to be NW for spring and winter and TK for summer. However, for autumn TK is also the most frequent class, despite the large differences in the pattern of the composite plots, limiting the information of the most frequent Lauscher Class.

For extreme events in the South West region (Fig. 4.23), the strong south to north

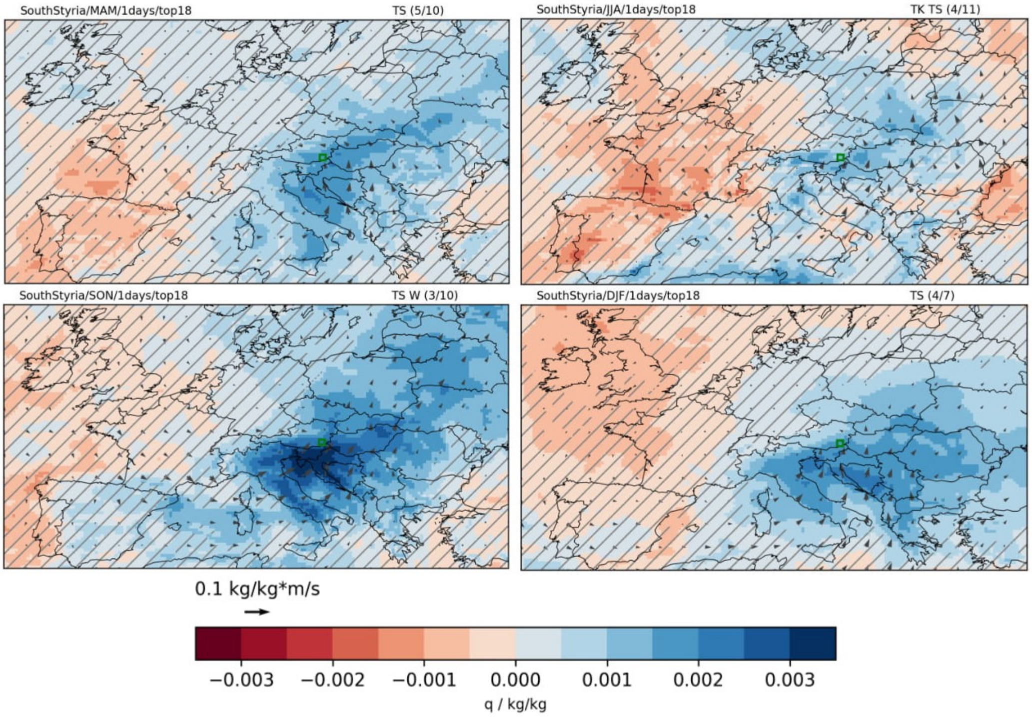

Figure 4.20: Anomaly of the 850 hPa moisture transport (arrows) and specific humidity (colors) composites of the 18 strongest daily extreme precipitation events in the South Styria region for each season separately. Insignificant anomalies are hatched. A green rectangle indicates the extreme event region. The letters in the upper right corner denote the most frequent Lauscher Class(es) on the days of the events, together with the fraction of absolute occurrences over the number of events where the Lauscher Class(es) were available.

moisture transport into the target region clearly indicates that the Mediterranean is the main moisture source in all seasons. Strongest humidity anomalies are found in winter, where significant anomalies are also covering a wider area than in the other seasons. Especially in summer and autumn, a counter movement is seen with moisture transport from north to south over the UK and France in summer and the Bay of Biscay and Iberia in autumn, where there are also negative humidity anomalies.

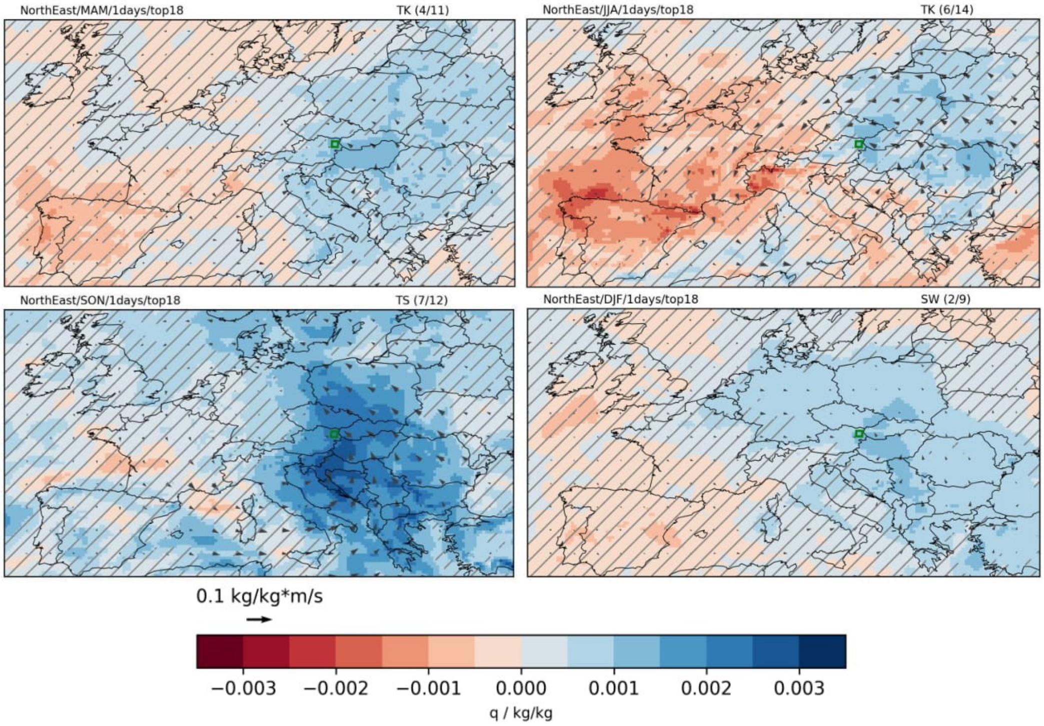

Figure 4.21: Same as in Fig. 4.20 for the North East region

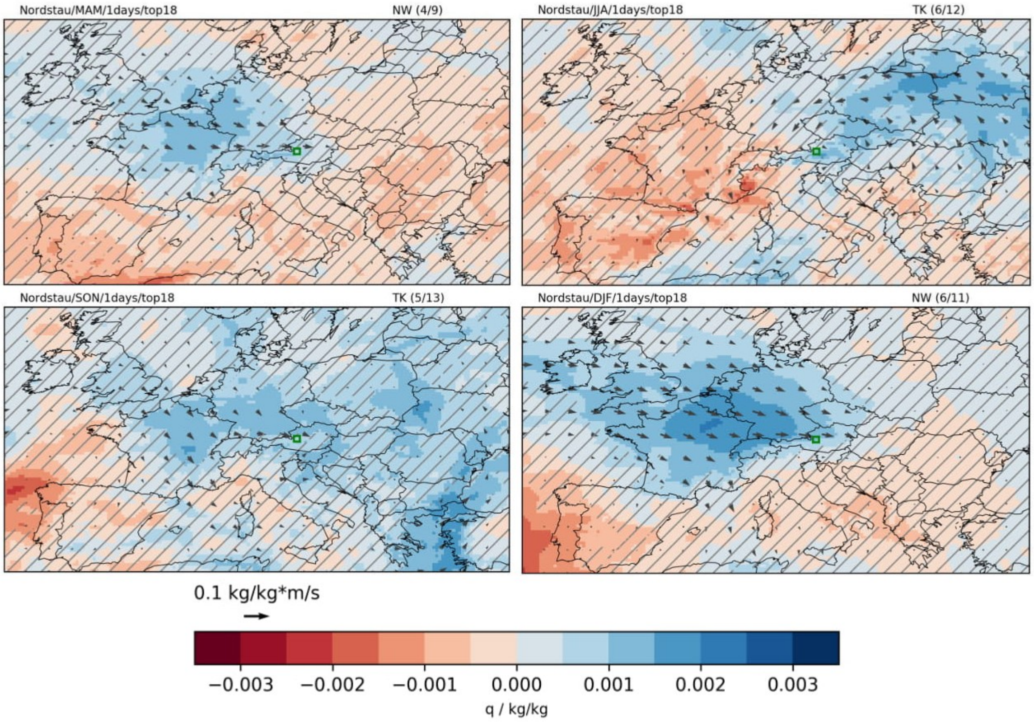

Figure 4.22: Same as in Fig. 4.20 for the Northern Stau region

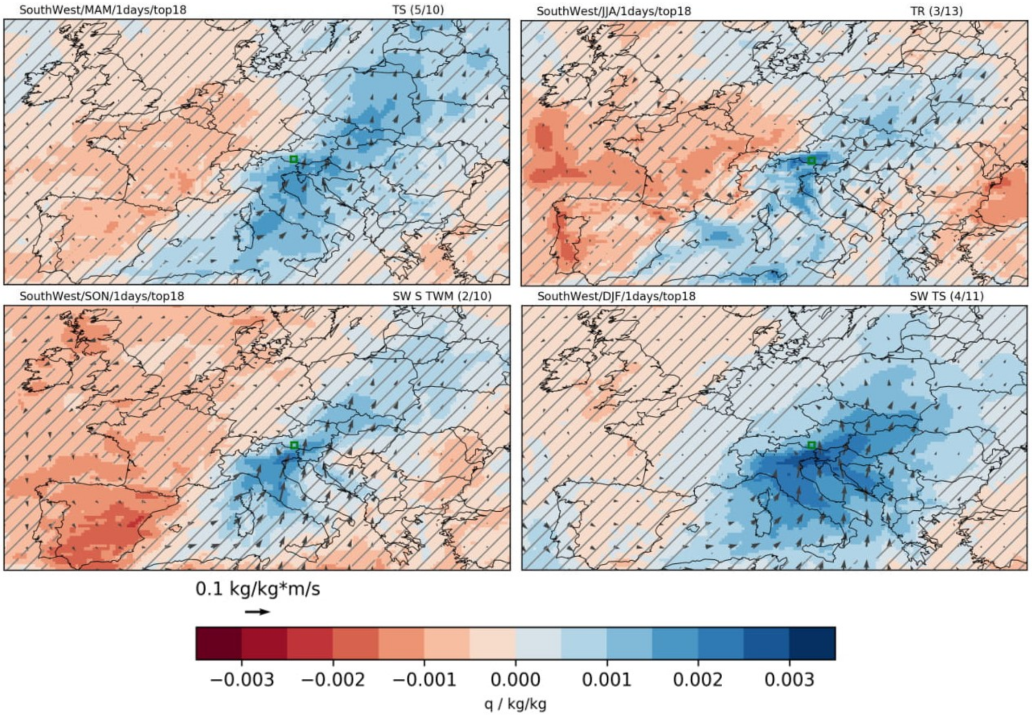

Figure 4.23: Same as in Fig. 4.20 for the South West region

Interpreting the results of a composite analysis has to be done with caution to not make misleading conclusions. A downside of the composite analysis is that it will average over events with potentially very different synoptic to large-scale features. For instance, it remains unclear if the results for the North East region (Fig. 4.17) with only small areas of significant values are actually indicating a very weak jet stream during extreme precipitation events in this region or if very different results for the individual events canceled out each other due to the averaging. At least for the winter season, the moisture transport and the different synoptic conditions indicated by the Lauscher Classes do support the latter explanation. On the other hand, also the very strong pattern found for the jet stream for the Northern Stau region in winter could be either a very pronounced jet stream or very similar patterns for the individual events, amplifying the anomalies when they are averaged. Furthermore, one should keep in mind that the jet stream is usually much stronger in winter than in summer (Koch et al., 2006).

The results do however still reveal strong differences of the conditions between extreme events in the individual regions. The South Styria and South West show very similar results both for the jet stream and the moisture transport and availability. A meandering of the jet stream over western Europe is visible in all seasons, indicating cyclogenesis over the Mediterranean. This is also supported by the most frequent Lauscher Classes, which is TS in all seasons for the South Styria region and TS and TR for the South West region except for autumn, which seems to have a larger variability in terms of synoptic conditions. The Mediterranean is clearly the main moisture source for extreme precipitation in these regions. The contrary results for the Northern Stau region, although located less than 1° to the north of the South West region, can be explained by the main alpine ridge, separating these regions and protecting the Northern Stau region from Mediterranean influences. Thus, extreme events in this regions are mainly accompanied by north to northwesterly flow coming from the North Sea, both visible in the jet stream and moisture transport and supported by the Lauscher Classes NW and TK. The differing patterns in summer do support other conditions in this season. As pointed out above the weak results for the North East regions could indicate that extreme events in this region could be caused by a larger variety of synoptic and large-scale conditions than in the other regions.

4.3 Weather types

4.3.1 Estimation of the GPD

To investigate the risk of extreme precipitation in Austria under the condition of different weather types, the GPD will be estimated for precipitation data on days where a specific Lauscher Class occurred. From the estimated parameters, return levels will be calculated.

Before estimating the GPD parameters, Tab. 4.1 shows the frequency of the individual Lauscher Classes in the time period 1997-2018 for which they are available. Some classes do have very low frequencies, especially **Vb** and **N**. Since the threshold u of the GPD will be chosen as the 90th percentile, this would give only 3-4 samples for **Vb** and 6 samples for **N**to fit the GPD on, which is obviously not enough. For the class **S**, the estimation also failed due to a too small sample size. Therefore, the Lauscher Classes **Vb**, **N** and **S** have to be excluded from the extreme distribution analysis. The classes **TwM** and **TSW**, which would have also a too low frequency when considered separately, where combined for this analysis, as Lauscher did not distinguish between those classes and therefore the differences should be negligible. One should keep in mind that for the Lauscher Classes **TR**, **TB** and **TwM+TSW** the errors of the estimated parameters are still large, especially for the shape parameter and the return levels. A more accurate and suitable selection of the threshold u could have been possibly achieved by using nonparametric methods, graphical methods or Goodness-of-Fit tests (Langousis et al., 2016) for the precipitation data of each class individually, potentially reducing the parameter errors. Since the aim of this analysis is to get qualitative rather then quantitative results, the benefit of a

Table 4.1: Frequency of the Lauscher Classes in the time period 1997-2018

Lauscher Class	TK	TR	Vb	TS	TB	TwM+TSW
Frequency	679	170	36	461	281	188
Lauscher Class	N	NW	W	SW	S	G
Frequency	58	954	756	566	123	860

more accurate threshold selection was not expected to be substantial and thus was not conducted. Moreover, by using the same percentile for each Lauscher Class as the threshold, it allows to compare them.

Fig. 4.32 to 4.28 shows the pattern of the threshold u, i.e. the 90th quantile of the precipitation data, the estimated parameters σ_0 and ξ_0 of the GPD (according to (3.5)) and the estimated return level (according to (3.7)), defined as the level which is expected to be exceeded once every 150 days the corresponding Lauscher Class occurred. Note that in terms of return periods this gives different results for each class. For instance, the return levels found for the class TR will be exceeded only once in 20 years, as this class only occurred at 170 days in the 22-year period. The return levels found for the class TK however, are expected to be exceeded once every 5 years.

The results for the Lauscher Classes **TR**, **TK** and **TS** do show large similarities. The threshold, i.e. the 90th quantile is highest at the southern border of Austria, centered where the borders of Italy, Slovenia and Austria met, which is the typical "Southern Stau" region. For **TR** and **TK**, there are also higher thresholds in the northern Alpine foothills. Overall, the thresholds are enhanced over all parts of Austria, compared to the other classes. The scale parameter is highest at the southern border of Austria, meaning that in this region the extreme values exhibit large variations. Hence, also the return levels are highest in this region for all three classes. **TR** has individual high scale parameter values also in other regions, which could be due to bad estimation because of the small sample size as mentioned above. The same holds for the shape parameter. For **TK** and **TS** the shape parameter is close to zero, indicating a light-bounded GPD.

Thresholds associated with the Lauscher Class **TB** over Austria are also high at the tri-border region Austria-Slovenia-Italy, but much more restricted to this region than the other low pressure related classes. In Tyrol and eastern Austria, the threshold is generally low. High thresholds are found outside Austria over the whole western alpine region. The scale parameter does correlate with the threshold and thus also the return levels, giving high values where high thresholds and scale parameters are found.

The Lauscher Class **TwM&TSW** gives high thresholds along the western Mediterranean coast, the western alpine region south of the main alpine ridge and again in the Southern Stau regions in Austria and Slovenia. In Austria outside of Carinthia, the thresholds decrease rapidly. The scale parameter is highest at the southern border of Austria and along the western Mediterranean coast, resulting in the high return levels in those regions. The shape parameter seems to be very low in parts of southern Austria, indicating a bounded GPD which should again be taken with caution due to the small sample size.

The Lauscher Classes associated with the large-scale flow over Austria (**NW**, **W**, **SW**) do show significantly lower values, which is not surprising since they are not associated with low pressure systems. NW has enhanced thresholds along the northern alpine slopes as expected from northwesterly flow. The scale parameter is also enhanced there and additionally also in Slovenia and the Slovenian-Austrian border. The shape parameter has weak positive values in most regions. The return values are as high in Slovenia and the most southern parts of Austria as north of the Alps due to the scale parameter.

W has higher thresholds over middle Austria than in the west or east, as well as over Switzerland along the northern slopes of the Alps and in some parts of western Germany. The scale parameter is again highest in the south of Austria and in Slovenia, resulting in the high return levels there.

SW is very similar to **TB**, indicating that TB is accompanied by a southwesterly flow over the Alps. The values are also comparably in magnitude.

The Lauscher Class **G**, which contains all days which could not be categorized in either of the other classes does not show any enhanced values for either of the parameters and is therefore not important for extreme precipitation over Austria. Probably most of these days are associated with weak high pressure or weak pressure gradient conditions over Austria.

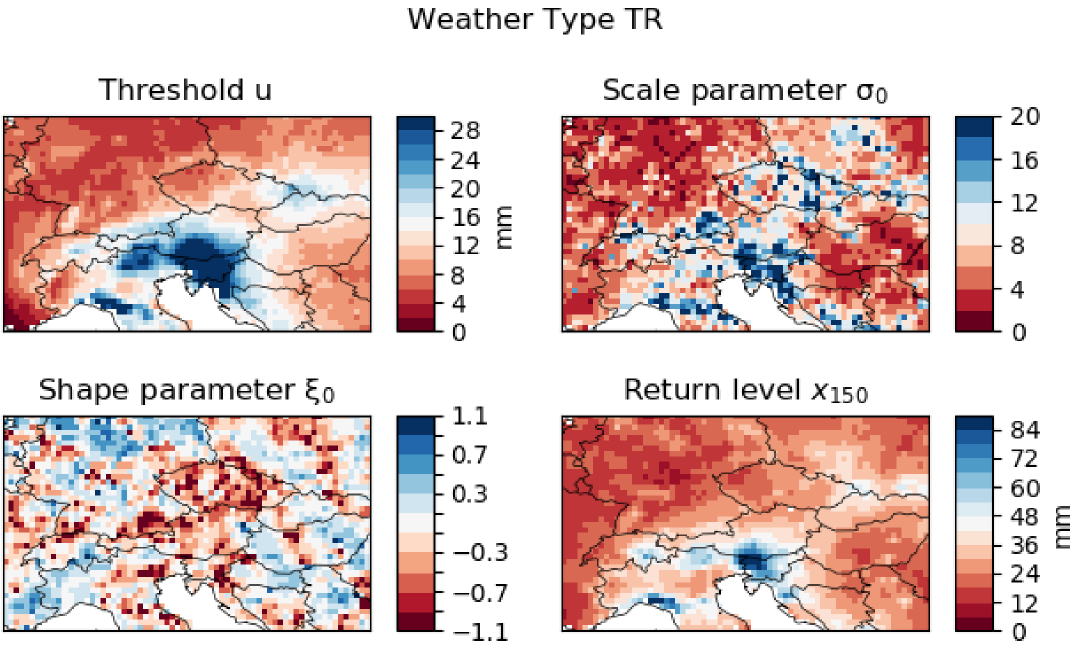

Figure 4.24: Threshold u and estimated parameters σ_0 and ξ_0 of the GPD and the estimated return level for the Lauscher Class **TR**. u is defined as the 90th quantile of the precipitation data on days where the Lauscher Class occurred. The return levels are defined such that they are expected to e exceeded once every 150 occurrences of the Lauscher Class.

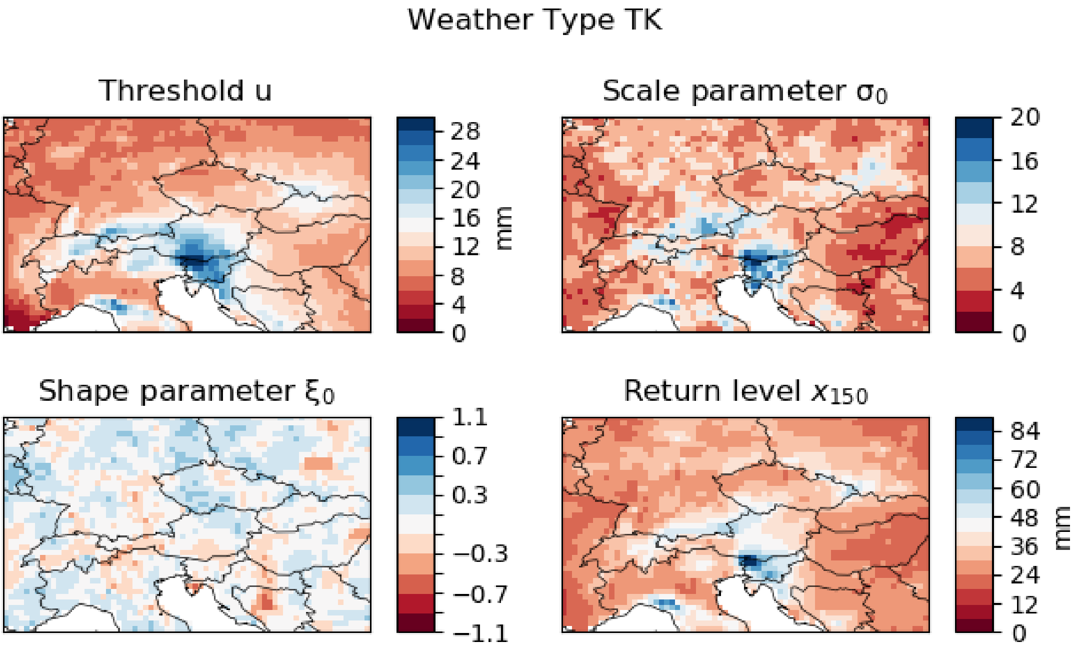

Figure 4.25: As Fig. 4.32 for the Lauscher Class **TK**.

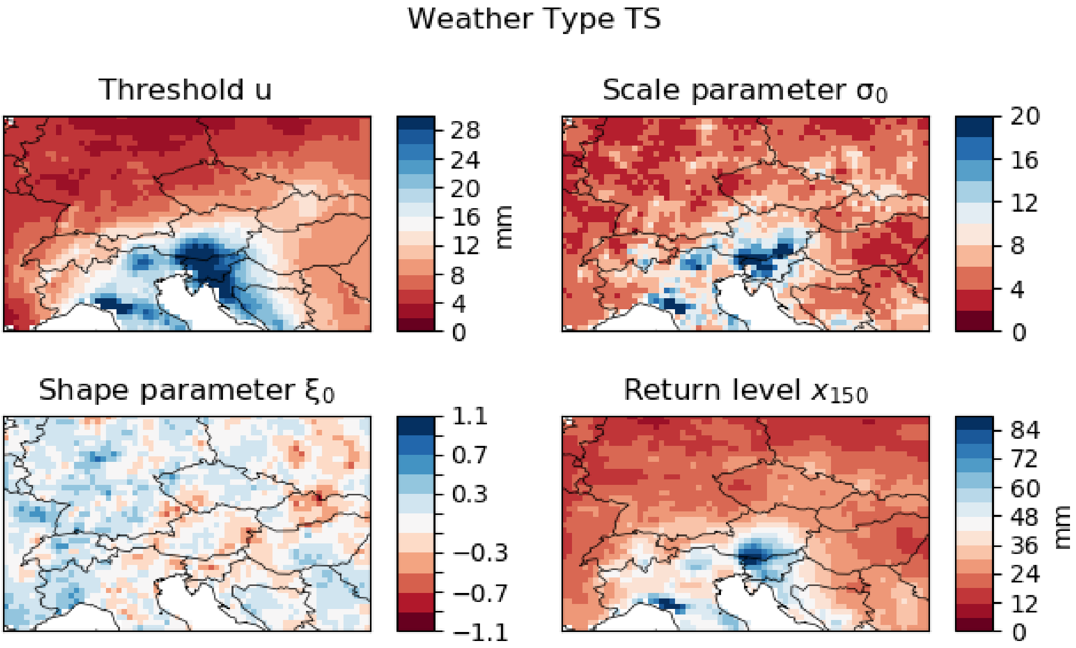

Figure 4.26: As Fig. 4.32 for the Lauscher Class **TS**.

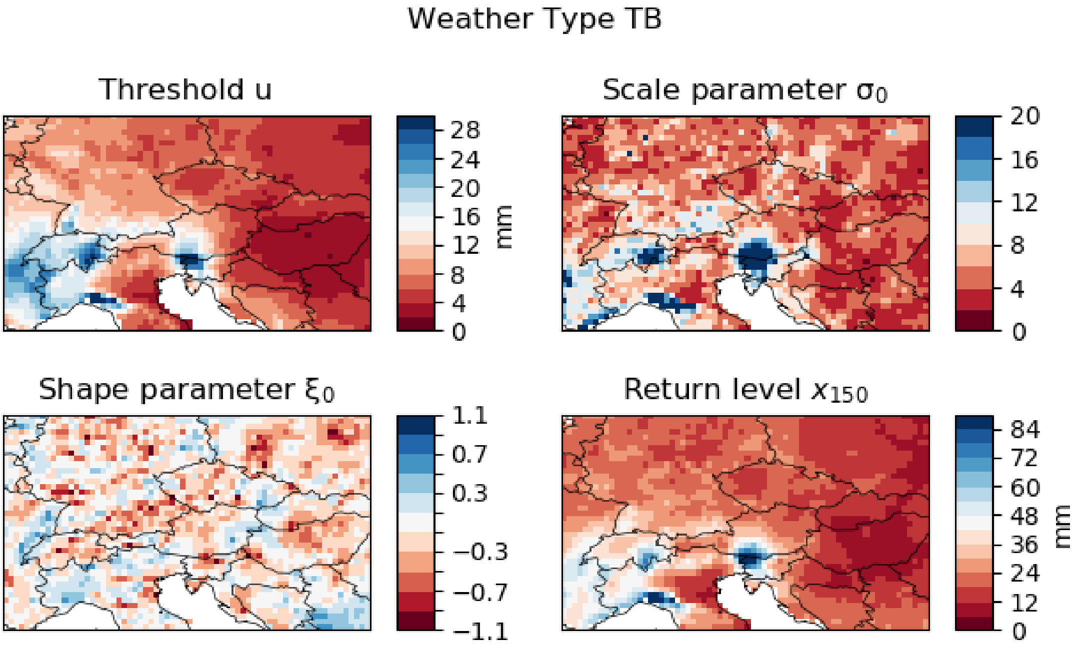

Figure 4.27: As Fig. 4.32 for the Lauscher Class TB.

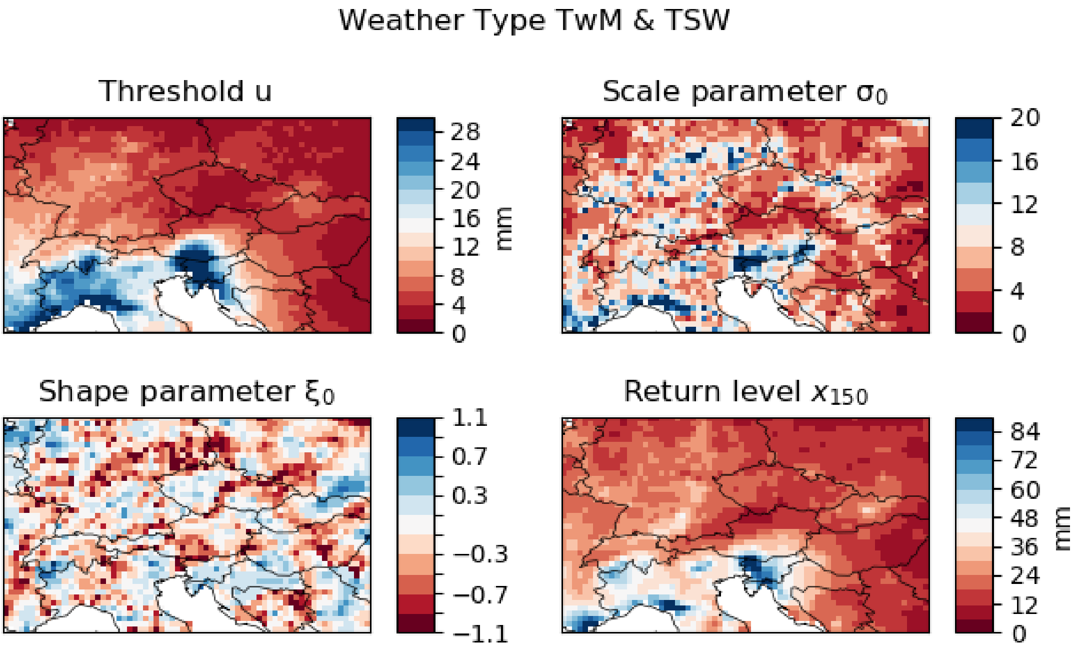

Figure 4.28: As Fig. 4.32 for the Lauscher Class **TwM&TSW**.

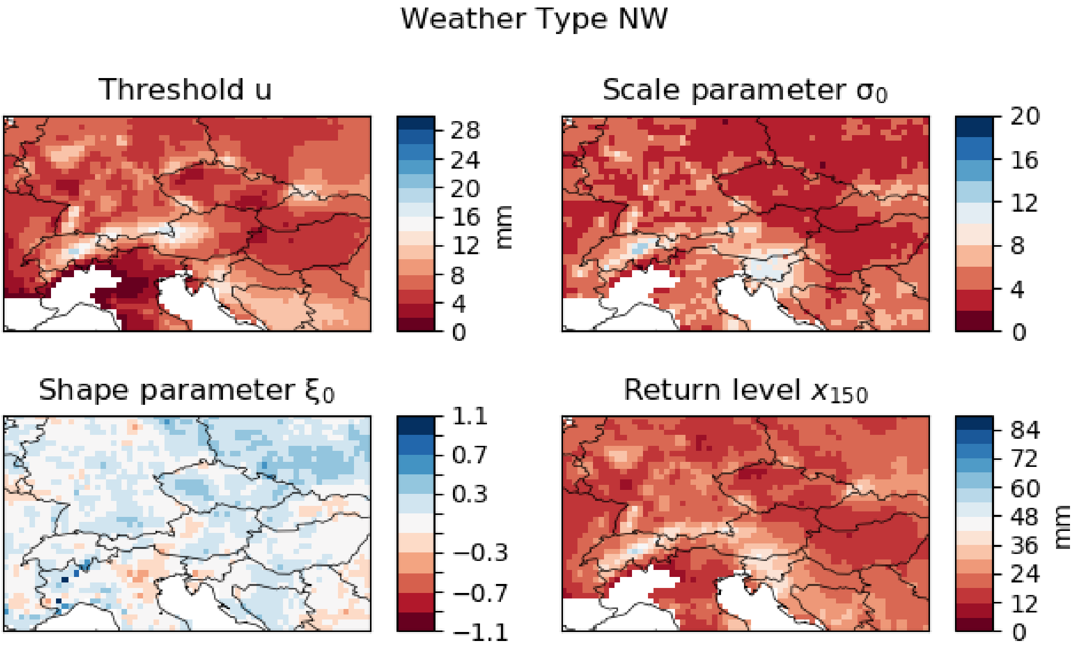

Figure 4.29: As Fig. 4.32 for the Lauscher Class **NW**.

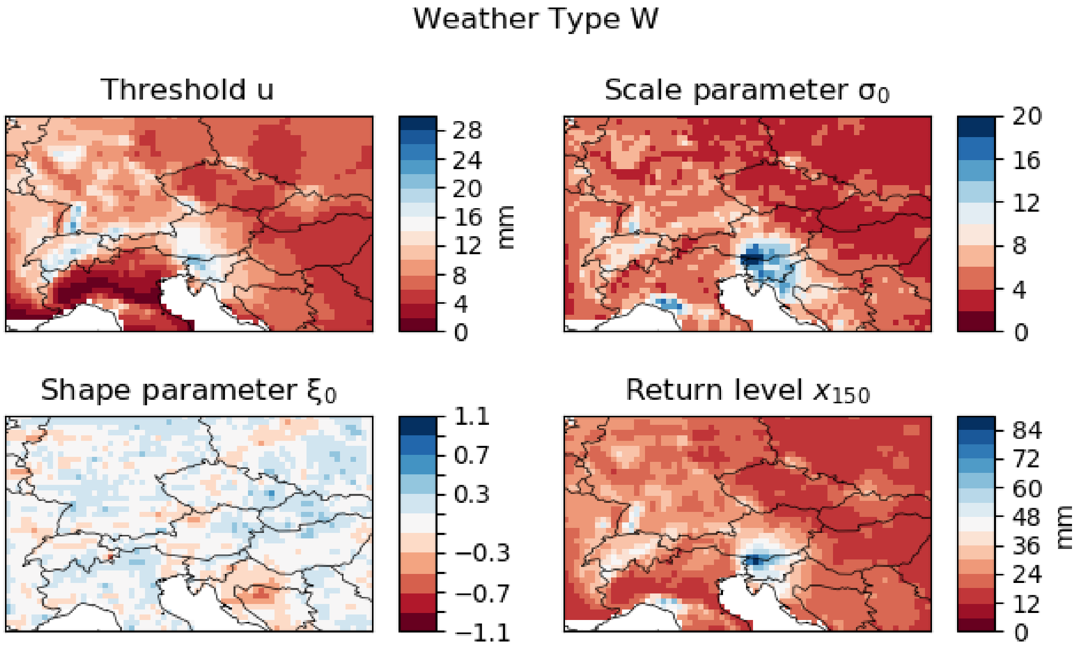

Figure 4.30: As Fig. 4.32 for the Lauscher Class **W**.

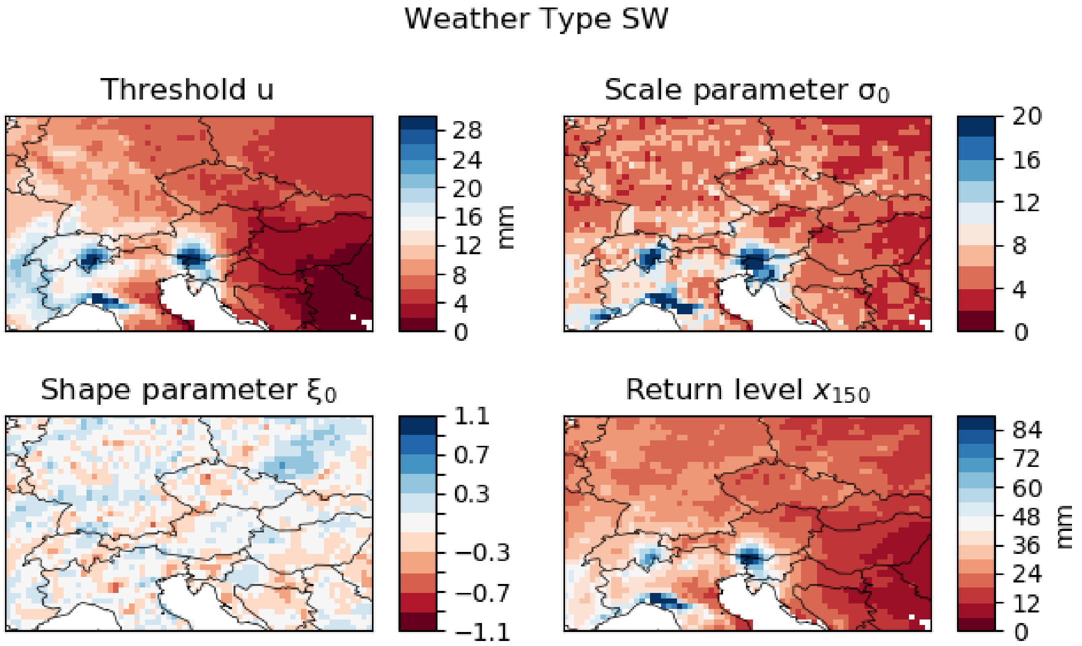

Figure 4.31: As Fig. 4.32 for the Lauscher Class **SW**.

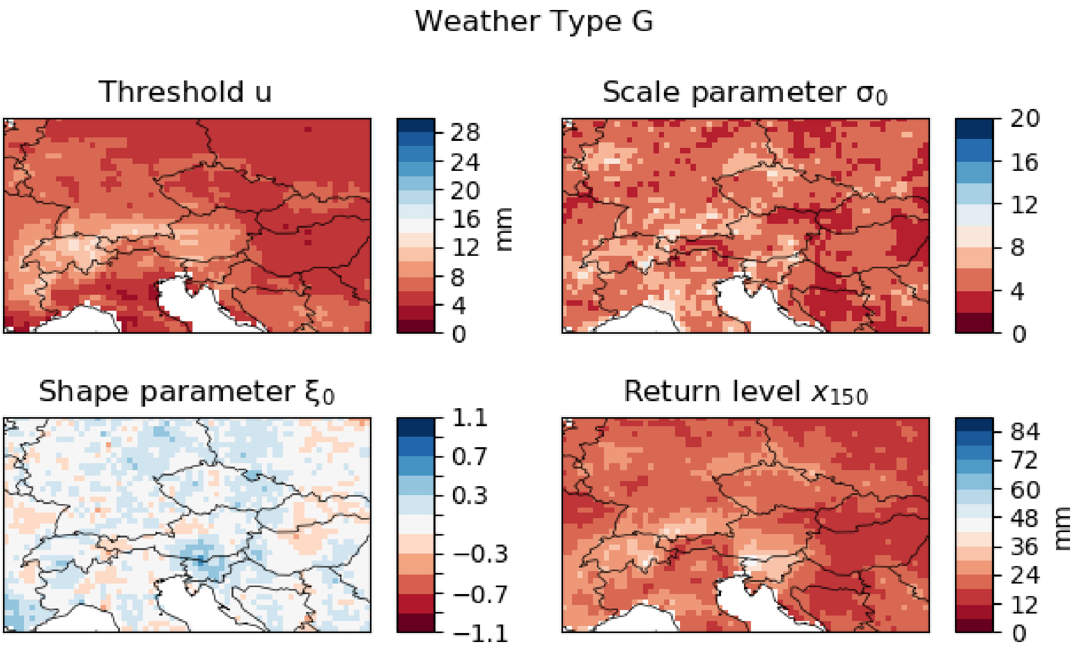

Figure 4.32: As Fig. 4.32 for the Lauscher Class **G**.

4.3.2 Fitting of the seasonal cycle

In order to reveal differences between the individual seasons, the seasonal cycle of precipitation conditional on the Lauscher Classes is calculated. Therefore, the precipitation intensity on each day where the weather type occurred is plotted against the day in the year when it occurred. This is done at four points of the precipitation grid, one within each region defined in Sec. 3.2. The seasonal cycle is approximated by a sine wave (Maraun et al., 2009), i.e.

$$y = a + b * sin\left(\frac{2\pi t}{365.25}\right) + c * sin\left(\frac{2\pi t}{365.25}\right), \tag{4.2}$$

where t is the number of the day in the year and a,b and c the coefficients which have to be estimated. The precipitation intensities are assumed to follow a Gamma distribution (Martinez-Villalobos and Neelin, 2019). The seasonal cycle is fitted for the 50th, 80th and 95th percentile in order to see differences when going to more extreme values. The 95% confidence intervals are obtained by error propagation.

Fig. 4.33 to 4.44 show the results for each Lauscher Class, including **N**, **S** and **Vb**. For **Vb** only the 50th percentile is plotted, as the fitting of the higher percentiles failed probably due to the small sample size. Note the different scales for the y-axis.

The Lauscher Class **TR** does not show significant variations in the seasonal cycle in North West and South Styria. In South West the 95th percentile has a maximum July and a minimum in February. In North East, the 50th percentile has a maximum in July and August, which is slightly shifted to September for the 80th percentile. The minima are in February and March, respectively. The 95th percentile has no significant variations.

For the class **TK**, maxima are seen in the high summer months and minima in winter for nearly all regions and percentiles, especially for the 95th percentile in North West. In North East, the maximum and minimum occurs 2 months earlier in the year.

The class **TS** has all the significant maxima (minima) of the 50th and 80th percentile in July/August (February). This is shifted 1 month towards earlier occurrences for the 95th percentile in South Styria and South West. In North East, the maximum and minimum occurs 1 month later. North West does not show a seasonal cycle in his 95th percentile.

Only the 95th percentiles have a pronounced cycle in North West and South West for the Lauscher Class **TB**. The maximum lies in August/September in South West and September/October in North West. The minima are in February and March. In North East, the maximum of the 95th percentile is in March, while it is in July for the lower percentiles. South Styria only has a significant maximum in high summer for the 50th percentile.

Results for **TwM+TSW** are not significant for the 95th percentile, but suggest maxima in spring. The lower percentiles also have their maxima in spring except for North East, where it is in July.

The Lauscher Class **N** has maxima in June/July and minima around the turn of the year. Only in the South West the maxima and occur later in the year, shifting from August (50th percentile) over September (80th percentile) to October (95th percentile). The results are however not significant for every region.

The maxima for **NW** are in August except for the 95th percentile in North West, where it is in July. The 95th percentile in South West does not exhibit a seasonal cycle.

The Lauscher Class **W** does not have any significant seasonal variations for either region or percentile.

For **SW**, the maxima lie in summer for the lower percentiles and are shifted towards autumn when going to the 95th percentile. However, those results are not significant at the 95% level.

For Lauscher Class **S** the maximum shifts in North West from May to March when going to higher percentiles. In South West the maxima of the lower percentiles lie in July, whereas the 95th percentile shows a minimum in summer, which is not very comprehensible when looking at the individual data points and probably again due to a too small sample size. The same applies for the 95th percentile in South Styria. In North East the maxima are found in July.

Lauscher Class **G** shows significant maxima of the seasonal cycles mostly In July. Only in South Styria and for the 95th percentile in North East this is slightly shifted towards August.

The results for **Vb** are not reliable due to the small sample size, but looking at the individual data points, the highest intensities are obtained in autumn and early winter for each region. Note however, that in South West there was only one event with precipitation exceeding 1 mm.

In summary, the most relevant Lauscher Classes for extreme precipitation are **TK**, **TR** and **TS**, which is not surprising as these classes correspond to low pressure over middle Europe and/or the Adriatic Sea. Additionally, when looking into the individual events, the Lauscher Classes **G** (Fig. 4.43) and **NW** (Fig. 4.39) show an enhanced risk of extreme precipitation particularly in summer, suggesting that these weather types provide a favorable environment for thunderstorms. The highest return levels are found around the tri-border region Austria-Slovenia-Italy, a typical Southern Stau region, which is known to have the highest rainfall extremes in Austria (Seibert et al., 2007). Interestingly, this was seen for all investigated Lauscher Classes, including **NW** and **W**, which were not expected to induce extreme rainfall at the southern side of the Alps. The high return levels for these classes were caused especially by high estimated scale parameters in this region.

The investigation of the seasonal cycles shows that most of the regions do either not exhibit significant variations or have their maxima in summer and minima in winter. Exceptions are found e.g. for the Lauscher Class **TB**. The seasonal cycle is often more pronounced in the 95th percentile due to the larger variations of precipitation intensities. The weather type **Vb**, which is known to cause severe weather over middle Europe and Austria, especially on the northern side of the Alps (Messmer et al., 2015; Hofstätter et al., 2018), could not have analysed properly due to the low frequency in the Lauscher series.

It should be noted that the fitted seasonal cycles often do not show as large variations as the data would suggest, e.g. for Lauscher Class **TK** (Fig. 4.34), **NW** (Fig. 4.39) and **G** (Fig. 4.43), where the most extreme events are by far stronger in summer than in other seasons. However, the fit of the 95th percentiles only exhibit very weak maxima in summer and has furthermore a surprisingly narrow confidence interval. The fit could be checked by comparing the seasonal cycle to a fit of a Gamma distribution to the data of individual months, but this was eventually beyond the scope of this thesis.

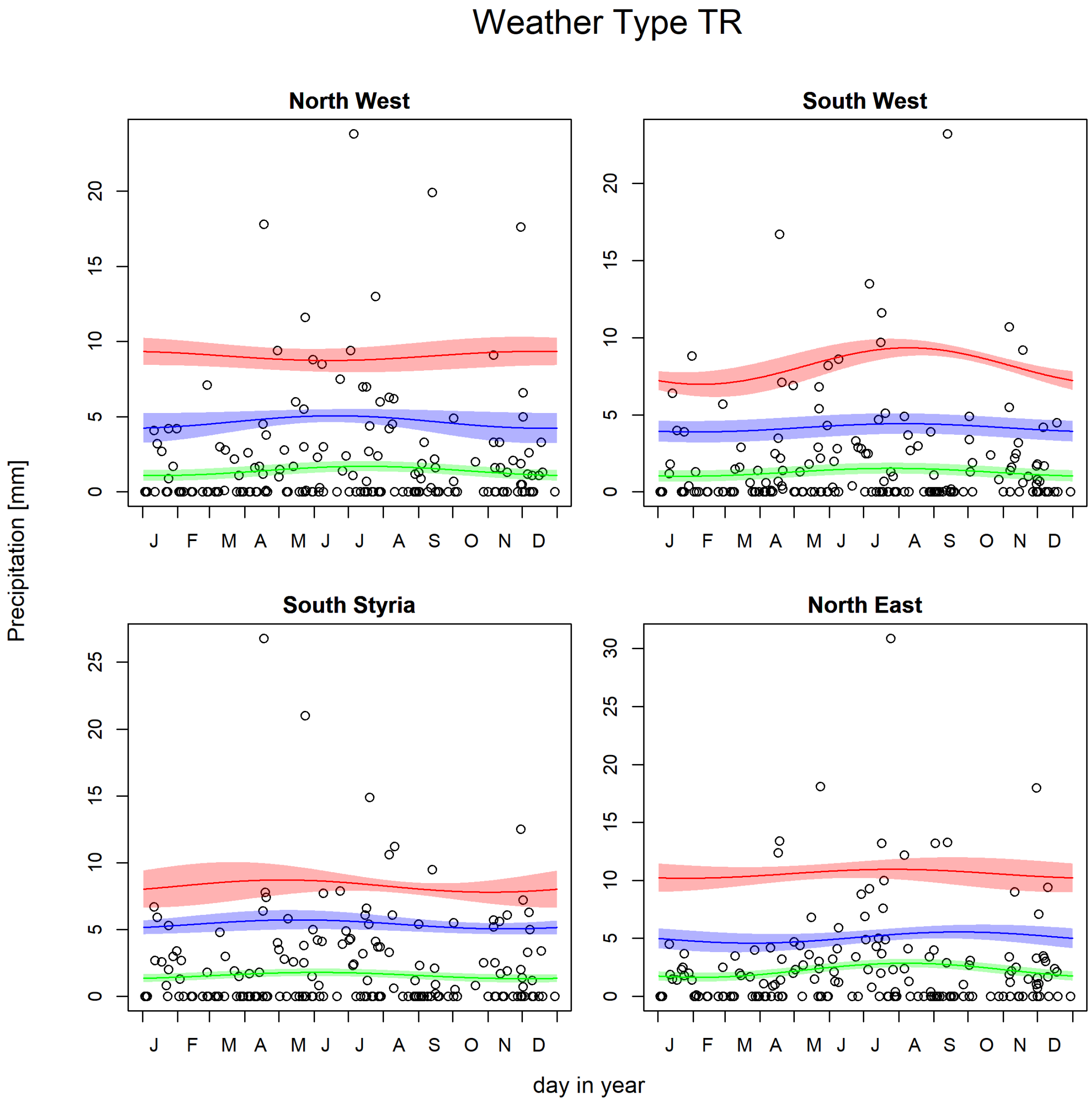

Figure 4.33: Fitted seasonal cycles for the 50th, 80th and 90th percentile at four individual grid points for precipitation data on days where Lauscher Class **TR** occurred.

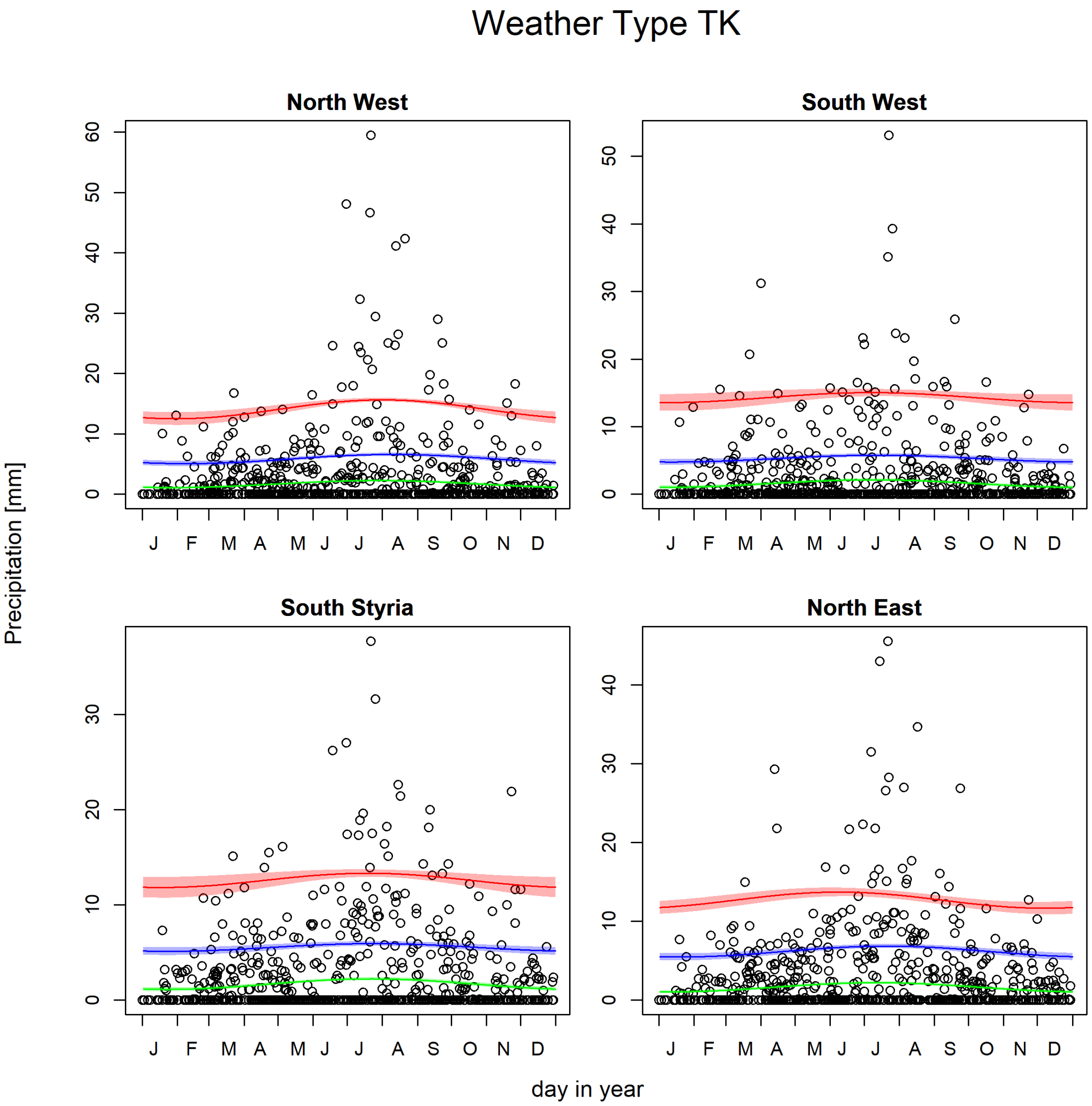

Figure 4.34: As Fig. 4.33 for Lauscher Class **TK**

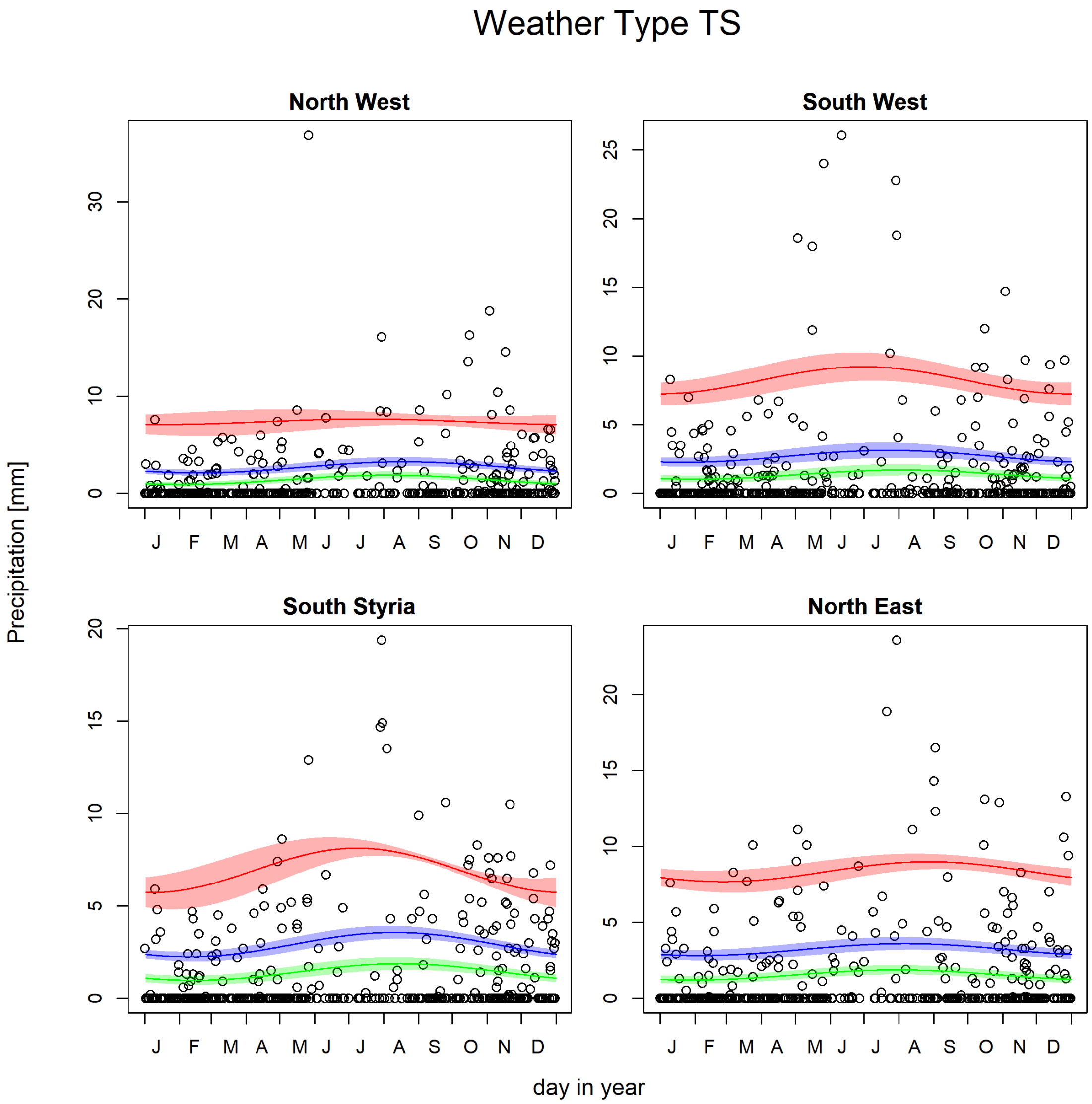

Figure 4.35: As Fig. 4.33 for Lauscher Class **TS**

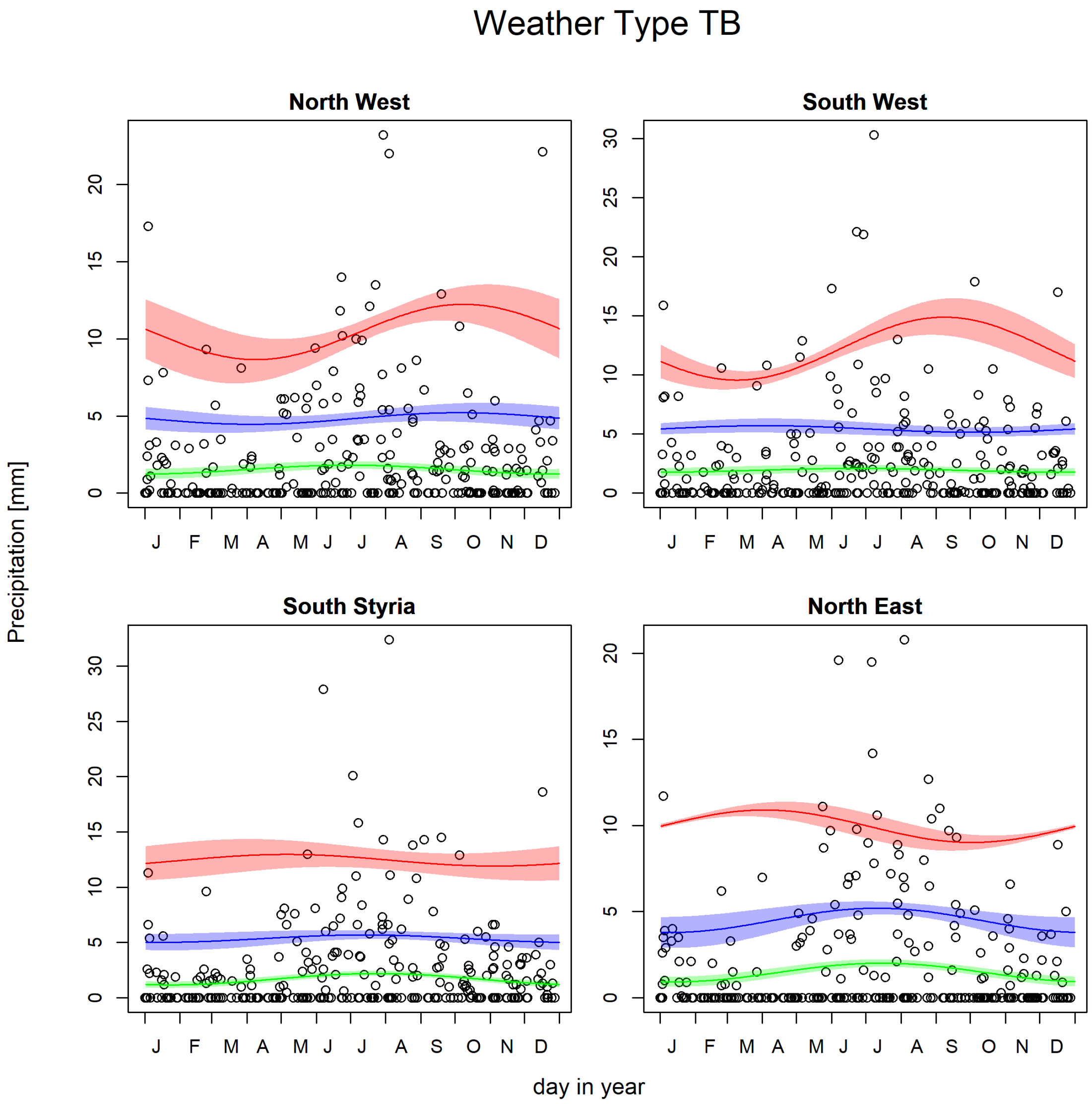

Figure 4.36: As Fig. 4.33 for Lauscher Class **TB**

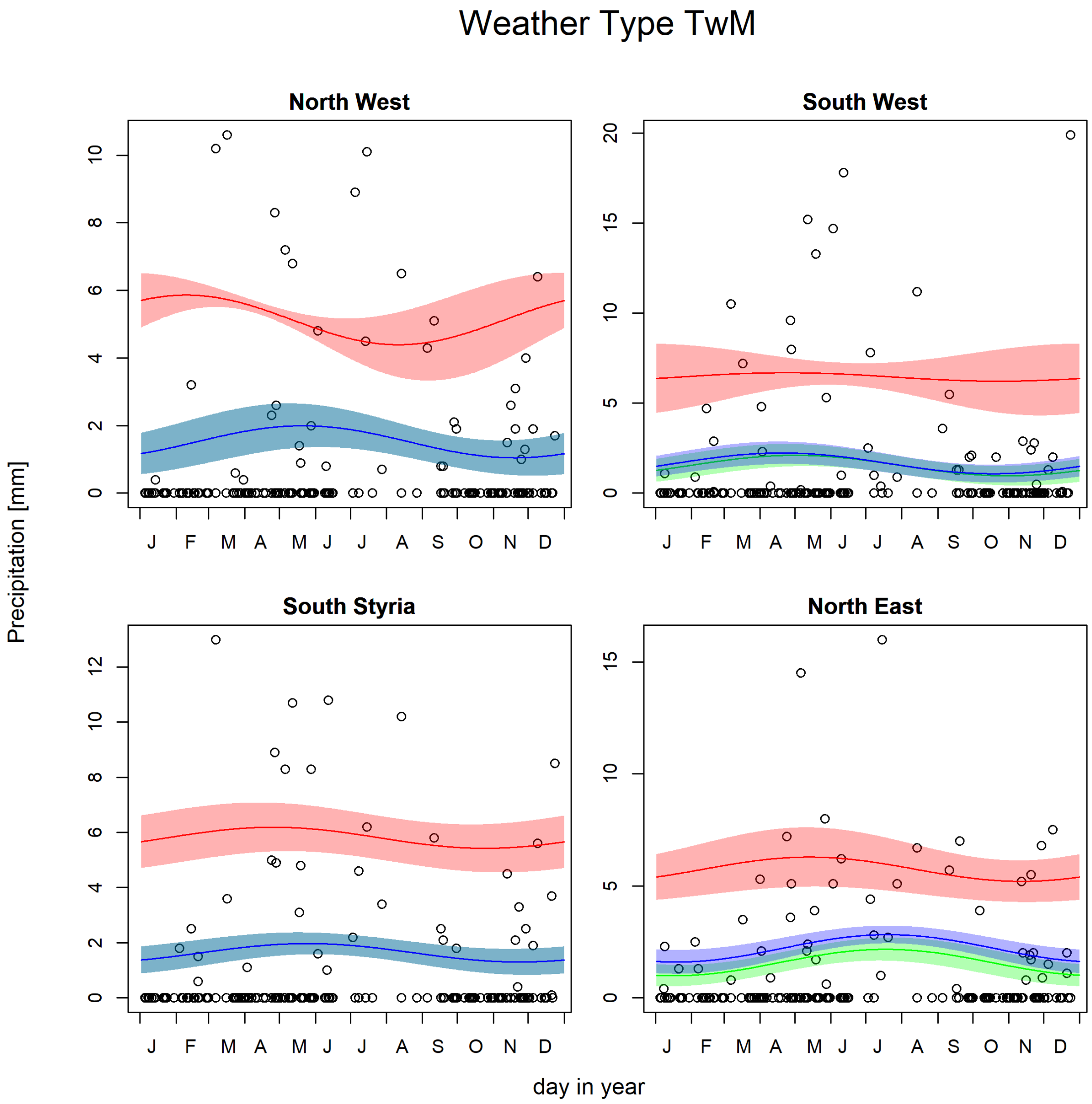

Figure 4.37: As Fig. 4.33 for Lauscher Class **TwM+TSW**

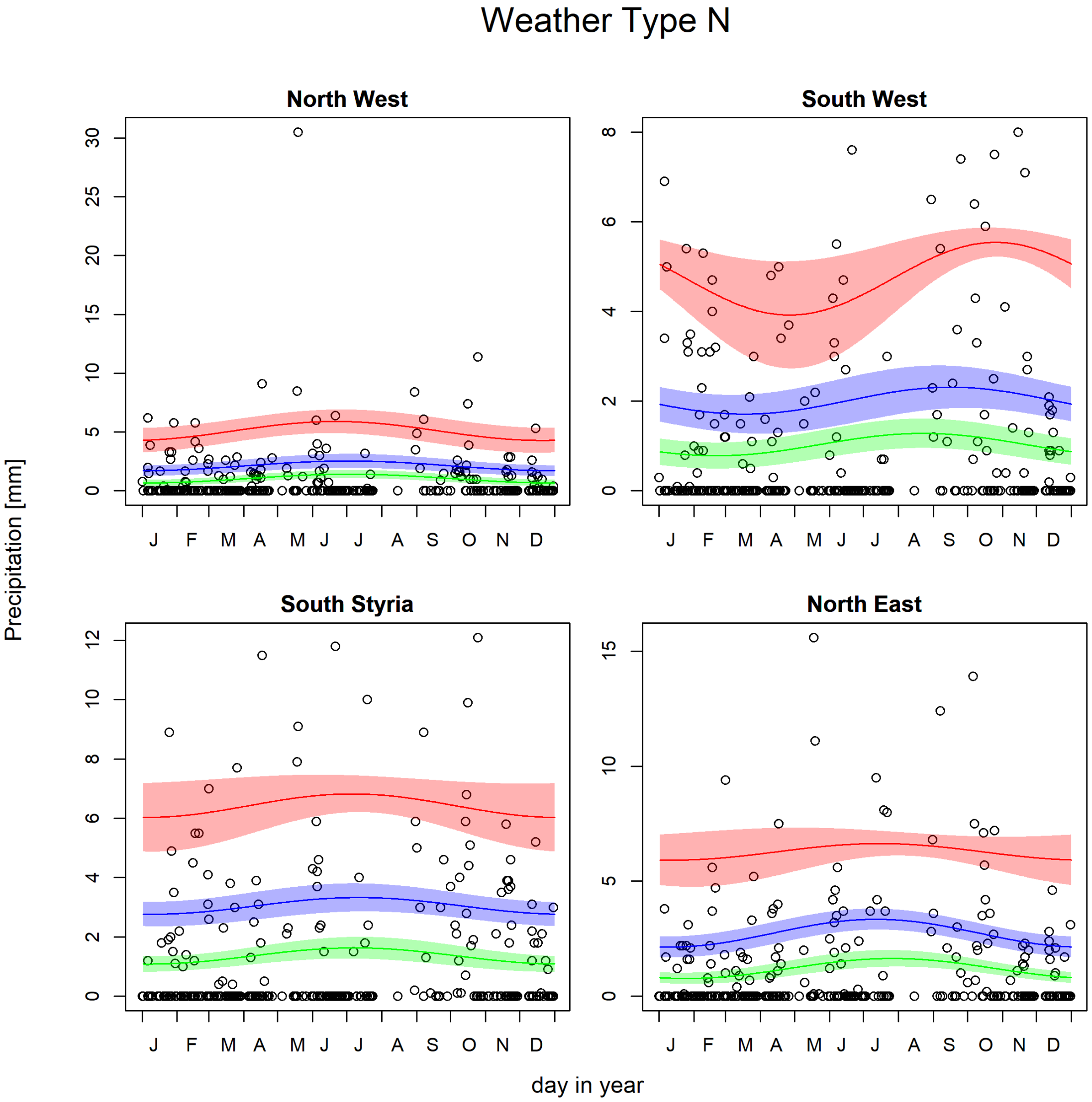

Figure 4.38: As Fig. 4.33 for Lauscher Class **N**

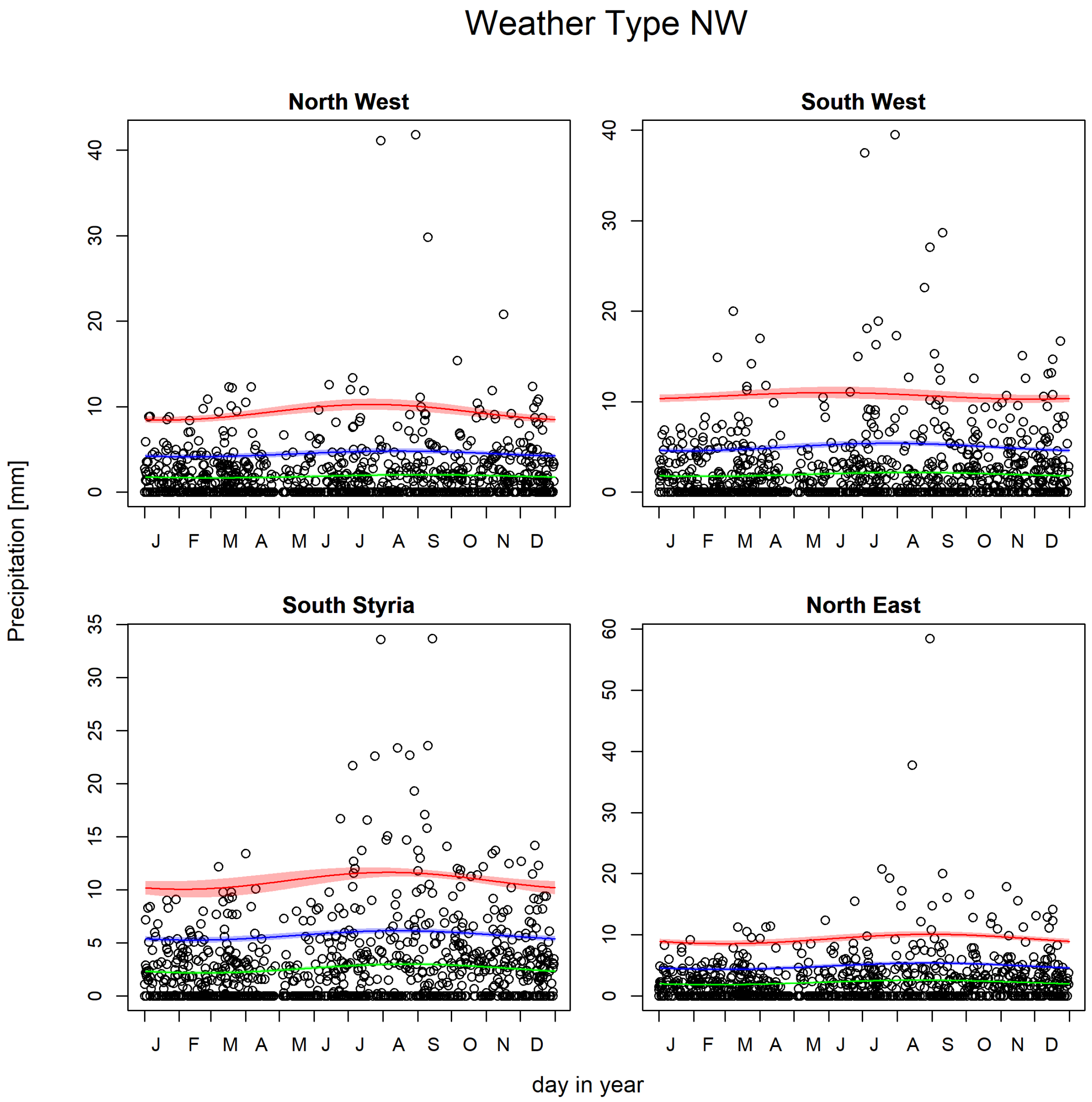

Figure 4.39: As Fig. 4.33 for Lauscher Class **NW**

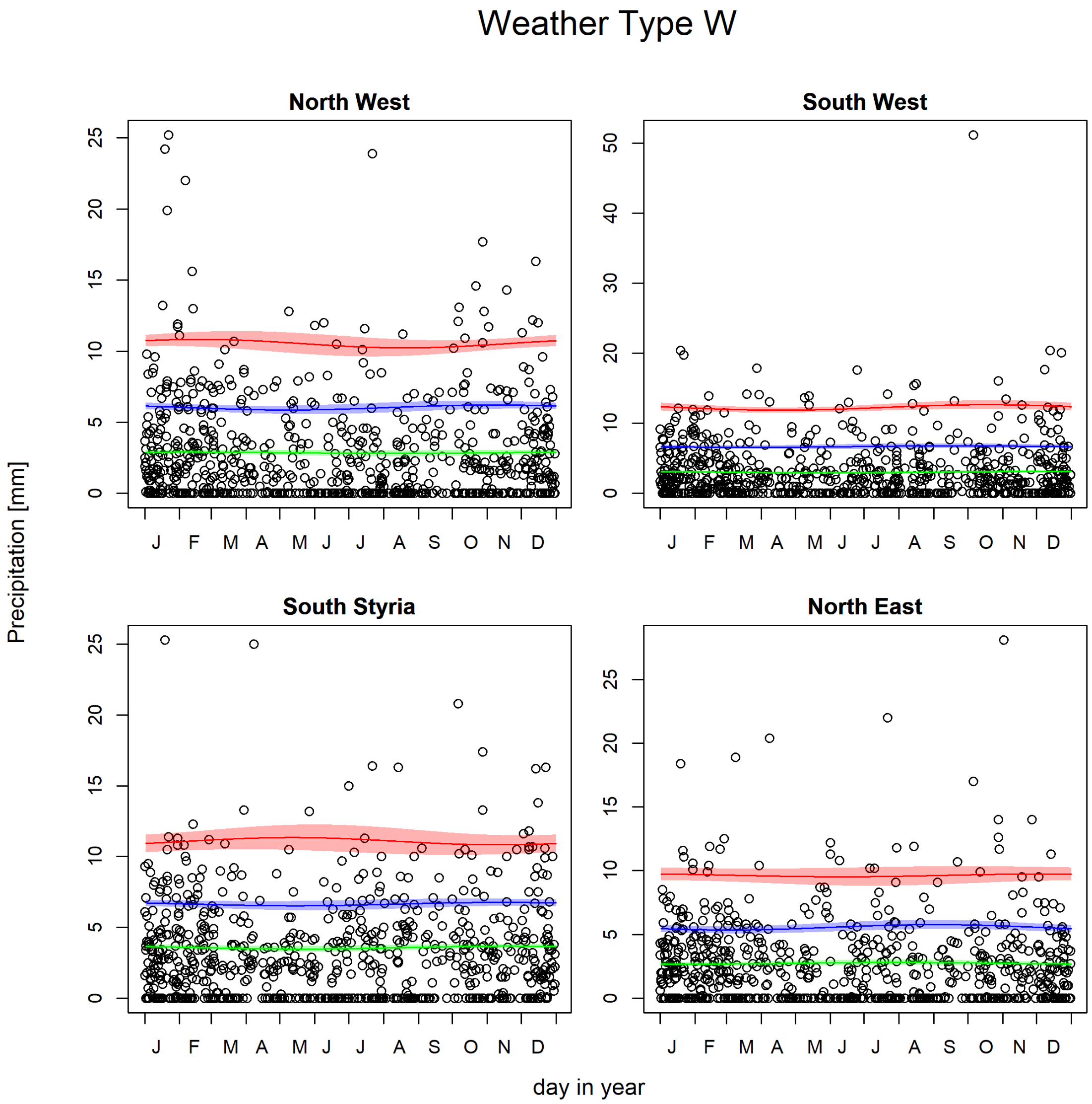

Figure 4.40: As Fig. 4.33for Lauscher Class **W**

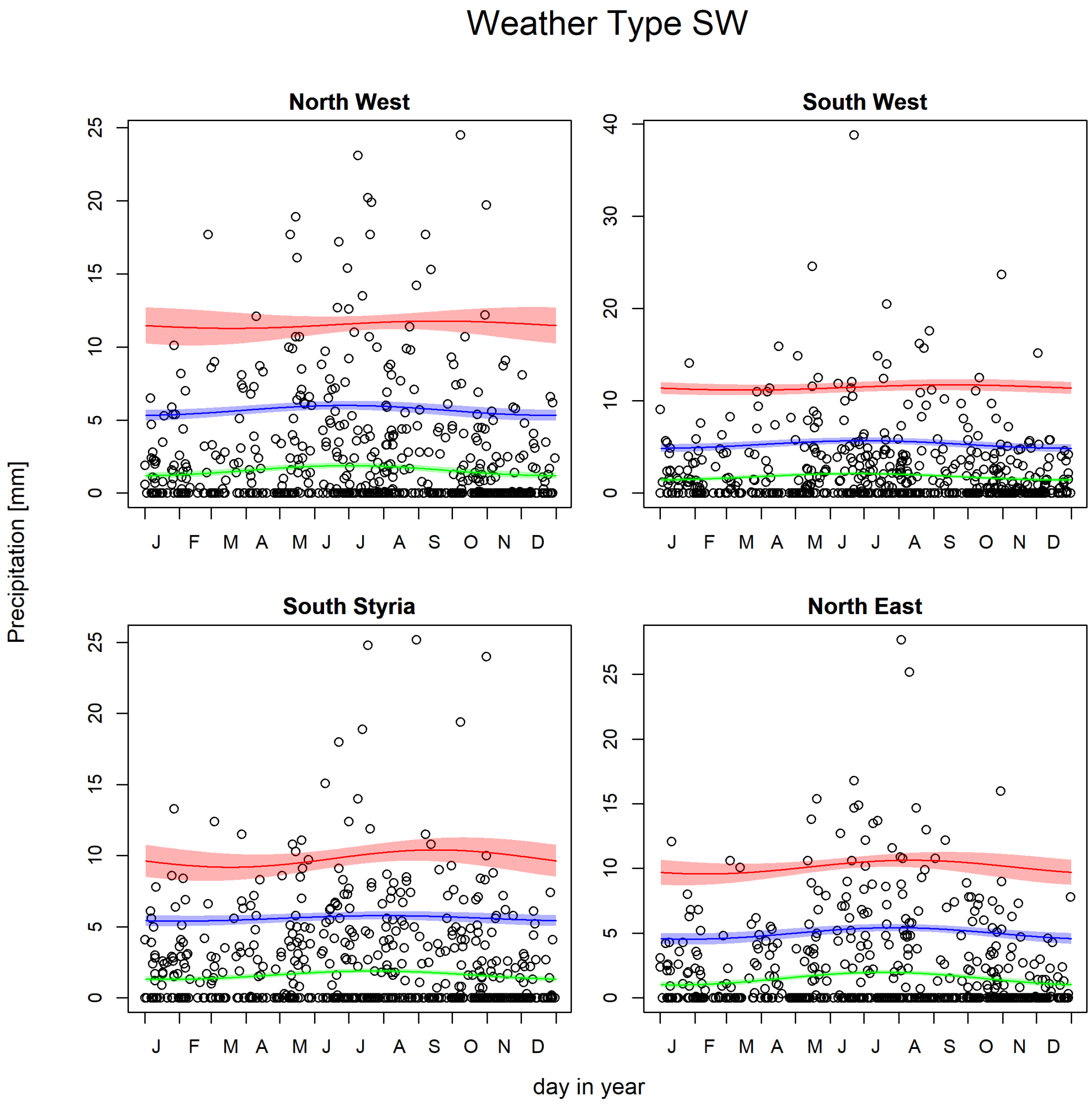

Figure 4.41: As Fig. 4.33 for Lauscher Class **SW**

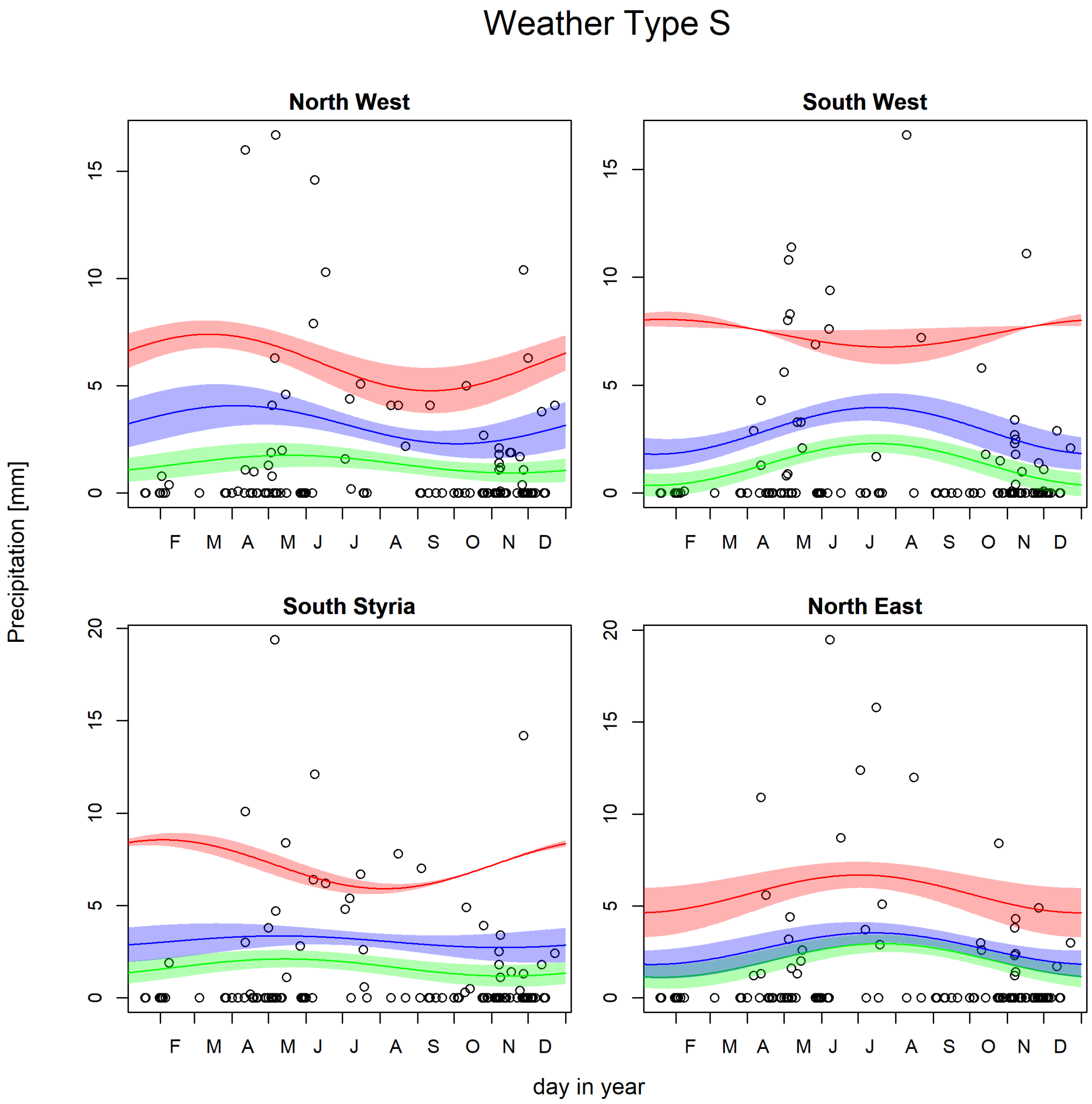

Figure 4.42: As Fig. 4.33 for Lauscher Class **S**

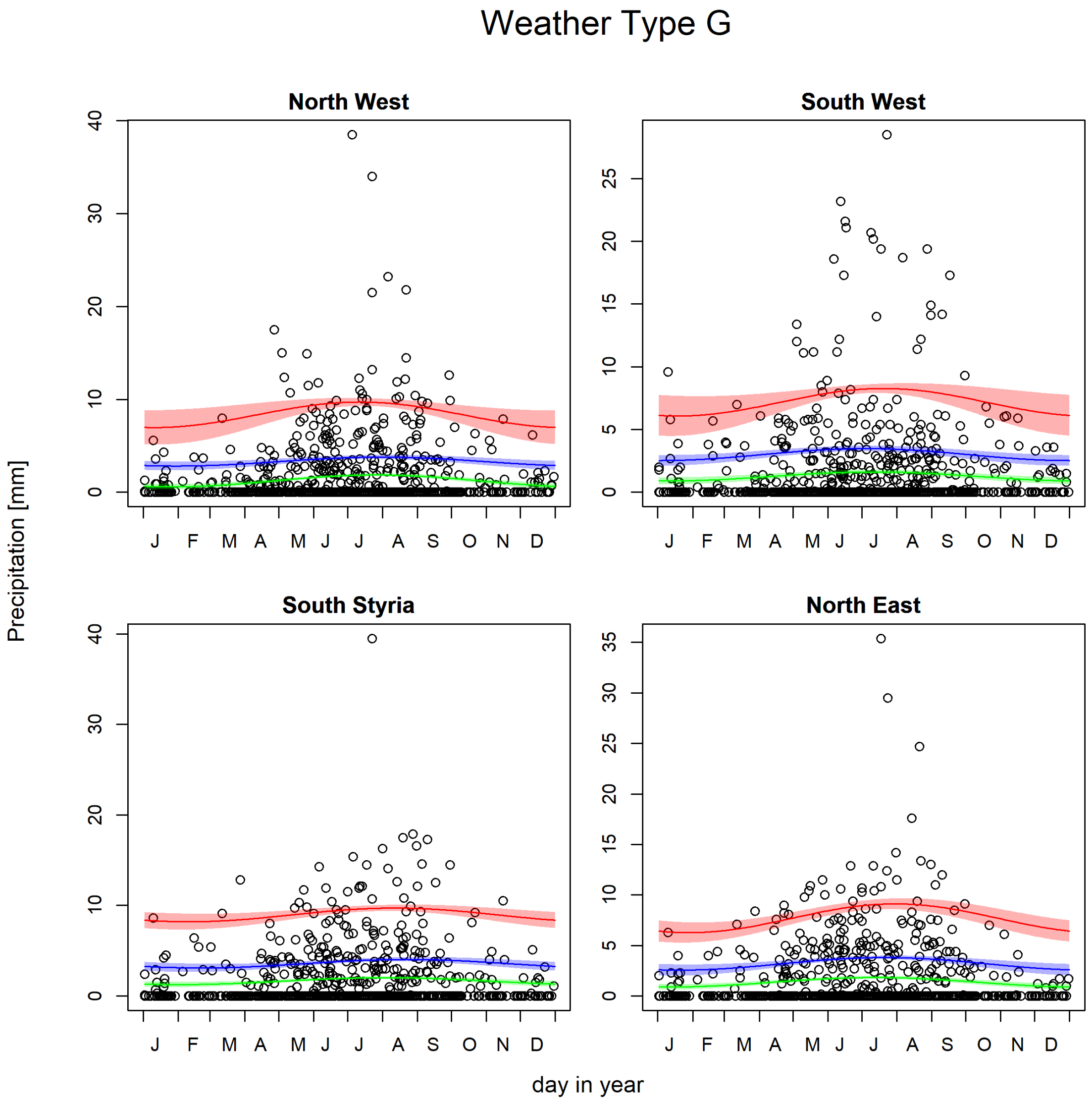

Figure 4.43: As Fig. 4.33 for Lauscher Class **G**

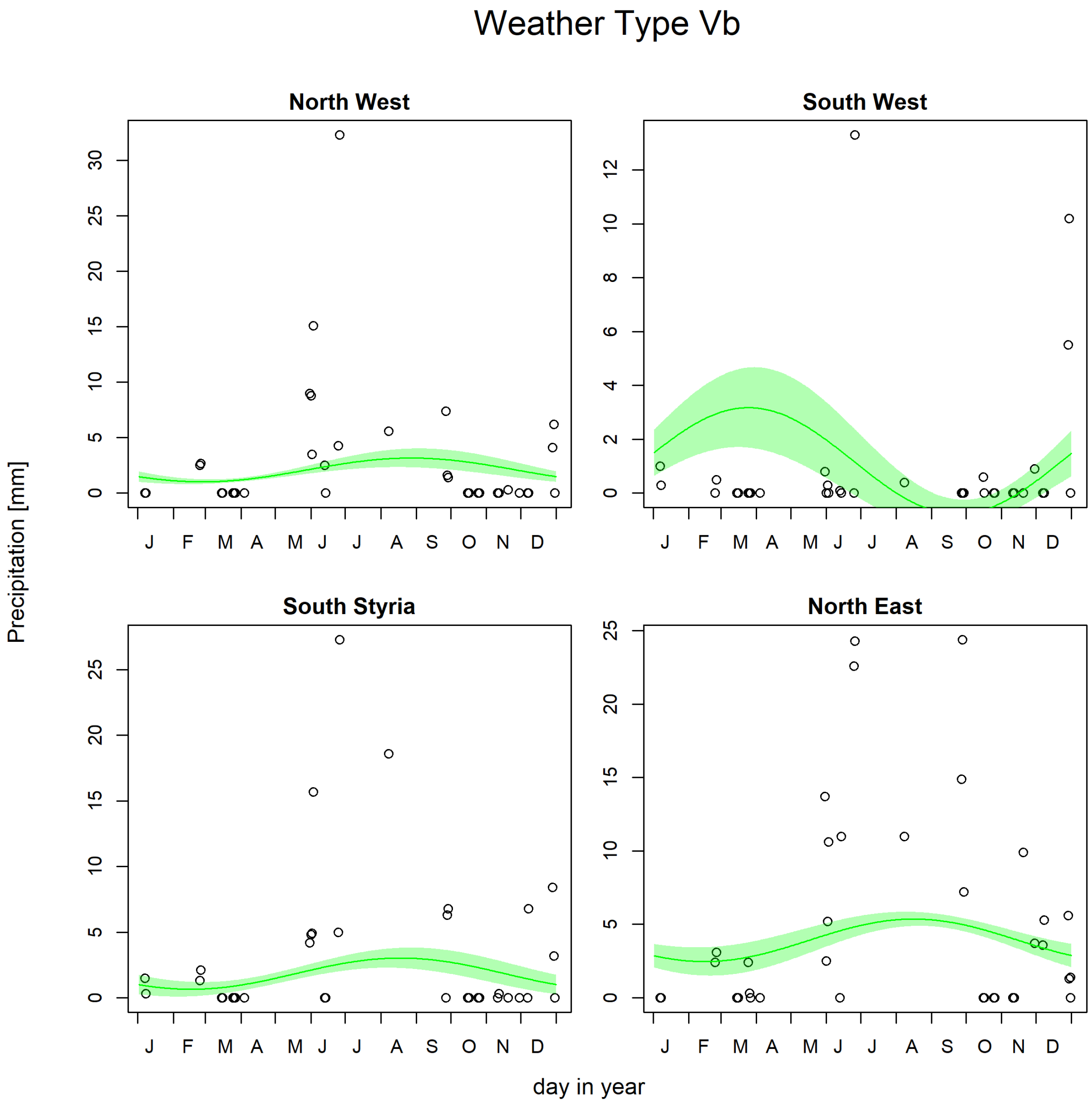

Figure 4.44: As Fig. 4.33 for Lauscher Class **Vb**

4.4 Atmospheric stability

In the following, an analysis of atmospheric stability during extreme precipitation events is conducted. Therefore, temperature gradients and profiles, as well as the convective available potential energy (CAPE) and the convective inhibition (CIN) are calculated at days of extreme events.

Extreme events are defined as the 10 strongest events of accumulated hourly precipitation within an ERA5 grid box in the period 2003-2016. If two of the hourly extreme events occur at the same day, this is considered as one single event to ensure to get 10 individual days for the analysis. This is done for four different regions in Austria (see Fig. 3.1), each defined such that it matches a 3×3 ERA5 grid box, and for each season separately.

For each event, the highest value of the temperature gradient, averaged between 1000 and 300 hPa, CAPE and CIN in the vicinity of the event is calculated, considering the nearest ERA5 grid point and the 9 surrounding ones. For the temperature gradient, all four 6-hourly values on the day of the event are considered, whereas for CAPE and CIN the value at midnight is excluded a priori, as high values are not expected at this time.

4.4.1 Temperature gradients and profiles

The obtained averaged temperature gradients associated with the extreme events (Fig. 4.45 to 4.48) all lie between 0.5 and 0.8 K per 100 m, with most values between 0.6 and 0.8 K per 100 m. Values below 0.6 K per 100 m are exclusively obtained in winter with one exception. The strongest gradients are found in spring in all regions, followed by summer, spring and winter.

The relationship between precipitation and temperature gradients obtained by linear regression in South Styria is positive for winter and autumn and slightly negative in spring and summer, meaning that the most extreme events do exhibit a slightly more stable atmosphere in spring. The results are the same for North East, with a positive relationship in spring and summer and a negative one in winter and autumn. In the Northern Stau region, there is a clear negative relationship visible in winter, whereas in the other season it is slightly positive or almost no trend can be seen. In South West, the relationship is negative in all seasons. Note however, that only the trends for South Styria in winter and autumn and for the Northern Stau region in winter are significant at the 95% level.

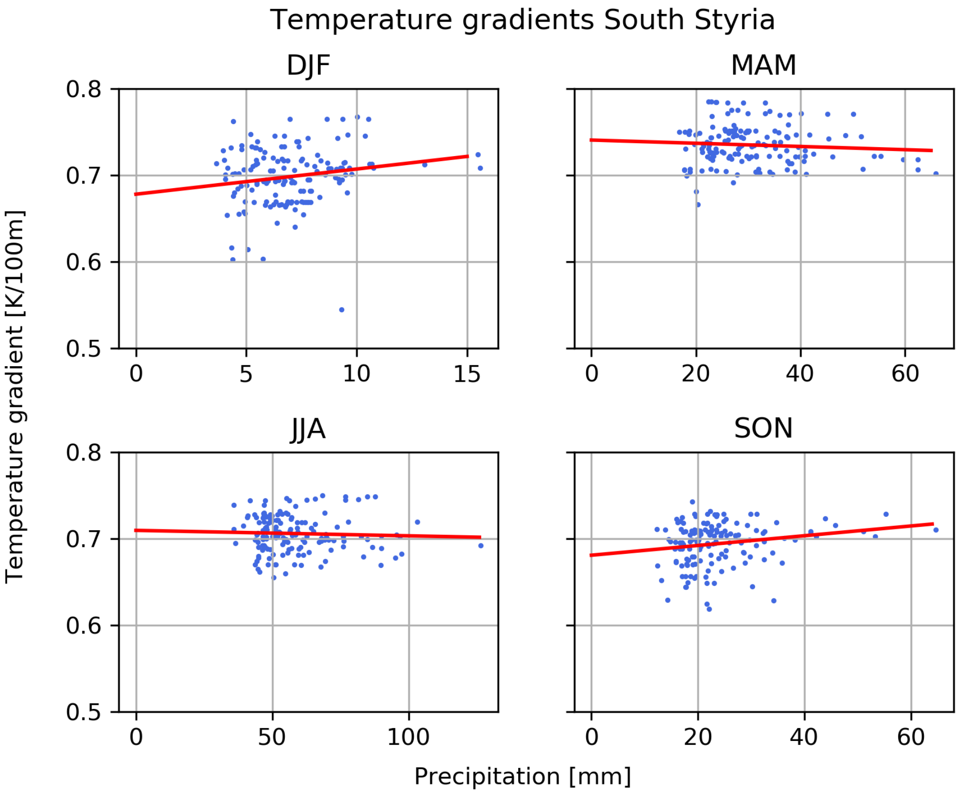

Figure 4.45: The strongest temperature gradients averaged between 1000 hPa and 300 hPa dependent on the accumulated hourly precipitation of the 10 strongest events within each ERA5 grid box for each season in the South Styria region. The red line gives the linear trend.

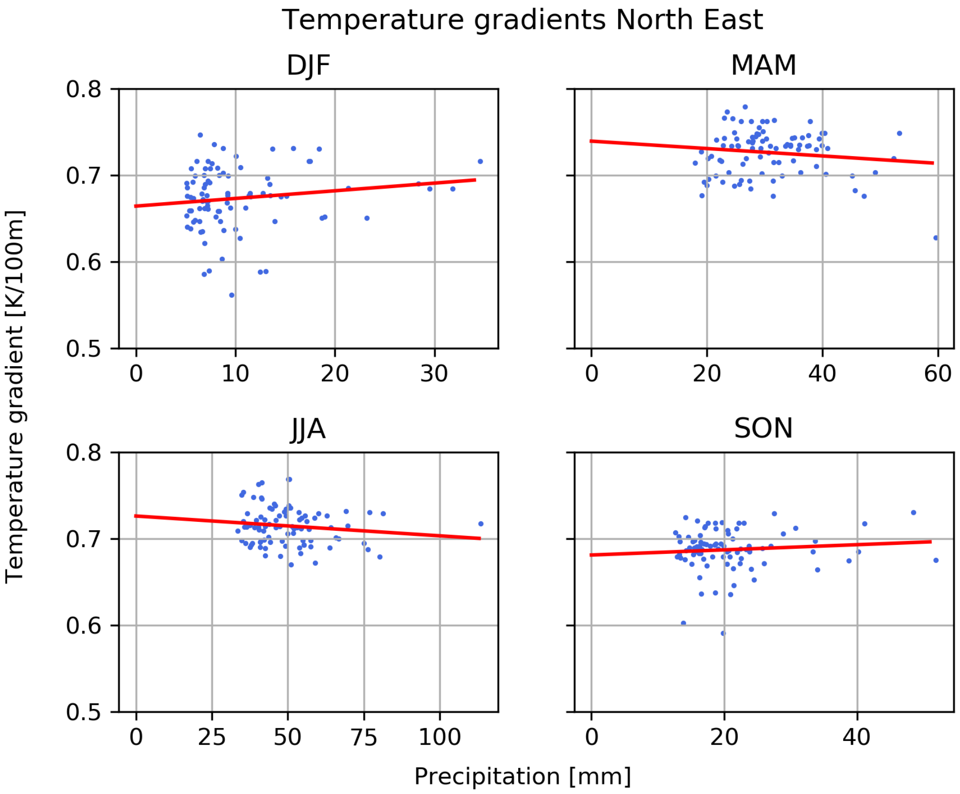

Figure 4.46: Same as in Fig. 4.45 for the North East region

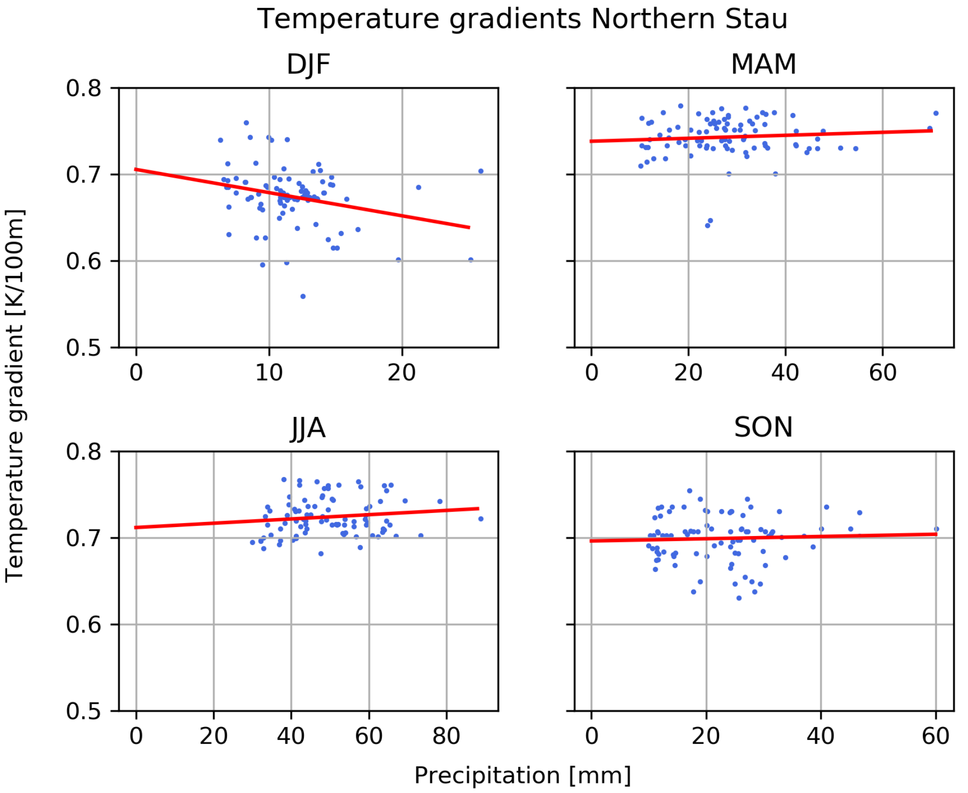

Figure 4.47: Same as in Fig. 4.45 for the Northern Stau region

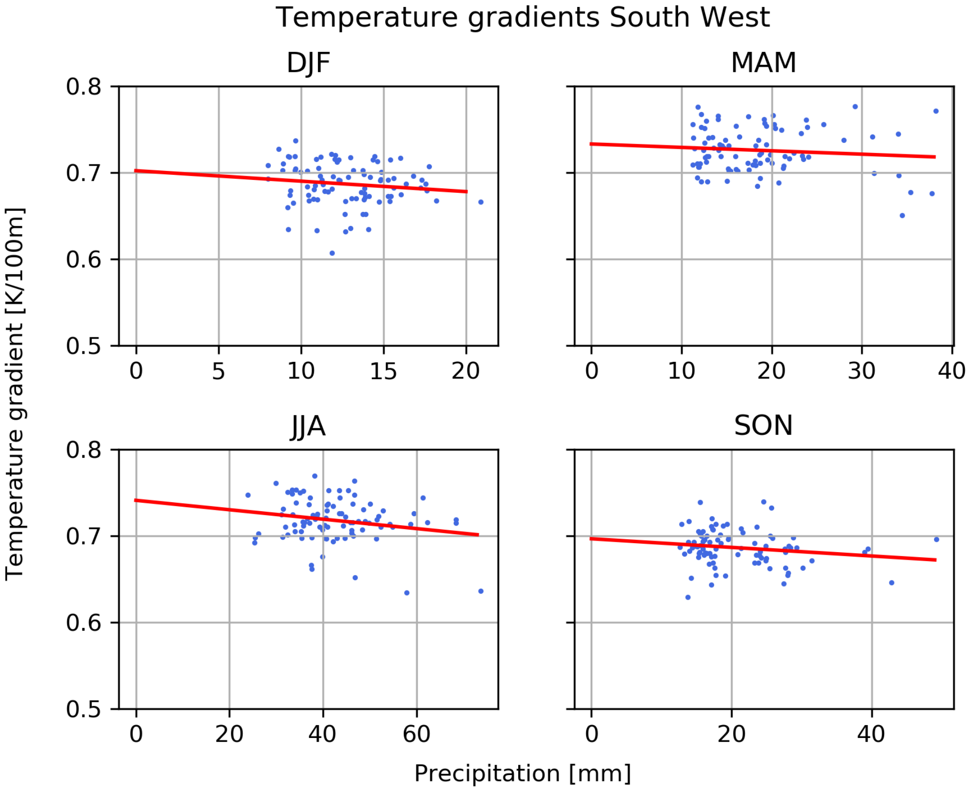

Figure 4.48: Same as in Fig. 4.45 for the South West region

Fig. 4.49 to 4.52 shows the averaged temperature profile of the events (solid blue line) at the grid point where the temperature gradient is strongest. The lapse rate does lie between the theoretical moist (dashed line) and dry (dotted line) adiabatic lapse rate (see (2.4) and (2.5)) for all regions and all seasons except for winter, where the lapse rate is slightly below the moist adiabatic lapse rate. Compared to the climatological mean (solid green line) the temperature averaged over the events is always higher at the surface and does decay faster than the climatological mean, mostly in the lower troposphere, because of a higher temperature gradient. In the Northern Stau and South West region the gradient of the events is especially strong between roughly 850 and 700 hPa, except for winter.

Loriaux et al. (2016) did find similar results when investigating precipitation events in the Netherlands, with a warmer atmosphere and higher gradients when going to more extreme events. They obtained the highest temperature gradients also between roughly 800 and 700 hPa.

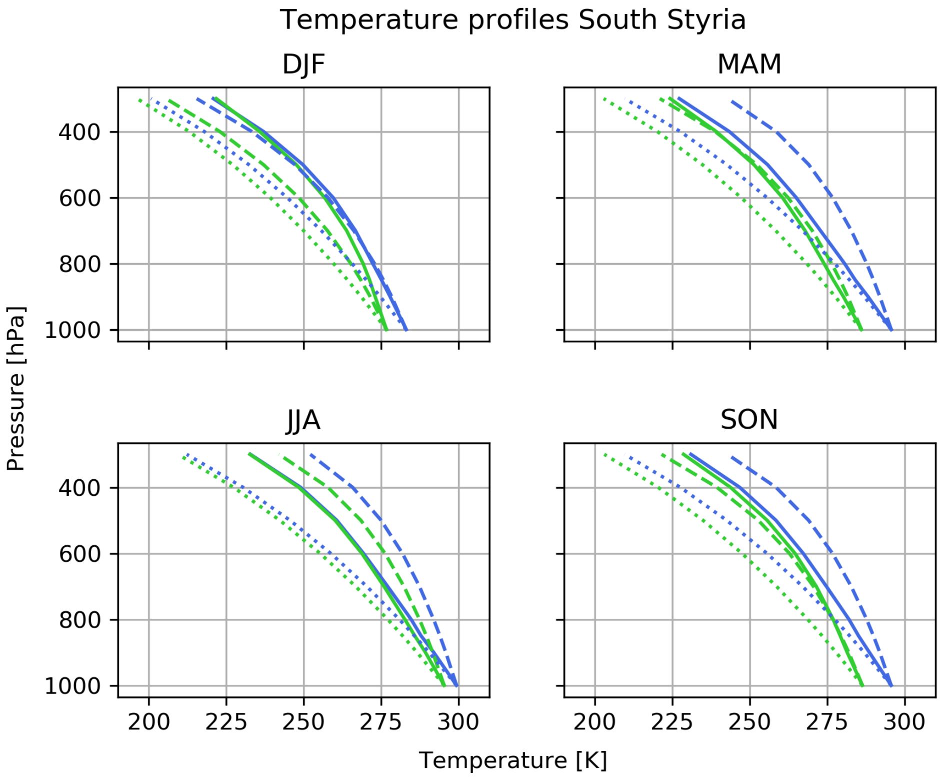

Figure 4.49: The mean temperature profile (blue solid line) of the 10 strongest events within each ERA5 grid box for each season in the South Styria region, obtained at the grid box of the highest temperature gradient. The blue dashed (dotted) line depicts the moist (dry) adiabatic lapse rate. The green lines are the same as the blue ones for the climatological (2003-2016) mean.

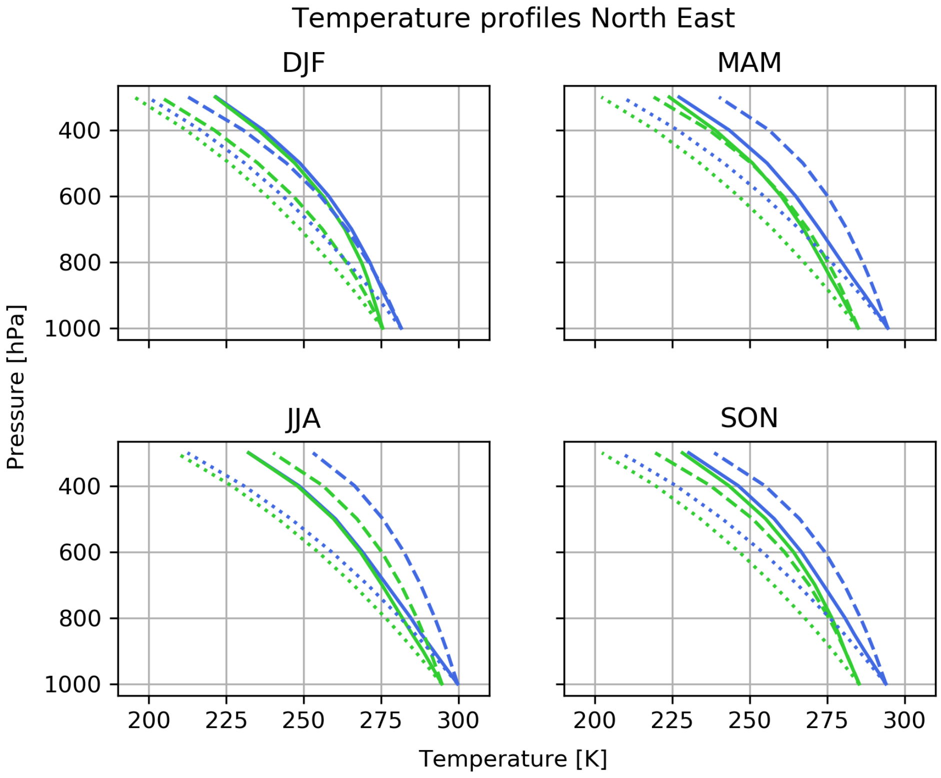

Figure 4.50: Same as in Fig. 4.49 for the North East region

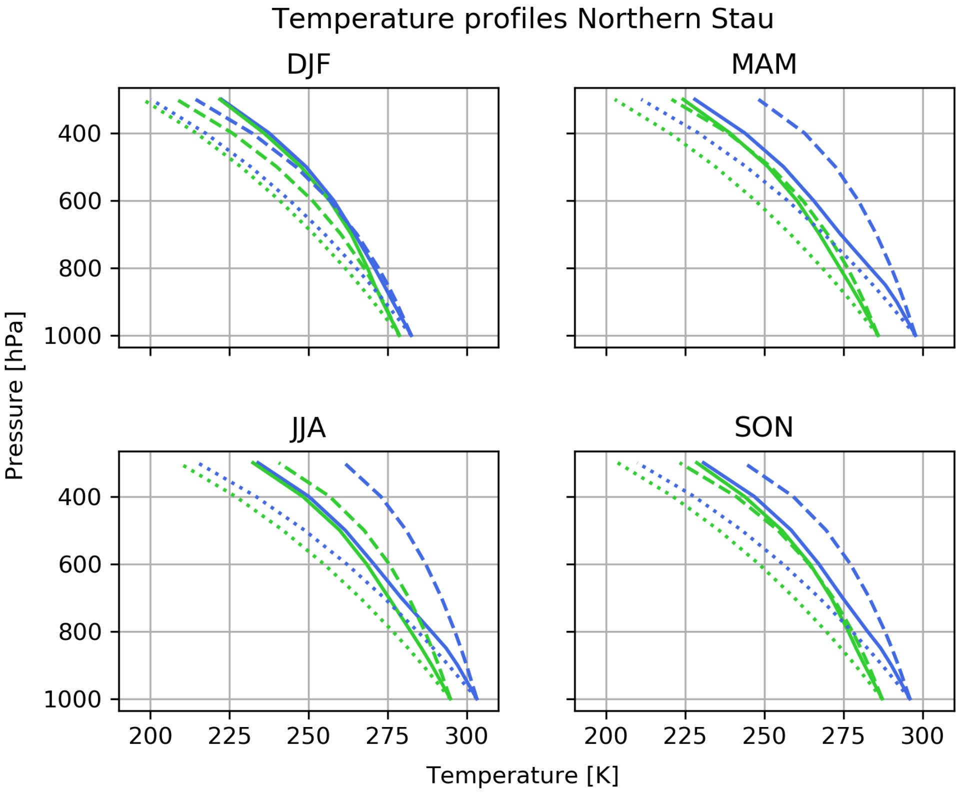

Figure 4.51: Same as in Fig. 4.49 for the Northern Stau region

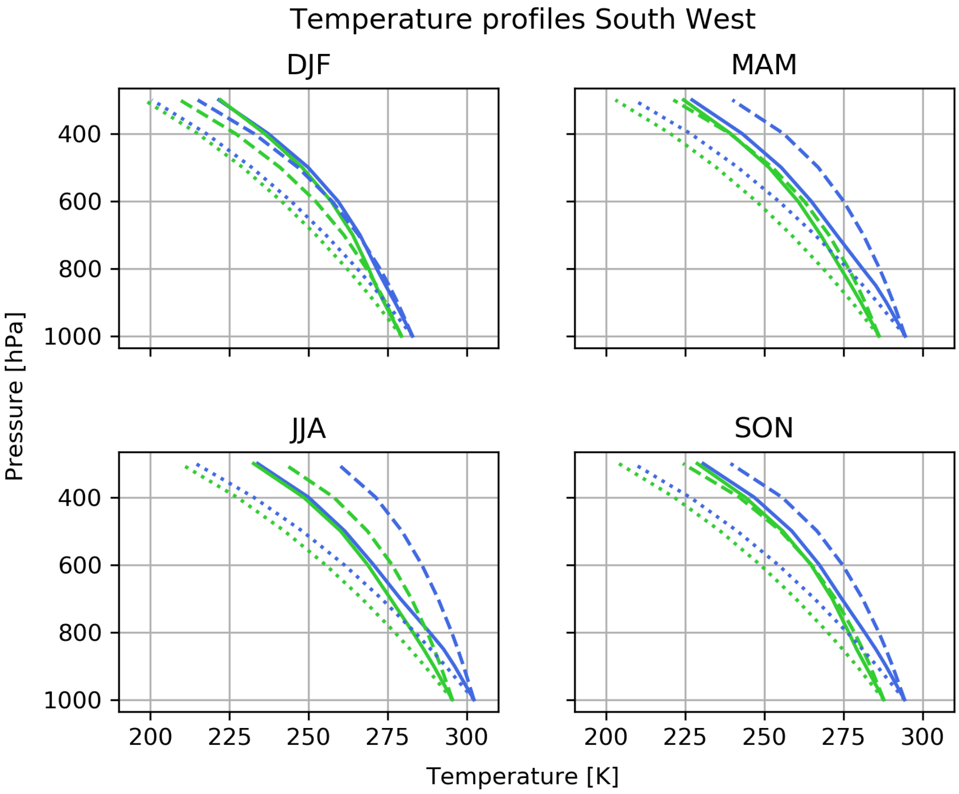

Figure 4.52: Same as in Fig. 4.49 for the South West region

4.4.2 CAPE and CIN

Fig. 4.53 to 4.56 shows the extreme precipitation values dependent on the obtained CAPE for each region. Not surprisingly, CAPE shows a clear seasonal cycle with lowest values in winter and highest values in summer for all regions. In the South Styria region, there are also large values (>3000 J/kg) obtained in spring. It is also the only region, where moderately high values (up to 500J/kg) in winter can be seen. The four outliers in spring, where CAPE exceeds 2000 J/kg, are all associated with comparably low to moderate precipitation values. In the South West and North East region, CAPE is higher in spring than in autumn on average.

There is no clear relationship immediately visible between CAPE and precipitation within these extreme events. Higher values of CAPE can lead to both very high and moderate extreme values. Vice versa, the most extreme events can be accompanied by very low CAPE and the weakest extremes are sometimes associated with a lot of CAPE. In some seasons in some regions there is a trend that the weakest extremes cannot be accompanied by high values of CAPE, e.g. South West and Northern Stau in summer or North East in autumn.

CIN (Fig. 4.57 to 4.60) is strongest in summer in all regions on average, but can exhibit high values also in spring and autumn. Although low values can lead to all kinds of extreme precipitation values from weak to strong, the stronger the CIN, the more restricted is the possible range of precipitation values towards weaker extremes. This can be seen in most regions and most seasons, but there are some exceptions. In the South Styria region in autumn for instance, there seems to be the opposite case that weaker CIN restricts the extreme precipitation to lower values. Additionally, in autumn CIN seems to be restricted to values above about -300 J/kg with one outlier at -600 J/kg.

A more objective assessment of the relationship between CAPE and CIN and the precipitation intensity can be given by fitting the data according to the supposed relationship given by (2.10). By rearrangement, a regression model can be developed of the type

$$ln(I) = c + \beta * ln(CAPE), \tag{4.3}$$

where c is a constant and β is the regression coefficient. The same model is applied also to the CIN values, following Lepore et al. (2016).

The obtained regression coefficients and their standard errors for each region and season are given in Tab. 4.2 and 4.3. For winter, only the data for South Styria was fitted, as in the other regions the obtained CAPE is mostly zero. The highest value in a region is written in bold and the highest value in a season is marked by *.

For CAPE, South Styria has regression coefficient between 0.2 and 0.5. The highest values are found for winter and summer, whereas the lowest is in autumn. In South West, the values are generally low, with 0.14 the highest one found in summer. The coefficients in spring and autumn are not significantly different from zero. In the Northern Stau region, the highest coefficients of all regions are found in spring and summer, significantly exceeding even the theoretical limit of 0.5. In autumn the relationship is much weaker compared to the other seasons. In North East, moderate values are found in spring and autumn, while the coefficient in summer is close to zero.

The differences between the individual regions are quite large, possibly indicating a varying importance of convective precipitation in the extreme events for the individual regions. While in North East and especially in South West only a rather weak or almost no relationship, depending on the season, is found, the relationship is clearly stronger in South Styria and the Northern Stau region. To explain the exceedance of the theoretical limit in spring and summer in the Northern Stau region, additional processes in forming these events and correlating with CAPE have to be assumed.

The obtained CAPE coefficients are comparable to those found by Lepore et al. (2015), especially those in South Styria. Interestingly, they noted a weaker relationship for summer than for winter, while here the highest coefficients are found in summer for all regions except North East. However, a coefficient for winter was only obtained for South Styria, where it is as high as in summer.

For CIN, the obtained relationships largely vary between regions and seasons. The values for the regression coefficients reach from highly negative (South Styria in winter, Northern Stau in spring and South West in all seasons) to highly positive (Northern Stau in summer). The positive values are surprising, as one would expect a negative relationship, as large values of CIN do hinder the rising of the air to the LFC and therefore the development of deep convection. Besides Northern Stau in summer, significant positive coefficients are obtained in South Styria in summer and autumn and in North East in spring. The negative relationships are much stronger than those found by Lepore et al. (2016), who obtained values all between 0 and -0.25. South West is the only region where consistent (negative) coefficients are found in all seasons.

This analysis could be influenced by the temporal and spatial resolution of the reanalysis dataset used for retrieving CAPE and CIN as well as temperature for calculating gradients and profiles, which is 6-hourly and $0.25° \times 0.25°$. The temporal resolution could be too coarse to effectively capture the peak values of those variables, which can exhibit large variations within 6 hours (Loriaux et al., 2016). For instance, a thunderstorm could build up in the afternoon after 12 UTC, cause an extreme event and collapse before 18 UTC, so that it won't be resolved in the reanal-

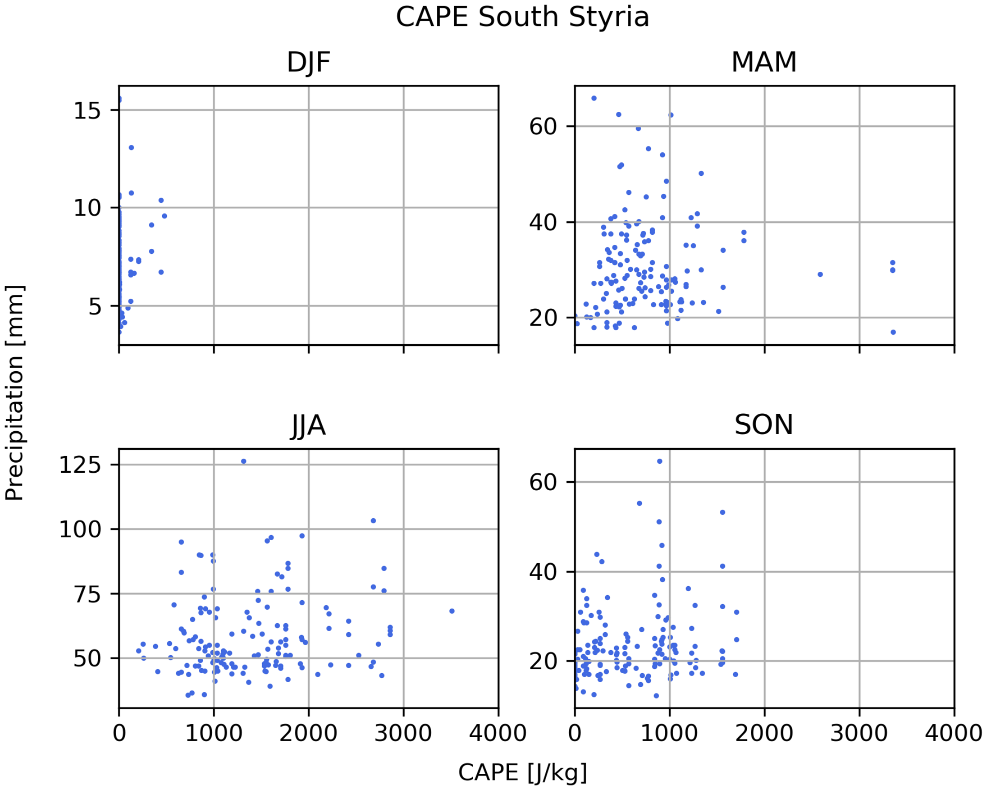

Figure 4.53: Accumulated hourly precipitation of the 10 strongest events within each ERA5 grid box for each season in the South Styria region, dependent on the CAPE of the event obtained at the surrounding grid box with the highest temperature gradient.

ysis data and eventually the strongest values would be missed. Dong et al. (2019) did not find a significant relationship between CAPE and extreme precipitation intensities and suggested that this might be because of the low temporal resolution of the CAPE data they used. Furthermore, the spatial resolution is coarse compared to the precipitation data, which is 1 km × 1 km. This means that for an event, which might be very localized and lead to extreme precipitation values at one grid point only (e.g. a small thunderstorm cell), CAPE and CIN are obtained for an area much larger than the actual event region. Hence it would tend to underestimate the CAPE and CIN values for such events.

While this could be an explanation of rather low CAPE regression coefficients in some regions, it would raise further scepticism for values >0.5. Further investigations on these considerations were beyond the scope of this thesis, but it seems likely that an analysis with higher resolved reanalysis data would provide more reliable results.

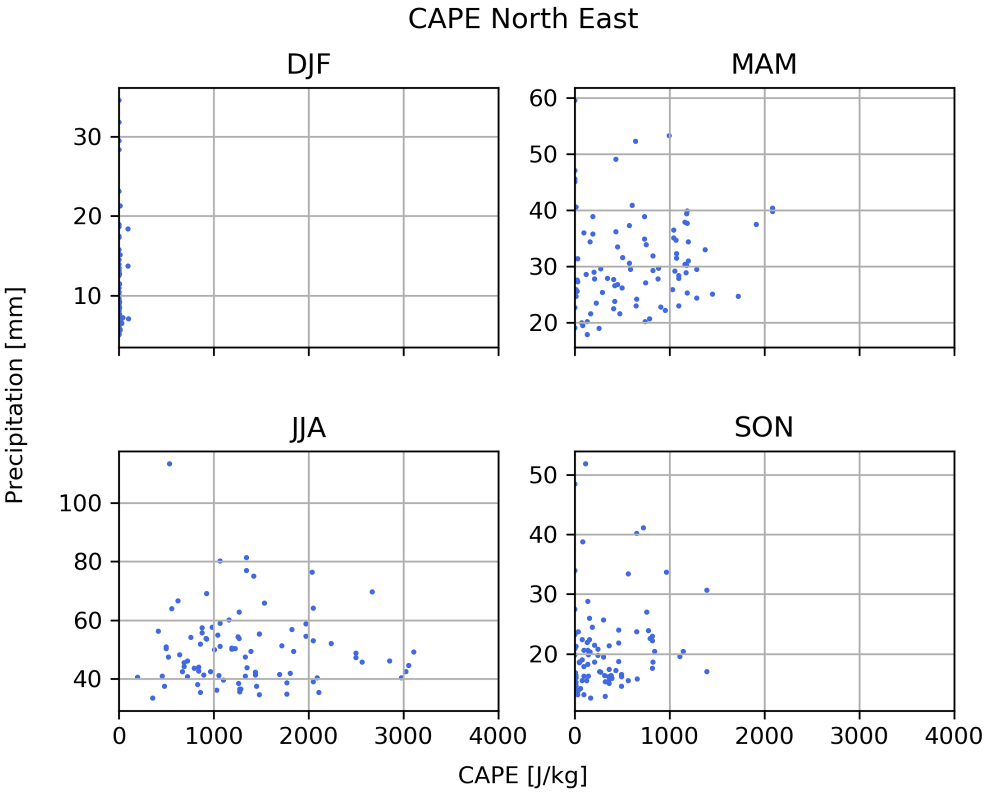

Figure 4.54: Same as in Fig. 4.53 for the North East region

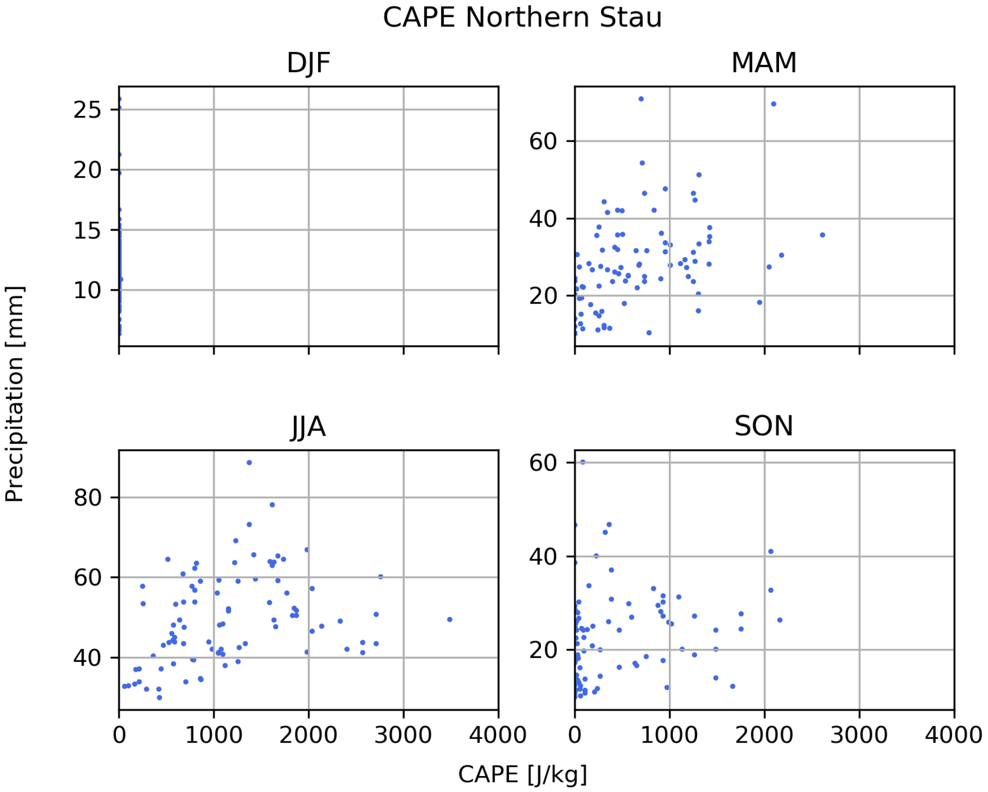

Figure 4.55: Same as in Fig. 4.53 for the Northern Stau region

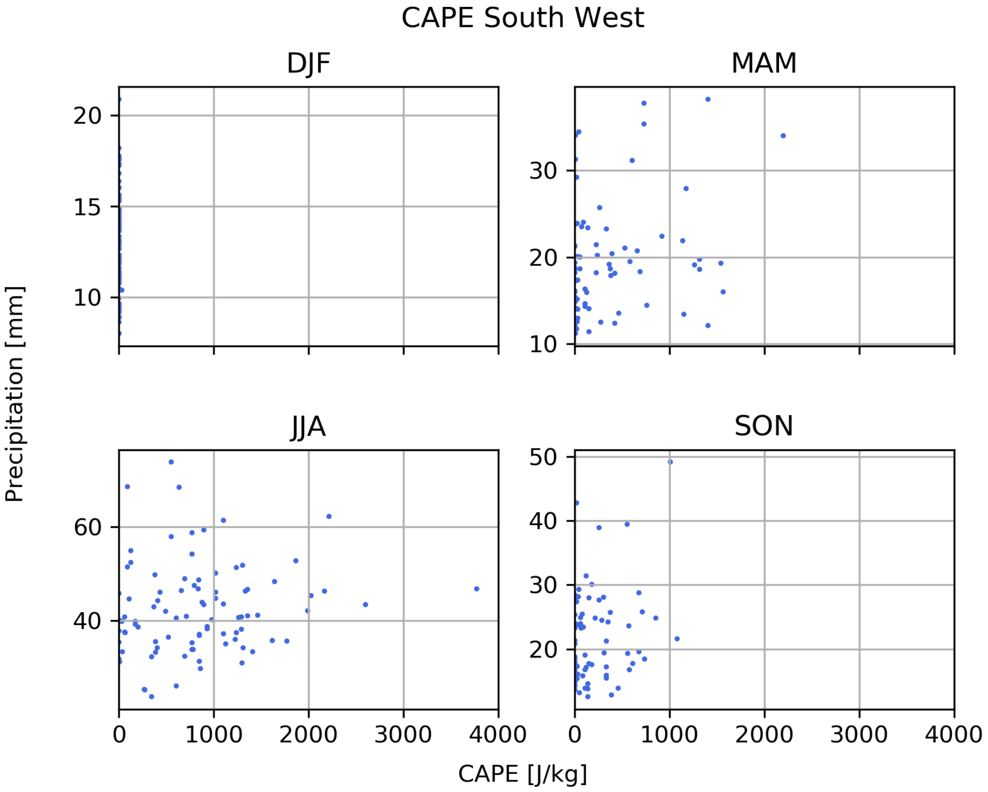

Figure 4.56: Same as in Fig. 4.53 for the South West region

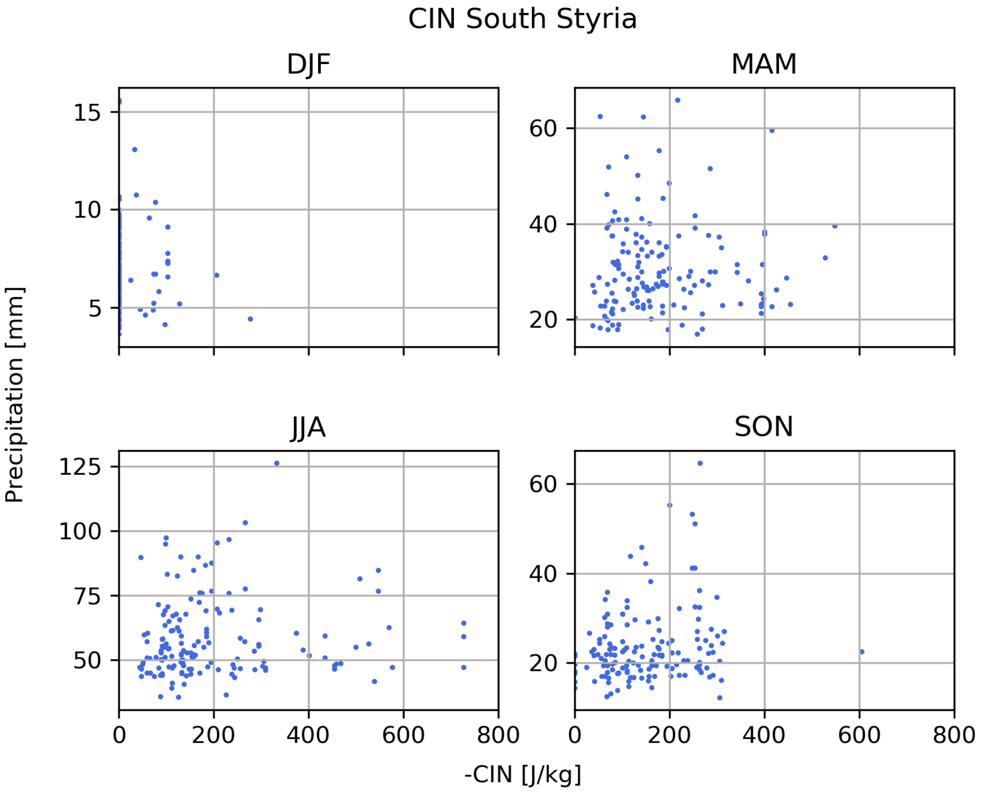

Figure 4.57: Accumulated hourly precipitation of the 10 strongest events within each ERA5 grid box for each season in the South Styria region, dependent on the CIN of the event obtained at the surrounding grid box with the highest temperature gradient.

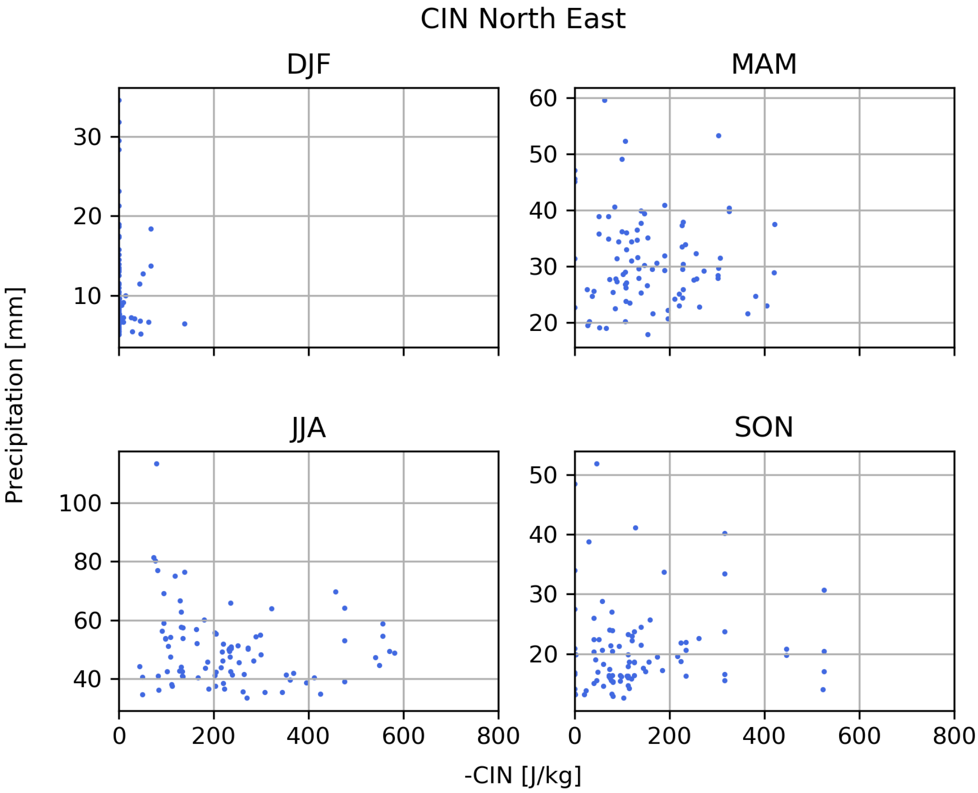

Figure 4.58: Same as in Fig. 4.57 for the North East region

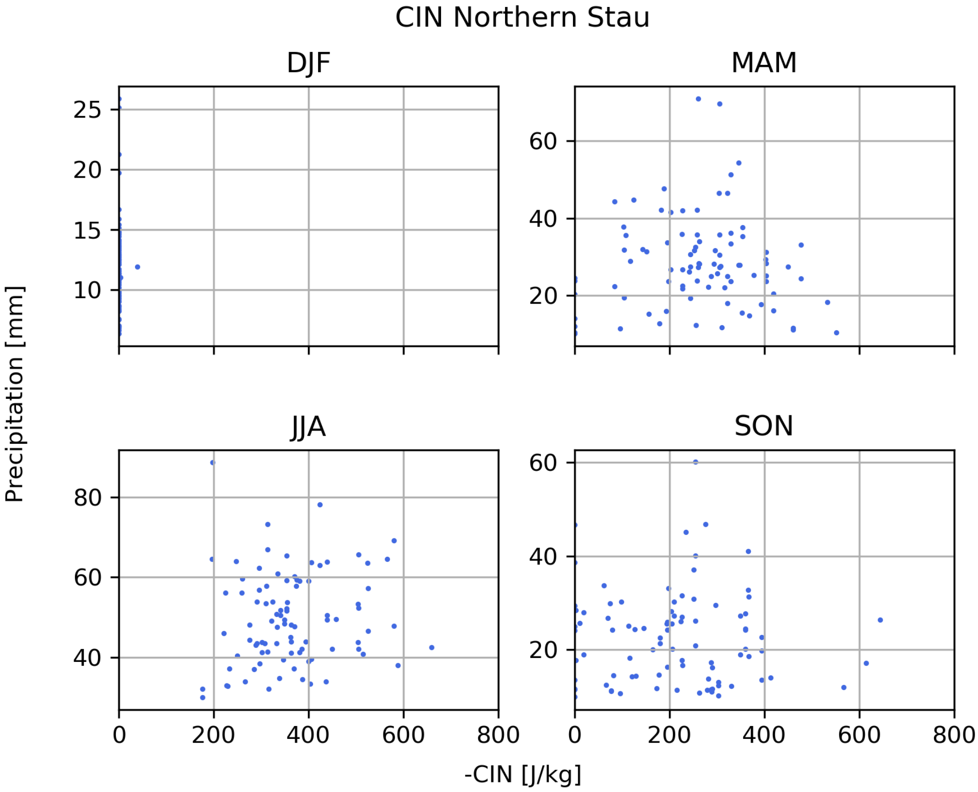

Figure 4.59: Same as in Fig. 4.57 for the Northern Stau region

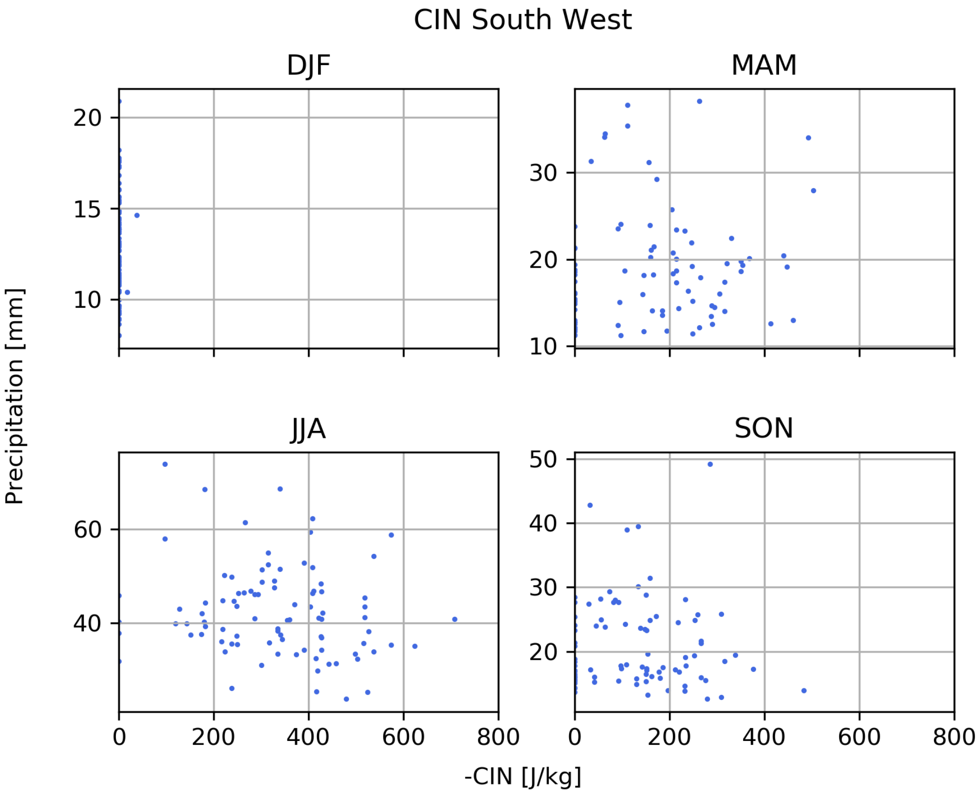

Figure 4.60: Same as in Fig. 4.57 for the South West region

Table 4.2: Regression coefficients and their standard errors for the regression model given by (4.3). The highest value in a region is written in bold and the highest value in a season is marked by *

	South Styria	**South West**	**Northern Stau**	**North East**
DJF	0.47+0.19*	-	-	-
MAM	0.36+0.22	0.10+0.12	0.78+0.22*	0.19+0.11
JJA	**0.47+0.26**	**0.14+0.11**	**0.90+0.17***	0.04+0.31
SON	0.22+0.13	0.07+0.16	0.23+0.13	**0.30+0.10***

Table 4.3: As Tab. 4.2 for CIN

	South Styria	**South West**	**Northern Stau**	**North East**
DJF	-0.79+0.51			
MAM	0.14+0.20	-0.82+0.38	-0.74+0.56	0.27+0.19
JJA	0.22+0.15	-0.76+0.31	0.71+0.50	-0.38+0.20
SON	0.34+0.20	-0.60+0.27	-0.08+0.29	0.19+0.20

Chapter 5

Summary and conclusion

Several drivers of extreme precipitation in Europe and Austria were investigated. The GEV distribution as well as sensitivities on return levels obtained by the estimated parameters where calculated for possible large-scale drivers, namely the SNAO, the SEA, tropical precipitation and the Indian Summer Monsoon. The location and scale parameters μ and σ were modelled as linear dependent on the index of the corresponding drivers, while the shape parameter ξ was kept constant. The shift of the location of the GEV distribution dependent on the driver was often comparable to the findings on mean precipitation (Bladé et al., 2012; Wulff et al., 2017; Ossó et al., 2019). Regions of positive correlation between mean precipitation and the phase of the driver do also show a shift of the GEV distribution towards higher extremes and vice versa. The pattern for tropical precipitation is shifted southeastward compared to the SEA. The variations of the scale parameter with the phase of the driver is either insignificant almost everywhere or only significant in some small regions. However, as the return levels are sensitive to changes in the scale parameter, the resulting patterns of the sensitivity on the return levels can differ from those of the location parameter. Worth mentioning are the contradicting patterns found for the SEA and tropical precipitation. For the Indian Summer Monsoon, a region of both significant positive location and scale parameter shifts were found in western Germany/eastern Poland, which was not seen for mean precipitation.

A composite analysis of the jet stream and moisture availability and transport at days of extreme precipitation events in four regions and all seasons in Austria was conducted. Differences where found between regions on the southern and the northern side of the Alps. While extremes in the northern region were caused by strong moisture inflow from northwest to northeast and accompanied by the jet stream lying in a northwest to southeast direction over central Europe, the regions on the southern side exhibited extreme events which were characterized by moisture transport from the Mediterranean Sea and a meander of the jet stream to the west to southwest of Austria. The results for the North East region suggest that extremes in this region can be associated with a wider spectrum of large-scale conditions.

The impact of different synoptic conditions on extreme precipitation over Austria were further analysed by estimating the GPD for days where a certain weather type occurred. The weather types were based on the classification of Lauscher (1972). The classes with the highest impact were found to be those who are associated with low pressure systems either over or south of Austria. The highest return levels were found at the southern border of Austria for almost every class. Additionally, the seasonal cycle was fitted to precipitation data of the several classes in the four regions. The maxima were found to be mostly in the summer months for both moderate and high percentiles. Exceptions are seen e.g. for class N. The 95th percentile does exhibit more pronounced maxima and minima than lower percentiles.

To investigate the atmospheric stability during or prior to extreme precipitation events, temperature gradients and profiles, as well as CAPE and CIN were calculated. The atmosphere was found to be warmer and more unstable than in the climatological mean during these events. The temperature gradients averaged between 1000 and 300 hPa lie mostly between 0.6 and 0.8 K/100 m, with the strongest gradients found in spring. No significant trend towards either higher or lower gradients for higher intensities was seen for most regions and seasons within those extremes. Both high and low values of CAPE and CIN can lead to extreme events. A positive relationship between CAPE and precipitation intensities was obtained, especially in spring and summer in the Northern Stau region. The relationship with CIN can be either positive or negative, with large variations between individual regions and seasons.

These results highlight the importance of drivers at a wide variety of scales for extreme precipitation in Europe and Austria. Large-scale drivers are important by altering the large-scale circulation and increasing the probability for e.g. an extratropical cyclone to develop in or move over a specific region. These synoptic systems furthermore can destabilize the atmosphere and cause moisture to be transported into or be converged in an area, where then, depending on regional to local scale factors, a precipitation event can be triggered. The interplay between those scales is crucial for assessing the conditions under which extreme precipitation events occur. the results show that the probability and severity of extreme precipitation in Europe can be influenced by remote conditions around the globe. In Austria, their are large differences between favourable conditions for individual regions, especially at the synoptic scale, meaning that those regions have to be treated separately. Atmospheric instability does play an important role in triggering extreme events, but is not essential. Beside those studied in this thesis, also many other drivers are relevant for extreme precipitation and need to be considered.

Bibliography

Adler, R. F., Sapiano, M. R. P., Huffman, G. J., Wang, J.-J., Gu, G., Bolvin, D., Chiu, L., Schneider, U., Becker, A., Nelkin, E., Xie, P., Ferraro, R., and Shin, D.-B. (2018). The Global Precipitation Climatology Project (GPCP) Monthly Analysis (New Version 2.3) and a Review of 2017 Global Precipitation. *Atmosphere*, 9(4):138. Number: 4 Publisher: Multidisciplinary Digital Publishing Institute.

Allen, M. R. and Ingram, W. J. (2002). Constraints on future changes in climate and the hydrologic cycle. *Nature*, 419(6903):228–232. Number: 6903 Publisher: Nature Publishing Group.

Ashok, K., Guan, Z., and Yamagata, T. (2001). Impact of the Indian Ocean dipole on the relationship between the Indian monsoon rainfall and ENSO. *Geophysical Research Letters*, 28(23):4499–4502. _eprint: https://agupubs.onlinelibrary.wiley.com/doi/pdf/10.1029/2001GL013294.

Barbero, R., Abatzoglou, J. T., and Fowler, H. J. (2019). Contribution of large-scale midlatitude disturbances to hourly precipitation extremes in the United States. *Climate Dynamics*, 52(1-2):197–208.

Barlow, M., Gutowski, W. J., Gyakum, J. R., Katz, R. W., Lim, Y.-K., Schumacher, R. S., Wehner, M. F., Agel, L., Bosilovich, M., Collow, A., Gershunov, A., Grotjahn, R., Leung, R., Milrad, S., and Min, S.-K. (2019). North American extreme precipitation events and related large-scale meteorological patterns: a review of statistical methods, dynamics, modeling, and trends. *Climate Dynamics*, 53(11):6835–6875.

Barry, R. and Chorley, R. (1984). Atmosphere, weather and climate / by R. G. Barry and R. J. Chorley. *SERBIULA (sistema Librum 2.0)*.

Beck, C. and Philipp, A. (2010). Evaluation and comparison of circulation type classifications for the European domain. *Physics and Chemistry of the Earth, Parts A/B/C*, 35(9-12):374–387.

Ben Alaya, M. A., Zwiers, F., and Zhang, X. (2020). An Evaluation of Block-Maximum-Based Estimation of Very Long Return Period Precipitation Extremes with a Large Ensemble Climate Simulation. *Journal of Climate*, 33.

Bladé, I., Liebmann, B., Fortuny, D., and van Oldenborgh, G. J. (2012). Observed and simulated impacts of the summer NAO in Europe: implications for projected drying in the Mediterranean region. *Climate Dynamics*, 39(3-4):709–727.

Chronis, T., Raitsos, D. E., Kassis, D., and Sarantopoulos, A. (2011). The Summer North Atlantic Oscillation Influence on the Eastern Mediterranean. *Journal of Climate*, 24(21):5584–5596.

Coles, S. (2001). *An introduction to statistical modeling of extreme values*. Springer series in statistics. Springer, London ; New York.

Cornes, R. C., van der Schrier, G., van den Besselaar, E. J. M., and Jones, P. D. (2018). An Ensemble Version of the E-OBS Temperature and Precipitation Data Sets. *Journal of Geophysical Research: Atmospheres*, 123(17):9391–9409.

Coumou, D., Petoukhov, V., Rahmstorf, S., Petri, S., and Schellnhuber, H. J. (2014). Quasi-resonant circulation regimes and hemispheric synchronization of extreme weather in boreal summer. *Proceedings of the National Academy of Sciences*, 111(34):12331–12336. Publisher: National Academy of Sciences Section: Physical Sciences.

Dong, W., Lin, Y., Wright, J. S., Xie, Y., Yin, X., and Guo, J. (2019). Precipitable water and CAPE dependence of rainfall intensities in China. *Climate Dynamics*, 52(5-6):3357–3368.

Doswell, C. A., Brooks, H. E., and Maddox, R. A. (1996). Flash Flood Forecasting: An Ingredients-Based Methodology. *WEATHER AND FORECASTING*, 11:22.

Fischer, E. M., Sedláček, J., Hawkins, E., and Knutti, R. (2014). Models agree on forced response pattern of precipitation and temperature extremes. *Geophysical Research Letters*, 41(23):8554–8562. _eprint: https://agupubs.onlinelibrary.wiley.com/doi/pdf/10.1002/2014GL062018.

Folland, C. K., Knight, J., Linderholm, H. W., Fereday, D., Ineson, S., and Hurrell, J. W. (2009). The Summer North Atlantic Oscillation: Past, Present, and Future. *Journal of Climate*, 22(5):1082–1103.

Grams, C. M., Binder, H., Pfahl, S., Piaget, N., and Wernli, H. (2014). Atmospheric processes triggering the central European floods in June 2013. *Natural Hazards and Earth System Sciences*, 14(7):1691–1702. Publisher: Copernicus GmbH.

Grazzini, F. and van der Grijn, G. (2002). Central European Floods during summer 2002. *ECMWF Newsletter*, 96.

Hersbach, H., Bell, B., Berrisford, P., Hirahara, S., Horányi, A., Muñoz-Sabater, J., Nicolas, J., Peubey, C., Radu, R., Schepers, D., Simmons, A., Soci, C., Abdalla, S., Abellan, X., Balsamo, G., Bechtold, P., Biavati, G., Bidlot, J., Bonavita, M., Chiara, G. D., Dahlgren, P., Dee, D., Diamantakis, M., Dragani, R., Flemming, J., Forbes, R., Fuentes, M., Geer, A., Haimberger, L., Healy, S., Hogan, R. J., Hólm, E., Janisková, M., Keeley, S., Laloyaux, P., Lopez, P., Lupu, C., Radnoti, G., Rosnay, P. d., Rozum, I., Vamborg, F., Villaume, S., and Thépaut, J.-N. (2020). The ERA5 global reanalysis. *Quarterly Journal of the Royal Meteorological Society*, 146(730):1999–2049. _eprint: https://rmets.onlinelibrary.wiley.com/doi/pdf/10.1002/qj.3803.

Hess, P. and Brezowsky, H. (1999). *Katalog der Großwetterlagen Europas*. Potsdam, 5. verbesserte und ergänzte auflage edition.

Hiebl, J. and Frei, C. (2018). Daily precipitation grids for Austria since 1961—development and evaluation of a spatial dataset for hydroclimatic monitoring and modelling. *Theoretical and Applied Climatology*, 132(1):327–345.

Hofstätter, M., Lexer, A., Homann, M., and Blöschl, G. (2018). Large-scale heavy precipitation over central Europe and the role of atmospheric cyclone track types. *International Journal of Climatology*, 38(S1):e497–e517. _eprint: https://rmets.onlinelibrary.wiley.com/doi/pdf/10.1002/joc.5386.

Holton, J. R. (2004). *An introduction to dynamic meteorology*. Number v. 88 in International geophysics series. Elsevier Academic Press, Burlington, MA, 4th ed edition. OCLC: 54400282.

Hurrell, J., Kushnir, Y., Ottersen, G., and Visbeck, M. (2003a). *The North Atlantic Oscillation: Climatic Significance and Environmental Impact*, volume 134. Journal Abbreviation: Geophys. Monogr. Ser. Publication Title: Geophys. Monogr. Ser.

Hurrell, J. W., Kushnir, Y., Ottersen, G., and Visbeck, M. (2003b). An overview of the North Atlantic Oscillation. In Hurrell, J. W., Kushnir, Y., Ottersen, G., and Visbeck, M., editors, *Geophysical Monograph Series*, volume 134, pages 1–35. American Geophysical Union, Washington, D. C.

Šimková, T. and Picek, J. (2017). A comparison of L-, LQ-, TL-moment and maximum likelihood high quantile estimates of the GPD and GEV distribution. *Communications in Statistics - Simulation and*

Computation, 46(8):5991–6010. Publisher: Taylor & Francis _eprint: https://doi.org/10.1080/03610918.2016.1188206.

Iribarne, J. V. and Godson, W. L. (1981). *Atmospheric Thermodynamics*. Springer Netherlands, Dordrecht.

Kalnay, E., Kanamitsu, M., Kistler, R., Collins, W., Deaven, D., Gandin, L., Iredell, M., Saha, S., White, G., Woollen, J., Zhu, Y., Chelliah, M., Ebisuzaki, W., Higgins, W., Janowiak, J., Mo, K. C., Ropelewski, C., Wang, J., Leetmaa, A., Reynolds, R., Jenne, R., and Joseph, D. (1996). The NCEP/NCAR 40-Year Reanalysis Project. *Bulletin of the American Meteorological Society*, 77(3):437–472. Publisher: American Meteorological Society.

Koch, P., Wernli, H., and Davies, H. C. (2006). An event-based jet-stream climatology and typology. *International Journal of Climatology*, 26(3):283–301.

Langousis, A., Mamalakis, A., Puliga, M., and Deidda, R. (2016). Threshold detection for the generalized Pareto distribution: Review of representative methods and application to the NOAA NCDC daily rainfall database. *Water Resources Research*, 52(4):2659–2681. _eprint: https://agupubs.onlinelibrary.wiley.com/doi/pdf/10.1002/2015WR018502.

Lauscher, F. (1972). Wetter und Leben: Jahrgang 24/Heft 9-10 - PDF - CCCA Data Server.

Lavers, D. A., Hannah, D. M., and Bradley, C. (2015). Connecting large-scale atmospheric circulation, river flow and groundwater levels in a chalk catchment in southern England. *Journal of Hydrology*, 523:179–189.

Lee, S. and Kim, H.-k. (2003). The Dynamical Relationship between Subtropical and Eddy-Driven Jets. *Journal of the Atmospheric Sciences*, 60(12):1490–1503. Publisher: American Meteorological Society.

Lepore, C., Allen, J. T., and Tippett, M. K. (2016). Relationships between Hourly Rainfall Intensity and Atmospheric Variables over the Contiguous United States. *Journal of Climate*, 29(9):3181–3197.

Lepore, C., Veneziano, D., and Molini, A. (2015). Temperature and CAPE dependence of rainfall extremes in the eastern United States. *Geophysical Research Letters*, 42(1):74–83.

Lima, C. H. R., Lall, U., Troy, T., and Devineni, N. (2016). A hierarchical Bayesian GEV model for improving local and regional flood quantile estimates. *Journal of Hydrology*, 541:816–823.

Loriaux, J. M., Lenderink, G., and Siebesma, A. P. (2016). Peak precipitation intensity in relation to atmospheric conditions and large-scale forcing at midlatitudes: PEAK INTENSITY RELATED TO THE ATMOSPHERE. *Journal of Geophysical Research: Atmospheres*, 121(10):5471–5487.

Lynch, A. and Cassano, J. (2006). Applied Atmospheric Dynamics.

Maraun, D., Rust, H., and Osborn, T. (2009). The annual cycle of heavy precipitation across the United Kingdom: A model based on extreme value statistics. *International Journal of Climatology*, 29:1731–1744.

Mariotti, A. and Arkin, P. (2006). The North Atlantic Oscillation and oceanic precipitation variability. *Climate Dynamics*, 28(1):35–51.

Mariotti, A. and Dell'Aquila, A. (2012). Decadal climate variability in the Mediterranean region: roles of large-scale forcings and regional processes. *Climate Dynamics*, 38(5-6):1129–1145.

Martinez-Villalobos, C. and Neelin, J. D. (2019). Why Do Precipitation Intensities Tend to Follow Gamma Distributions? *Journal of the Atmospheric Sciences*, 76(11):3611–3631. Publisher: American Meteorological Society.

Messmer, M., Gómez-Navarro, J. J., and Raible, C. C. (2015). Climatology of Vb cyclones, physical mechanisms and their impact on extreme precipitation over Central Europe. *Earth System Dynamics*, 6(2):541–553.

Nair, P. J., Chakraborty, A., Varikoden, H., Francis, P. A., and Kuttippurath, J. (2018). The local and global climate forcings induced inhomogeneity of Indian rainfall. *Scientific Reports*, 8(1):6026. Number: 1 Publisher: Nature Publishing Group.

North, G. R. and Erukhimova, T. L. (2009). *Atmospheric Thermodynamics : Elementary Physics and Chemistry*. Cambridge University Press, Cambridge, UK.

Ossó, A., Shaffrey, L., Dong, B., and Sutton, R. (2019). Impact of air–sea coupling on Northern Hemisphere summer climate and the monsoon–desert teleconnection. *Climate Dynamics*, 53(7-8):5063–5078.

Panetta, R. L. (1993). Zonal Jets in Wide Baroclinically Unstable Regions: Persistence and Scale Selection. *Journal of the Atmospheric Sciences*, 50(14):2073–2106. Publisher: American Meteorological Society.

Petoukhov, V., Rahmstorf, S., Petri, S., and Schellnhuber, H. J. (2013). Quasiresonant amplification of planetary waves and recent Northern Hemisphere weather extremes. *Proceedings of the National Academy of Sciences of the United States of America*, 110(14):5336–5341.

Pfahl, S., O'Gorman, P. A., and Fischer, E. M. (2017). Understanding the regional pattern of projected future changes in extreme precipitation. *NATURE CLIMATE CHANGE*, page 7.

Rahimpour, V., Zeng, Y., Mannaerts, C. M., and Su, Z. B. (2016). Attributing seasonal variation of daily extreme precipitation events across The Netherlands. *Weather and Climate Extremes*, 14:56–66.

Rodwell, M. J. and Hoskins, B. J. (1996). Monsoons and the dynamics of deserts. *Quarterly Journal of the Royal Meteorological Society*, 122(534):1385–1404. _eprint: https://rmets.onlinelibrary.wiley.com/doi/pdf/10.1002/qj.49712253408.

Rust, H., Maraun, D., and Osborn, T. (2009). Modelling seasonality in extreme precipitation: A UK case study. *The European Physical Journal Special Topics*, 174:99–111.

Sardeshmukh, P. D. and Hoskins, B. J. (1988). The Generation of Global Rotational Flow by Steady Idealized Tropical Divergence. *Journal of the Atmospheric Sciences*, 45(7):1228–1251. Publisher: American Meteorological Society.

Schüepp, M. (1968). Kalender der Wetter- und Witterungslagen von 1955 bis 1967 im zentralen Alpengebiet.

Screen, J. and Simmonds, I. (2014). Amplified mid-latitude planetary waves favour particular regional weather extremes. *Nature Climate Change*, 4:704–709.

Seibert, P., Frank, A., and Formayer, H. (2007). Synoptic and regional patterns of heavy precipitation in Austria. *Theoretical and Applied Climatology*, 87(1-4):139–153.

Shukla, R. P. and Huang, B. (2016). Interannual variability of the Indian summer monsoon associated with the air–sea feedback in the northern Indian Ocean. *Climate Dynamics*, 46(5):1977–1990.

Stadtherr, L., Coumou, D., Petoukhov, V., Petri, S., and Rahmstorf, S. (2016). Record Balkan floods of 2014 linked to planetary wave resonance. *Science Advances*, 2(4):e1501428.

Tabari, H. and Willems, P. (2018). Lagged influence of Atlantic and Pacific climate patterns on European extreme precipitation. *Scientific Reports*, 8(1):5748. Number: 1 Publisher: Nature Publishing Group.

Toreti, A., Xoplaki, E., Maraun, D., Kuglitsch, F. G., Wanner, H., and Luterbacher, J. (2010). Characterisation of extreme winter precipitation in Mediterranean coastal sites and associated anomalous atmospheric circulation patterns. *Natural Hazards and Earth System Sciences*, 10(5):1037–1050.

Tyrlis, E. (2013). The summer circulation over the eastern Mediterranean and the Middle East: Influence of the South Asian monsoon. *Climate Dynamics*, 40:1103–1123.

Ulbrich, U., Brücher, T., Fink, A. H., Leckebusch, G. C., Krüger, A., and Pinto, J. G. (2003a). The central European floods of August 2002: Part 1 – Rainfall periods and flood development. *Weather*, 58(10):371–377. _eprint: https://rmets.onlinelibrary.wiley.com/doi/pdf/10.1256/wea.61.03A.

Ulbrich, U., Brücher, T., Fink, A. H., Leckebusch, G. C., Krüger, A., and Pinto, J. G. (2003b). The central European floods of August 2002: Part 2 -Synoptic causes and considerations with respect to climatic change: The central European floods of August 2002: Part 2 -Synoptic causes and considerations with respect to climatic change. *Weather*, 58(11):434–442.

van Bebber, W. (1891). *Die Zugstrassen der barometrischen Minima nach den Bahnenkarten der deutschen Seewarte für den Zeitraum 1875-1890.* Meteorologische Zeitschrift.[Offprint].

Vicente-Serrano, S. and López-Moreno, J. (2008). Nonstationary influence of the North Atlantic Oscillation on European precipitation. *Journal of Geophysical Research*, 113.

Westermayer, A. T., Groenemeijer, P., Pistotnik, G., Sausen, R., and Faust, E. (2017). Identification of favorable environments for thunderstorms in reanalysis data. *Meteorologische Zeitschrift*, 26(1):59–70.

Woollings, T., Hannachi, A., and Hoskins, B. (2010). Variability of the North Atlantic eddy-driven jet stream: Variability of the North Atlantic Jet Stream. *Quarterly Journal of the Royal Meteorological Society*, 136(649):856–868.

Wulff, C. O., Greatbatch, R. J., Domeisen, D. I. V., Gollan, G., and Hansen, F. (2017). Tropical Forcing of the Summer East Atlantic Pattern. *Geophysical Research Letters*, 44(21):11,166–11,173.

Yee, T. and Wild, C. (1996). Vector Generalized Additive Models. *Journal of the Royal Statistical Society. Series B (Methodological)*, pages 481–493.

Zveryaev, I. I. and Allan, R. P. (2010). Summertime precipitation variability over Europe and its links to atmospheric dynamics and evaporation. *Journal of Geophysical Research*, 115(D12):D12102.